Bubble Dynamics in a Fluidized Bed

An Experimental Study Using X-ray Tomography

S. M. Podber

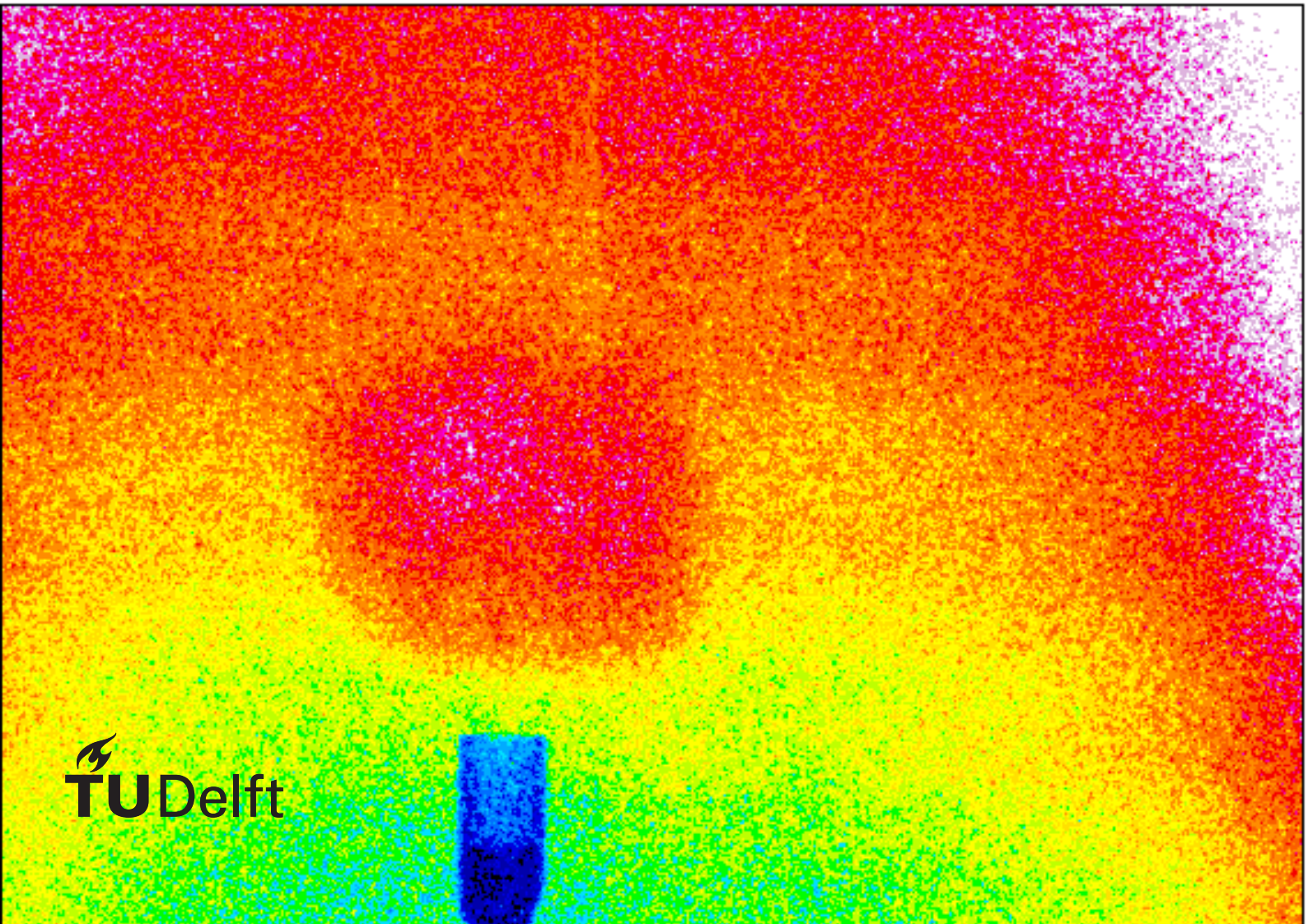

Bubble Dynamics in a Fluidized Bed

An Experimental Study Using X-ray Tomography

by

S. M. Podber

to obtain the degree of Master of Science
at the Delft University of Technology,
to be defended publicly on 18 August Friday, 2023 at 10:00 AM.

Student number: 5451558
Project duration: November 21, 2022 – August 18, 2023
Thesis committee: Dr. Eng. L. Portela Thesis supervisor
Dr. B. Bera
Prof. dr. ir. R.A.W.M. Henkes
Prof. dr. ir. W. de Jong

An electronic version of this thesis is available at http://repository.tudelft.nl/.

TU Delft

Abstract

Fluidized bed reactors are catalytic multiphase reactors capable of processing large volumes with relatively high mass and heat transfer, which is appealing to a variety of industries. The presence of voids, in this case gas bubbles, within these systems can be detrimental to the efficiency and are desired to be minimized. Further fundamental understanding of the bubbles is necessary to model, design, and control them. However, the study of bubbles is difficult, as these beds are typically opaque and 3D. Current studies of bubbles within fluidized beds are often limited to use of quasi-2D set ups, specialized particles, or internal measuring devices.

This research utilizes a newly constructed experimental setup consisting of three x-ray source and flat panel detector pairs that produce 2D projections. This setup allows for investigation into the bubble dynamics inside a 3D cylindrical column with industrial particles. The possibilities and limitations of the use of 2D projections to obtain fully 3D time-resolved reconstructions were explored through simple 3D reconstructions of injections of single bubbles. These 3D reconstructions showed the potential of the setup for 3D time-resolved studies of the bubble dynamics and laid the groundwork for future studies.

Apart from the ability to obtain 3D reconstructions, the 2D projections can be used to study the dynamics of the bubbles. In this research, 2D projections of an injection of a single bubble were used to develop a deeper fundamental understanding of the shape, motion, and dynamics of an individual bubble traversing through a bed. The bubble shape and size were obtained through a horizontal slicing technique, which assumes axis-symmetry around the vertical axis. Different background fluidization levels, injection volumes, injection velocities, particles, and column diameters were investigated. An analysis of the individual bubble trajectories and the statistical averages provided insight into the interconnection of these factors. The two previously studied bubble stages, formation and rising, were observed. The rising stage was observed to have two regions, stable and unstable. The stable region, following the formation stage, occurs when the motion of the bubble is essentially rectilinear. The unstable region, following the stable region, occurs when the bubble moves sideways while traversing the column in an irregular motion. A simple analogy to gas bubbles in a liquid was drawn, suggesting the bubble cloud, or particles surrounding the bubble, plays a vital role, especially in the formation of the bubble. Standard correlations for the bubble rise velocity based on a constant bubble Froude number were found to be insufficient at accurately describing the bubble velocity and dynamics. The Froude number for individual bubbles appears to be non constant and dependent on parameters that have not been previously considered, like the level of background fluidization.

Contents

1 Introduction **1**
- 1.1 Motivation and Background . . . 1
- 1.2 Current Techniques and Previous Works . . . 1
- 1.3 Research Goals and This Work . . . 2
- 1.4 Outline . . . 3

2 Background Information **4**
- 2.1 Fluidized Beds . . . 4
- 2.2 Bubbles . . . 8
- 2.3 X-rays and X-ray Tomography . . . 11

3 Experimental Setup **13**
- 3.1 Setup and Apparatuses . . . 13
- 3.2 Image Processing . . . 16

4 Results **20**
- 4.1 Verification . . . 21
- 4.2 Representative Cases . . . 23
- 4.3 Formation Stage . . . 31
- 4.4 Rising Stage . . . 36
- 4.5 Velocity and Dynamics Analysis . . . 46

5 Conclusion and Recommendations **52**
- 5.1 Conclusions . . . 52
- 5.2 Recommendations . . . 53

Bibliography **55**

Symbols **59**

Abbreviations **60**

A Appendix A **61**
- A.1 Dynamics of a gas-liquid bubble . . . 61

B Appendix B **64**
- B.1 Individual Bubble Paths . . . 64
- B.2 Statistical Overview including secondary bubble . . . 82
- B.3 3D Reconstruction . . . 84

C Appendix C **88**
- C.1 Kato-Wen and Werther . . . 89
- C.2 Froude Number . . . 92

D Appendix D **95**
- D.1 Slice Stacking Script . . . 95

1 Introduction

1.1. Motivation and Background

Industrial use of fluidized bed reactors is relatively young, with the first commercial applications starting in the mid-20th century. The use of fluidized bed reactors only continues to increase within a variety of industries, necessitating further fundamental understanding of the internal mechanisms to optimize these complex systems.

A fluidized bed reactor is a multiphase catalytic reactor. A fluid, gas and/or liquid, passes through a solid catalyst and fluidizes the particles. Voids, or bubbles, tend to form within these reactors due to excesses of fluid. Bubbles are desired to be minimized within fluidized bed reactors, as the formation of bubbles on the distribution plate greatly affects the overall mass and heat transfer [1]. The fluid trapped within the bubbles is hindered from reacting.

Fluidized bed reactors are preferred in certain industries because of the possibility of continuous operation, high mass transfer, temperature uniformity, and the suitability for large scale operations [2, 3]. Fluidized bed reactors are used in oil cracking and refinement, gasification and combustion of coal, combustion of solid waste, nuclear fuel preparation, Fischer-Tropsch synthesis, and a wide variety of other processes [2, 4].

Industrial settings utilize 3D columns with catalytic particles. Research is typically restricted to transparent particles, 2D setups, or setups with internal measuring apparatuses because of the opacity of the beds. These setups may severely affect the bubbles shape and motion, leading to dynamics that can vary from actual 3D column fluidized beds.

This research utilizes x-ray tomography to study the dynamics of a 3D column fluidized bed. The focus of this thesis is to expand upon the fundamental understanding of individual bubbles within a 3D column fluidized bed.

1.2. Current Techniques and Previous Works

Research on the internal dynamics of fluidized beds commonly utilizes experimentally compatible particles, quasi-2D setups, or 3D setups with internal measurement apparatuses to observe the column.

The catalytic material used in fluidized beds is typically opaque, obscuring the internal workings of the column, so transparent particles are used. Transparent and catalytic particles often have different properties, making comparison difficult, since the particle properties can affect important aspects of the fluidized beds. The quasi-2D setups can affect the shape and dynamics of the bubble, leading to different behavior than in actual 3D fluidized beds. The use of internal measurement apparatuses in 3D fluidized beds allows for the study of typical industrial setups and particles. However, these apparatuses can disrupt the bubbles and are unable to track the bubbles through the entirety of the column [5].

Some examples of techniques that have been used to study fluidized beds include:

- High speed cameras [6–8]
- Capacitance probes [9, 10]
- X-ray 2D imaging [5, 11–13]

- MRI [14]

Recent developments in MRI techniques allow for 3D time-resolved studies of the gas bubble and for the tracking of the particle motion and velocity in the emulsion phase. However, the MRI technique is restricted on the size and type of particles, as well as the size of the column, which is limited based on the size of the MRI machine.

The majority of research on bubbles in fluidized beds has been focused on statistical averages, using “local measurements” of bubbles occurring inside a bubbling bed. Few studies on individual bubbles injected in a bed exist, for example, studies by Brauer [15]. However, studies tracking single bubbles traversing through a ”tall” 3D columns of different sizes with industrial particles do not appear to have been conducted.

1.3. Research Goals and This Work

This work utilizes a recently developed setup by the Transport Phenomena Section. This setup allows for fully 3D time-resolved studies in fluidized beds using x-ray tomography [16]. Figure 1.1 shows a simplified diagram of the setup, consisting of three x-ray sources and flat panel detector pairs. The resulting 2D projections can be combined to obtain fully 3D time-resolved reconstructions of the different phases.

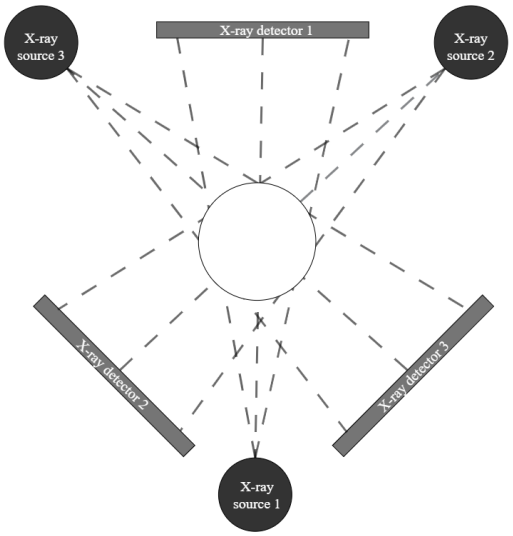

Figure 1.1: Fluidized bed setup utilized in this research

The 3D reconstruction based on the three 2D projections offers interesting possibilities, despite some limitations. The major limitations include limited angular resolution, which results in artifacts, and the difficulty in tracking particle motion and velocity in the emulsion phase [16]. The major benefits are the temporal resolution of the entire 3D shape-distribution field, the ability to utilize ”industrial” particles, and the ability to use a wide variety of 3D columns.

The overarching goals of this work are:

- To perform a preliminary exploration of the possibilities and limitations for a fully 3D time-resolved reconstruction from the 2D projections of three x-ray source-detector pairs for the study of the bubble dynamics, setting the stage for further work
- To investigate the bubble dynamics by tracking individually injected bubbles as they traverse a column from the injection site using 2D projections

The questions that guided this research are:

- What insight can tracking a single, injected 3D bubble provide?
- How can 2D projections be used to obtain an understanding of the 3D dynamics of a bubble?
- How can a single bubble be visualized using the 3D reconstruction based on the three 2D projections?

- How does different **background fluidization levels** affect individual bubbles in a single bubble injection?
- How does different **injection volumes and velocities** affect individually bubbles in a single bubble injection?
- How does different **particles** affect individual bubbles in a single bubble injection?
- How does different **column diameters** affect individual bubbles in a single bubble injection?

1.4. Outline

The structure of this thesis is as follows:

- Chapter 2: The background information related to fluidized beds, bubbles, models, and techniques
- Chapter 3: The experimental setup and image processing
- Chapter 4: The accuracy of these results, results, and comparison to literature and correlations
- Chapter 5: The possible conclusions drawn from the body of work and recommendations for future studies.

2

Background Information

2.1. Fluidized Beds

A fluidized bed occurs when a bed of solid particles is suspended in a fluid above a minimum superficial velocity (u_{mf}) and exhibits fluidized behavior. The particles will become suspended in the fluid, and the bulk mixture of fluid and particles will exhibit features similar to a fluid. This research will focus on gas-solid fluidized beds.

The types of fluidization can be categorized as homogeneous or heterogeneous fluidization. Homogeneous fluidization occurs when the solid particles are evenly distributed such that there are few observable bubbles. Heterogeneous fluidization occurs when the solid particles have a non uniform distribution, allowing for the formation of bubbles. Heterogeneous fluidization will be the focus of this study.

The motion of a fluid through a fluidized bed has been described through a variety of models. This study will focus on the two- and three-region models. Simplified diagrams of the two- and three-region models can be seen in Figure 2.1.

The two-region model describes a fluidized bed as an emulsion and bubble phase. The emulsion phase consists of the particles and fluidizing liquid, while the bubble phase consists of voids. This theory suggests that below u_{mf}, the input of fluid into the system will dissipate into the emulsion phase until u_{mf} is reached. After u_{mf} is reached, the formation of bubbles is possible [17].

The three-region model describes a bubbling fluidizing bed as an emulsion phase, a bubble phase, and a cloud surrounding the bubble [18]. The emulsion and bubble phases are the same as the two-region model. The major difference is the formation of a bubble cloud due to gas exiting the bubble and recirculating through the wake of the bubble. The bubble cloud is further discussed in section 2.2.

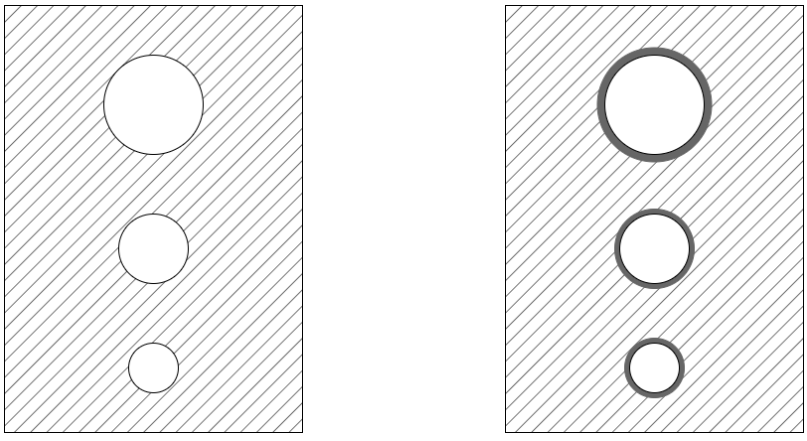

(a) Two-region model (b) Three-region model

Figure 2.1: Simplified diagram of two- and three-region models, based on Lee and Miller [19]

The u_{mf} can be determined empirically or theoretically. This study focuses on the empirical determination of the u_{mf}. The u_{mf} is affected by pressure, temperature, interparticle effects, vibrations, and different mixtures of fluids [3]. The u_{mf} affects the bubble shape, rise velocity, hold-up, and various other attributes, making the u_{mf} a vital aspect to understanding the hydrodynamic properties [20].

The bed is considered fixed when the superficial gas velocity (U) is less than u_{mf}. The relationship between the pressure drop within the bed (Δp_b) and U can be seen in Figure 2.2. The fluidizing behavior is dependent on whether the U increases or decreases. Increasing U results in a peak in the pressure ($\Delta p_{b,max}$) caused by particle-particle interactions. Decreasing U does not result in a pressure peak, as these physical interactions are not present when U decreases. The exact point of u_{mf} is not precisely defined; however, Figure 2.2 defines u_{mf} at Δp_{max}. This research defines u_{mf} when the bed is fluidized without bubbles present, which was typically at a U slightly below the $\Delta p_{b,max}$ curve. This definition may be unsuitable for certain Geldart particle types.

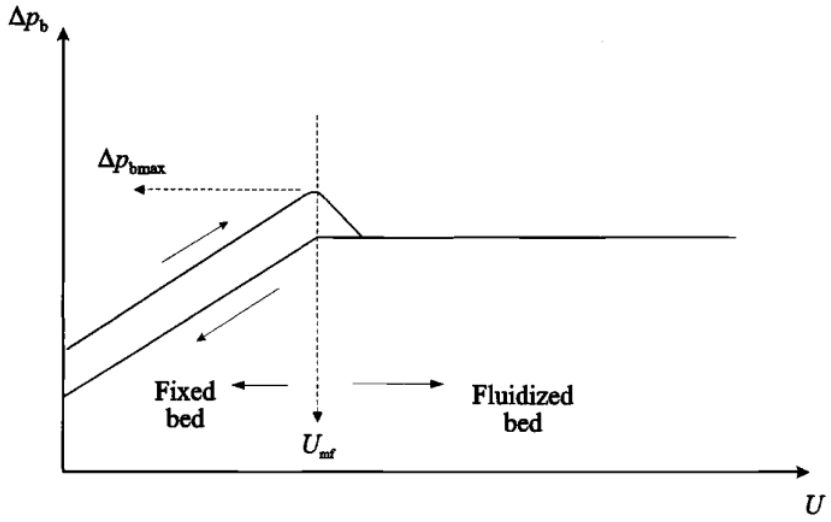

Figure 2.2: Pressure drop changes as gas velocity in/decreases [2]

This research aims to look at the bubble formation at 3 distinct U: below, at, and above u_{mf}. This study experimentally determines the u_{mf} of particles of two different sizes in columns of different diameters. Similar ratios of U/u_{mf} was used across the different particles.

2.1.1. Fluidization Regimes

The fluidized bed undergoes different regimes based on the U and particles. The particle types are described in section 2.1.2. The different regimes affect aspects of the reactor in a variety of ways, such as the heat and mass transfer. Visualizations of the different fluidization regimes can be seen in Figure 2.3. The regimes related to this research are: the fixed bed, the delayed bubbling, the bubbling, and the slugging regime.

The fixed bed regime occurs when U is less than the u_{mf} and is analogous to a packed or fixed bed. The delayed bubbling regime occurs when the bed is fluidized above the u_{mf} and under the minimum bubbling velocity (u_{mb}), resulting in a fluidized bed without bubbles. The delayed bubbling regime is only possible under certain conditions and certain particle types.

The bubbling regime occurs when u_{mb} is surpassed. Bubbles form consistently along the distribution plate. The u_{mb} is dependent on the attributes of the particles and fluid. Bubble coalescence and breakup become more prevalent. Coalescence is expected to be enhanced at increasing gas velocities during this regime, resulting in fewer and larger bubbles, relative to other regimes [2].

The slugging regime forms with increasing gas velocity. The bubbles in the bubbling regime will grow until the bubbles are similar in diameter to the column and experience significant wall effects. When the diameter of the bubble is over 60% of the diameter of the tube, the bubble is considered a slug [21]. At the initial formation of slugs, slugs are inconsistent but eventually stabilize and exhibit periodic behavior. The shape and behavior of slugs are dependent on the particle type.

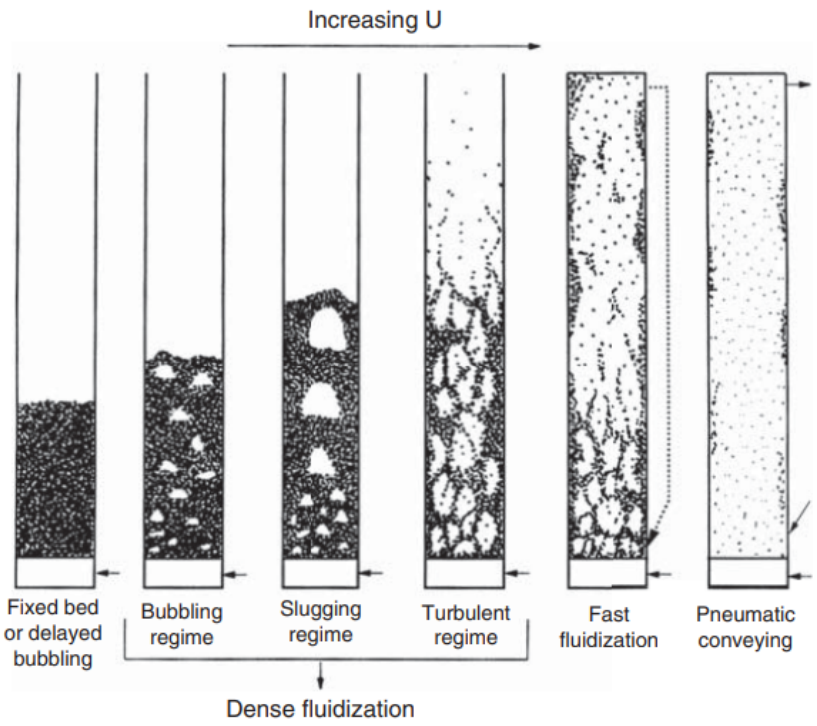

Figure 2.3: Fluidization regimes based on increasing U [3]

2.1.2. Geldart Classification of Particles

Within a gas-solid fluidized bed, the properties of the solid particles have a significant effect on the properties. Geldart delineated into four categories: Aerated (A), Bubbling (B), Cohesive (C), and Spoutable (D). Figure 2.4 represents the separation of the groups by mean particle size. The particles utilized in this experiment were Geldart A/B and B.

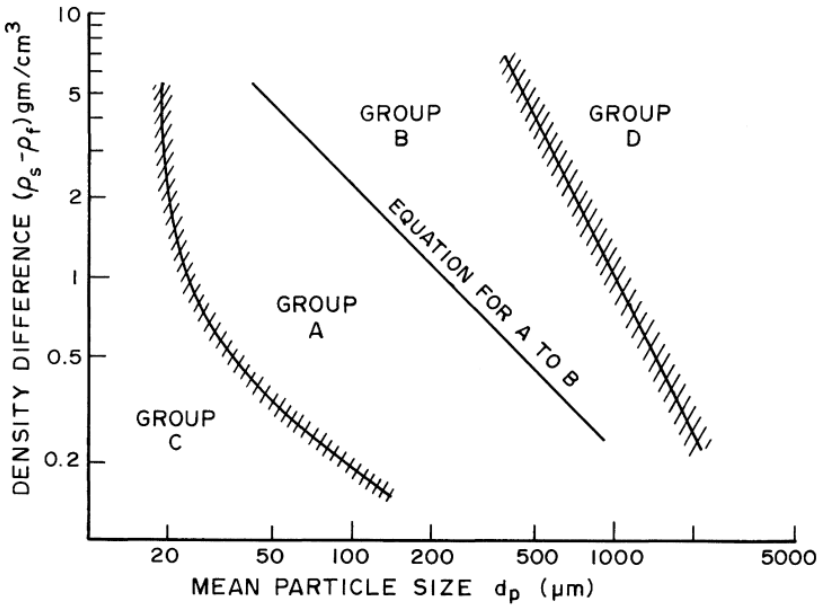

Figure 2.4: Geldart classification of fluidized particles at ambient conditions [22]

Group A is comprised of particles with diameters ranging from 30 to 100 μm. The hydrodynamic and interparticle forces are significant in the behavior of the particles [22]. These particles generally

fluidize well and allow for fluidization without reaching the bubbling regime. Bubbles tend to coalesce and breakup readily, leading to a maximum bubble size less than 10 cm [21].

Group B is comprised of particles between 100 to 1000 μm. The u_{mf} is equal to u_{mb}, resulting in bubble formation along the distribution plate as the particles begin to fluidize [22]. The interparticle forces are insignificant compared to the hydrodynamic forces. As the bubble moves up the column, the size of the bubble will grow approximately linear [21].

There are key differences between these bubbles, especially regarding the effects of bubble interactions. The splitting of bubbles is an important factor for Geldart A particles but is considered negligible for Geldart B particles [23]. Zhu et al. found in bubbling beds, bubbles in Geldart B beds can grow larger compared to bubbles in Geldart A/B beds [24].

2.1.3. Emulsion Phase Motion

Studies of the emulsion phase motion are limited, and the motion of the emulsion is expected to be complex.

Werther et al. found that for shallow beds, defined as the bed height (H_{bed}) being less than 2 times the bed diameter (D_{bed}), exhibited behavior displayed in 2.5.A, which is also believed to be the general motion of the emulsion phase [25].

Based on the general emulsion motion, Kunii et al. proposed that within a ”deep” (H_{bed}/D_{bed} > 1) fluidized bed comprised of Geldart B particles, the emulsion motion will act as in Figure 2.5.B, where secondary vortex rings form [21].

This study focuses on ”deep” beds and does not observe behavior close to the surface of the bed. Additionally, the injection nozzle was approximately centered within the column and 20 cm, about 1/3 of the total bed height, above the distribution plate. The emulsion phase motion is expected to affect the bubble motion and may be a possible explanation for some of the observations within the experiments. However, the exact motion of the emulsion phase was not observable with these experiments.

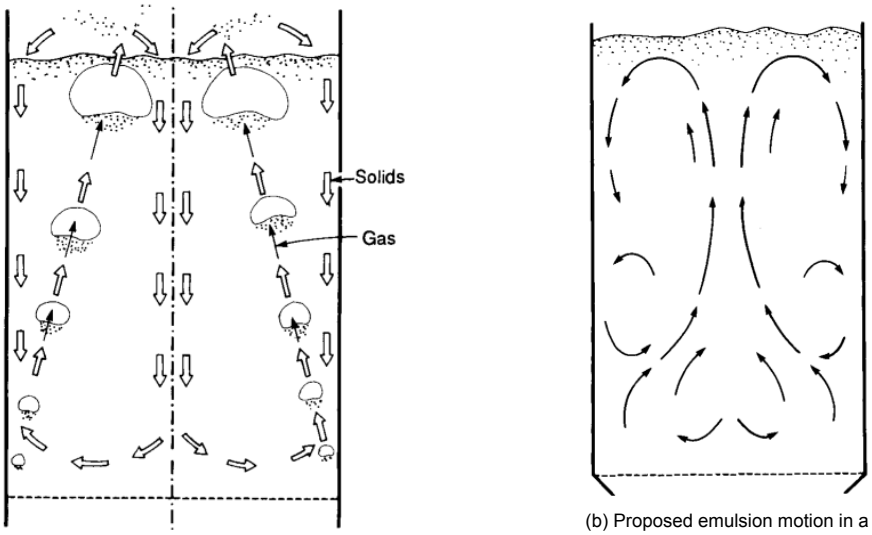

(a) General emulsion motion

(b) Proposed emulsion motion in a ”deep” bed for Geldart B type particles

Figure 2.5: Diagrams of emulsion movement [21]

2.1.4. Dimensionless Description of the Column

The current uses of dimensionless variables to describe gas-solid fluidized bed reactors are typically for scaling factors in scale-up and optimizing CFD-DEM models.

A dimensionless variable investigated in prior works is the Froude number. The Froude number compares the inertial forces to external forces. The Froude number has been typically used to distinguish fluidization regimes or to describe certain attributes of the particles [21, 22, 26–28].

Salehi et al. described an excess velocity Froude number (Fr_{column}) to increase the accuracy of simulations regarding the mixing times of Geldart B particles at a variety of fluidization levels [29].

Excess velocity-based Froude Number:

$$Fr_{column} = \frac{u - u_{mf}}{\sqrt{gD_{bed}}} \tag{2.1}$$

where D_{bed} is the diameter of the column.

This Froude number is utilized to describe the overall column, rather than the effects on individual bubbles. Other uses of the Froude number for fluidized bed focus on the relationship of u_{mf} to the particle size. The Fr_{column} suggests no bubbles are observed when Fr_{column} is $\mathcal{O}(10^{-3})$, some bubbles are present when Fr_{column} is $\mathcal{O}(10^{-2})$, and bubble-like voids are present when Fr_{column} is $\mathcal{O}(10^{-1})$ [30].

2.2. Bubbles

Bubbles naturally form within the column due to excesses in gas. Bubbles are generally undesirable in industrial scale, as the gas inside the bubble does not readily interact with the particles. As they rise in the column, bubbles were observed to form an ellipsoid with a wake. The wake consists of high velocity particles. The wake is a key aspect of vertical transport because particles will aggregate and be shed from the wake as the bubble traverses the column [31]. The bubble and wake combined approximately form a sphere.

Bubbles can be defined as ”fast” or ”slow” moving bubbles. A fast bubble occurs when the bubble rise velocity (u_{br}) is larger than U and a slow bubble when u_{br} is less than U. The structure of fast and slow bubbles in a gas-solid fluidized bed reactor can be seen in Figure 2.6.

Fast bubbles form a suspension layer around the bubble, referred to as the cloud. The cloud formation is a key factor in the three-region model. The cloud forms as the gas is released from the fast bubble and is recirculated into the bubble. The gas within the emulsion phase does not mix with the cloud, instead moving aside as the bubble passes.

Regarding the slow bubble, the gas within the emulsion phase uses the slow bubble as a convenient pass through to the surface, and the bubble sheds gas while traversing the column [21].

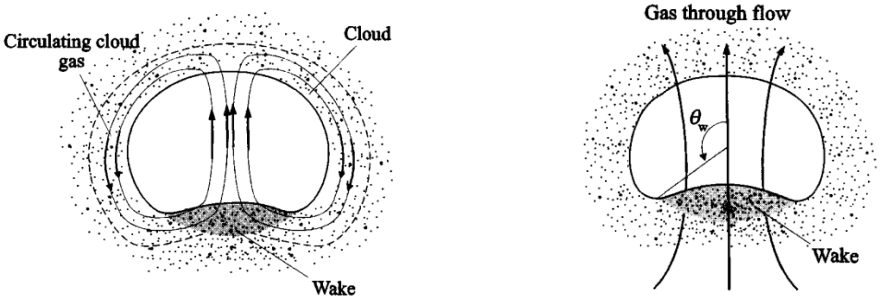

(a) Fast bubble (b) Slow bubble

Figure 2.6: Diagram of ”fast” and ”slow” bubbles [2]

2.2.1. Mechanisms of Bubble Splitting

The mechanism of splitting bubbles has been theorized into two main theories: wake collapse and roof collapse theories.

The wake collapse theory describes the mechanism of particles being drawn up through the wake and splitting the bubble. The circulation velocity of the particles must exceed the terminal free fall velocity of the particles for wake collapse to occur [32, 33].

The roof collapse theory describes the mechanism of particles falling through the top of the bubble to split the bubble [34]. This would occur due to a Rayleigh-Taylor type instability, where a less dense fluid pushes against a denser fluid [35].

2.2.2. Observed Bubble Regimes

A study by van der Schaaf et al. described the behavior of a bubble in three stages: formation, rise, and eruption [36]. These regimes have been observed in other works [7, 8, 14].

For a single bubble injection, the formation stage is when the bubble is injected into the system. A study by Mostafaei et al. observed the following behavior when injecting a single bubble. The injection of gas into the bed formed a compression wave. The bed did not considerably expand initially as the particles moved into empty spaces. However, as the injection continued, the bed expands, leading to a decrease in gas velocity and an increase in particle velocity [8]. This study by Mostafaei et al. focused on a single injection duration and velocity. However, changes in the injection variables may affect the particle interactions during the formation, such as faster injection velocities would cause more force on the particles compared to lower injection velocities for the same total injected volume.

The rising stage occurs after the bubble is released from the formation site and travels up the bed. The bed height will remain lifted. Van der Schaaf et al. observed after the bubble passed the pressure probe, the pressure of the bed returned to the pre-injection state [36]. The bed beneath a bubble is likely to return to a similar pre-injection state as the bubble rises. The formation of the bubble may affect the rising stage, as the density of the particles around the bubble during the formation stage could affect the interaction of the bubble with the cloud and emulsion phase. The eruption stage occurs when the bubble reaches the surface of the bed and exits, often causing the particles to aerosol. The bed settles and returns to a pre-bubble formation stage.

This research focuses on the formation and rising stage, as the eruption stage was outside of the frame.

2.2.3. Equivalent Diameter

There are a multitude of correlations to study the diameter of the bubble, summarized in Karimipour et al. [37]. The correlations chosen for this study were Werther and Kato-Wen because of their ability to calculate equivalent diameters at a U below U_{mf}. This research was able to specify the equivalent diameter of the studied bubbles; however, these correlations are regarding naturally formed bubbles within a bubbling bed.

Werther [38]:

$$d_{eq} = d_0[1 + 0.272(u - u_{mf})]^{1/3}(1 + 0.0684H)^{1.21} \tag{2.2}$$

where H is the height of the bubble in the column and d_0 is a defined variable based on Geldart particle type, which is 0.610 for Geldart A and 0.853 for Geldart B.

Kato-Wen [39]:

$$d_{eq} = 0.14\rho_p d_p(u/u_{mf})H + d_{b0,eq} \tag{2.3}$$

where ρ_p is the density of the particle, d_p is the diameter of the particle, and $d_{b0,eq}$ is the initial equivalent diameter of the bubble.

The d_{eq} of the bubbles captured by the projections was calculated via image processing. Riechmann found the utilization of x-ray attenuation to measure the bubble depth deviates significant from utilization of the projections to measure the bubble volume [5]. Therefore, this study will focus on the use of projections to calculate bubble diameter, the processing of which is described in section 3.2.1.

2.2.4. Bubble Rise Velocity

The bubble will approach the surface at a certain velocity, defined as the bubble rise velocity (u_{br}). The u_{br} affects particulate circulation within the reactor, resulting in increased heat transfer between the bed and the walls or heat exchangers. A commonly used correlation to measure the u_{br} is the Davidson and Harrison correlation [32]. This correlation is based on the Froude number and assumes the Froude number is constant.

Davidson and Harrison:

$$u_{br} = 0.711(gd_{eq})^{0.5} \tag{2.4}$$

where g is the acceleration of gravity and d_{eq} is the equivalent diameter.

The discrete u_{br} derived from the experimental results is obtained through,

$$u_{br} = YM_i - YM_{i+1} * f \tag{2.5}$$

where YM is the center of mass of the bubble along the y-axis, i is the frame number, and f is the frequency of the x-ray projections.

Within the individual analysis of bubbles, a B-spline is taken through the center of masses of the bubbles. The velocity can be derived from the B-spline, providing another method of obtaining u_{br}. In this research, the average was taken of the B-spline derivatives to obtain the u_{br}.

2.2.5. Bubble Dynamics

This research aims to use the Froude number to describe the individual bubbles through the relationship to the drag coefficient. The bubbles within a fluidized bed can be viewed analogous to bubbles in a gas-liquid bubble column, further expanded upon in Appendix A.1. For a bubble column, when the Reynolds number is large and bluff bodies form, the terminal velocity, the drag force, drag coefficient, and thereby the Froude number are all constant.

The overall motion of a single bubble in a fluidized bed can be simplified into two categories: when the bubble changes size and when the bubble is in motion. A near constant exchange of gas from the bubble to the emulsion phase is expected.

When the bubble expands or contracts, the surroundings are also moved, requiring work to be done. A diagram can be seen in Figure 2.7. The pressure difference between the bubble internally (P_{bubble}) and the cloud interface ($P_{interface}$), a relatively small area, is large. The large pressure difference would form a cloud with a significant force per unit length along the outside of the bubble (γ). Understanding the cloud is vital to understand the dynamics of the overall bubble. Passage of gas through and into the bed allows for the bubbles to interact with the system and other bubbles.

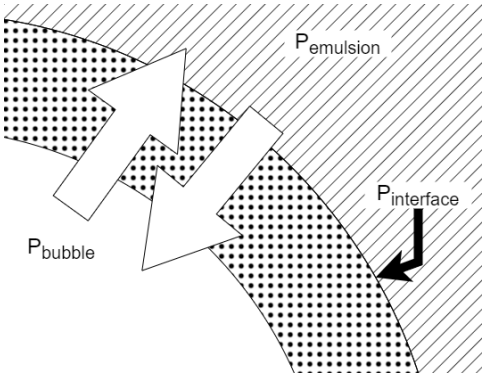

Figure 2.7: Simplified diagram of gas exchange between the bubble, cloud, and emulsion phase

This research is specifically focused on the dynamics of a single bubble. A single bubble that is reasonably far from the walls of a fluidized bed will have the velocity and dynamics determined by interactions between the gas and emulsion phase dynamics, which is directly related to the dynamics along the interface and cloud.

Gas-solid fluidized beds experience a significant amount of gas flux between the bubble and emulsion phase. These interactions are not present within a gas-liquid bubble column, but an analogy between the different columns can be drawn and is further expanded upon in Appendix A.1. Gas bubbles in liquid have an interdependence between shape, flow, and interfacial rheology; gas bubbles in solids have an interdependence between shape, flow, and dynamics near the cloud. The gas-liquid interfacial rheology is assumed to be exactly 2D and can be simple, comprised of the static surface tension for a pure liquid, or complex, involving surface viscosity, surfactants, ect. The gas-solid dynamics near the cloud are not exactly 2D and comprises of interactions between the gas and the particles near the interface. Despite these differences, analogies can be drawn between gas-solid and gas-liquid columns.

A quasi-steady state assumption allows for a balance between the buoyancy force (F_B) and drag force (F_D) to be drawn. The ρ associated with these forces can be taken as the density of the emulsion far from the interface. In general, the relationship of the Froude number to the drag coefficient (C_D) is:

$$Fr = \sqrt{\frac{2}{C_D}} \tag{2.6}$$

The equivalent Froude number (Fr_{eq}) can be taken as:

$$Fr_{eq} = \sqrt{\frac{4}{3}\frac{A_v}{A_\perp}\frac{1}{C_{D\perp}}} \tag{2.7}$$

where A_v is the volume based area, $A_\perp$ is the perpendicular area of the bubble, and $C_{D\perp}$ is the perpendicular drag coefficient.

The Davidson and Harrison correlation takes the Froude number as a constant to obtain the bubble rise velocity, so that $U_{br} \propto \sqrt{d_{eq}}$. The assumption of the fixed bluff body shape of the bubble and a interfacial force dominated flow are taken for this correlation, which are based on an analogy to the constant spherical cap regime for gas-liquid bubbles. When applying this analogy, the shape of the bubble is not affected by the dynamics near the cloud. However, if the dynamics near the cloud are important, then the assumption of a constant Froude number may not hold. If there is an analogy between the cloud dynamics of a gas-solid bubble and static surface tension of a gas-liquid bubble, then the U_{br} would be constant.

2.3. X-rays and X-ray Tomography

2.3.1. X-rays

X-rays are a type of electromagnetic radiation with high energy, approximately 0.145 to 120 keV, and short wavelengths, approximately 0.01 to 10 nm. X-rays allow for insight into otherwise inaccessible processes through a noninvasive technique. The intensity of the x-ray decreases as it passes through materials; this phenomenon is called attenuation. Denser objects are able to more readily absorb radiation, resulting in a relatively lighter image when compared to less dense objects.

When utilizing x-rays, beam hardening and scattering can affect the resulting projections. X-rays release energy along a spectrum of low to high energies, which are not attenuated or absorbed equally. The relatively lower energy x-rays are attenuated more easily, so the x-ray beams with high energy photons remain. resulting in x-ray beams that have increasing high energy photons. Figure 2.8 compares the energy of the photons that pass through a medium to ones that do not pass through a medium. This shift, or beam hardening, in the x-ray spectrum leads to a non constant attenuation coefficient (μ). The projections may have streaks or cause more dense areas to artificially decrease in value.

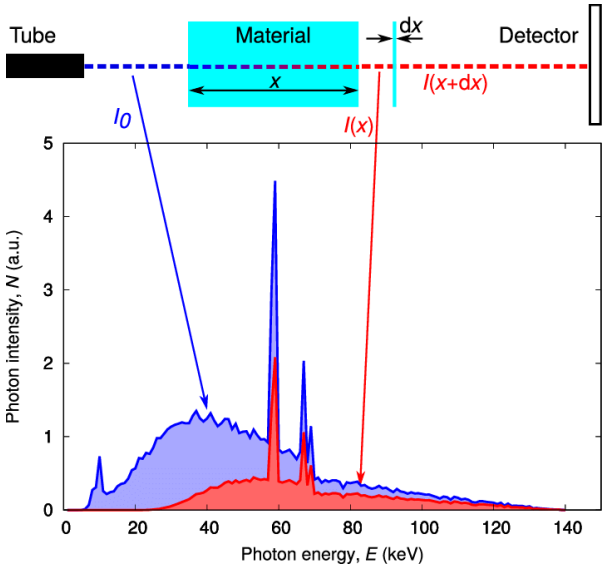

Figure 2.8: Energy spectrum of incident x-ray beam (blue) and x-ray beam through aluminium block (red) [40]

Overall, projections affected by x-ray scattering may exhibit increased noise and increased artifacts [41]. X-ray scattering is caused by either photoelectric effect or Compton scattering [42]. The photoelectric effect occurs when an incident photon interacts with a bonded electron, transferring all of the photon's energy and ejecting the electron. A new electron takes the place of the ejected electron, resulting in the release of a characteristic photon. Compton scattering occurs when an incident photon interacts with a bonded electron and transfers some of the photon's energy to the electron. The electron and photon are scattered. The photoelectric effect affects the contrast of the image, while Compton scatter can lead to an unclear background and artifacts.

2.3.2. X-Ray Tomography

When taking x-rays with a single source and detector, a 2D image, called projectional radiograph, is produced. Obtaining 3D images from x-rays is possible through computational tomography (CT) scans. The CT scans are a noninvasive technique that can allow for observation into opaque subjects, like a fluidized bed.

CT scanners take multiple images of a target at different angles, which are complied and reconstructed into 3D. Similar to how a pixel can be related to the length in 2D images, voxels are related to the cubic volume of a 3D projection. Increasing the voxels will allow for a more ”sharper” image but is dependent on the system settings.

Typically, CT scanners utilize a rotating x-ray source as the target remains stationary. This is not possible with a fluidized bed reactor, as the motion within the column would produce noise and make the resulting scans indecipherable. A possible alternative, executed in this research, is the use of multiple static sources for targets that cannot remain stationary. The multiple static sources/detectors, 3 in the case of this research, are aligned in different angles around the column that allow for 3D reconstruction.

Simultaneous Iterative Reconstruction Technique

The resulting images from the projections must be processed to generate a 3D reconstruction. There are two major categories of image reconstruction: analytic and iterative reconstruction. The research utilizes iterative reconstruction, specifically the Simultaneous Iterative Reconstruction Technique (SIRT). SIRT is a quadratic optimization technique frequently utilized in medical applications. The SIRT corrects the density after all ray paths have been considered, rather than after each ray path [43].

The 3D reconstructions in this research utilized script developed by A.B.M. Graas with the Centrum Wiskunde & Informatica (CWI) and further details on the 3D reconstruction scrip is available in Graas et al. [16].

3

Experimental Setup

The following chapter will describe the experimental setup and apparatuses. The methodology of image analysis is described.

3.1. Setup and Apparatuses

The theoretical design of the x-ray setup can seen in Figure 3.1.

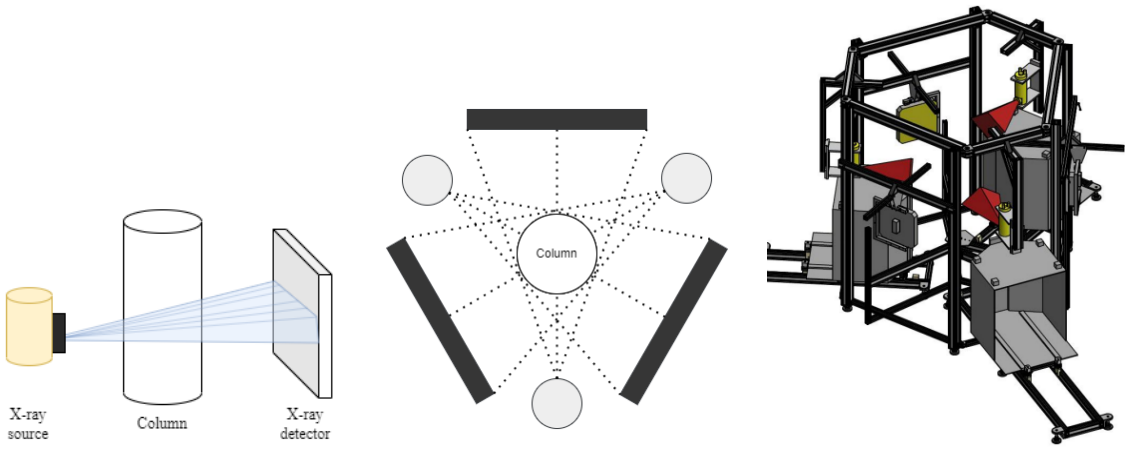

(a) Setup of single x-ray source (b) Overhead view (c) 3D model

Figure 3.1: Diagrams of the experimental setup

The experiments were conducted with three evenly spaced x-ray sources and flat panel detector (FPD) with a centered fluidized bed column. The x-ray sources and detectors were arranged to allow for the generation of a 3D tomogram. The FPDs can be adjusted along tracks and rotated. The x-ray sources are fixed. The central column can be adjusted vertically. The air to the column is supplied through a sintered porous distribution plate. The flow of air to the entire system via the sintered porous distribution plate is referred to as the background fluidization level (U). The background fluidization level can be changed through changing the flow rate of gas into the system.

3.1.1. Column and Bubble Injection

The central columns utilized in the experiments were cylindrical PMMA columns with inner diameters of 15 and 5 cm.

A simplified P&ID for the injection of a single bubble into a column can be seen in Figure 3.2. A mass flow controller (EL-FLOW Select F-201CV, Bronkhorst High Tech, B.V.) is connected to a pressure regulator valve and a 2.5 L pressure vessel tank. A solenoid valve (type 166B-871IJM, Mac Valves Europe, Inc.) opens for the specified injection duration (t_{inj}). The gas passes through a central nozzle

(Ø 0.5 cm) fitted with porous cap. The porous cap ensures even gas distribution throughout the bubble formation. The injection of air into the system through the nozzle is referred to as the injection velocity (Q). A period of 2 s is given between bubble injections to minimize bubble-bubble interactions. The t_{inj} can be varied to affect the volume of injection. The spherical equivalent diameter of the volume of injection ($d_{eq,inj}$) can be calculated. The pressure within the pressure vessel can be varied to affect the injection velocity.

The specifications of the columns and can be see in Figure 3.3 and table 3.1. For the 15 cm column, the injection nozzle is approximately 28 cm above the distribution plate, so the injected bubble can be easily isolated from the bubbles forming along the distribution plate and allows for the study of the individual bubble.

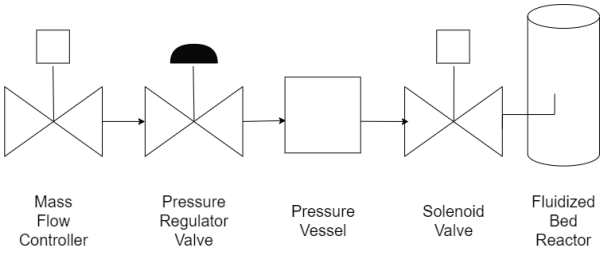

Figure 3.2: Simplified single bubble injection P&ID

Inner diameter (m)	0.15	0.05
Distance of nozzle tube from bottom of column (m)	0.28	0.030
Unfluidized bed height above nozzle (m)	0.40	0.40
Bed growth (m)	0.009	0.012
Fig. 3.3.A (cm)	6.1	
Fig. 3.3.B (cm)	6.3	
Fig. 3.3.C (cm)	1.0	
Fig. 3.3.D (cm)	1.0	
Fig. 3.3.E (cm)	0.80	

Table 3.1: Column specifications

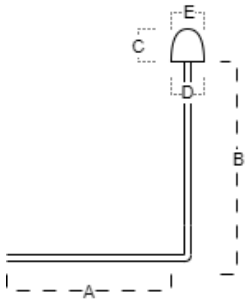

Figure 3.3: Specifications of the injection nozzle, not to scale

Experiments were run with two different particles, described in Table 3.2. Different particles were chosen to investigate the different effects on the bubbles of Geldart A/B and Geldart B particles.

For each injection, the volumetric flow rate and injection duration were utilized to calculate the $d_{eq,inj}$ and the velocity of the gas, which can be seen in tables 3.3 and 3.4. The pressures, and thereby the injection velocities, were selected based on the limitations of the setup. The pressure regulator valve had a maximum of approximately 2 bar, so 1.8 bar was selected to allow for the highest available injection velocity. The pressure of 0.75 bar was selected because it was approximately half of the

	Puralox® NWa-155 Sasol Germany GmbH	Polystyrene
Material	$\gamma - Al_2O_3$	Polystyrene
Geldart classification	A/B	B
Mean Sauter diameter [d_p] (mm)	0.289	0.500
Particle density [ρ_p] (kg/m^3)	1350	1050

Table 3.2: Particle specifications [5, 44]

initial injection velocity. The pressure of 1.3 bar was used because the pressure regulator valve was manually set for these experiments and was the closest possible pressure to the 1.8 bars from previous experiments.

Pressure (bar)	1.8		0.75	
t_{inj} (ms)	Avg $d_{eq,inj}$ (cm)	Avg Q (m/s)	Avg $d_{eq,inj}$ (cm)	Avg Q (m/s)
20	2.93	33.9	2.29	13.7
35	3.64	36.8		
50	4.03	34.8	3.22	17.8
60	4.34	36.3		
100	5.06	34.5	4.08	18.1
200	6.53	37.1	5.09	17.6

Table 3.3: Average $d_{eq,inj}$ and Q for 15 cm column

Pressure (bar)	1.3	
t_{inj} (ms)	Avg $d_{eq,inj}$ (cm)	Avg Q (m/s)
20	2.74	27.3
50	3.76	28.4
100	4.72	27.9
200	5.92	27.7

Table 3.4: Average $d_{eq,inj}$ and Q for 5 cm column

The gas flow through the distribution plate is alternated between three levels of background fluidization. A summary of the levels of background fluidization used for each particle and column size can be see in Tables 3.5 and 3.6. These column sizes were used to understand the wall effects and slugging.

Column size (cm)	15	
d_p (mm)	0.2	0.5
1.1Umf (cm/s)	3.02	14.2
Umf (cm/s)	2.64	12.9
0.7Umf (cm/s)	1.89	9.05

Table 3.5: U experimentally used in relation to U_{mf} in 15 cm column

For the 15 cm column, the bed is studied at the fluidization flow rates of $0.7U_{mf}$, U_{mf}, and $1.1U_{mf}$.

During the experiments in the 5 cm column, a large discrepancy was seen between the predicted and experimental U_{mf}. The discrepancy was resolved upon repeating the experiments and has been attributed to a leak in the connections providing the background fluidization to the 5 cm column. The background fluidization taken for the 5 cm column were above and below U_{mf}, but the exact ratio

Column size (cm)	5		
d_p (mm)	0.2		0.5
Trial	1	2	2
Above Umf (cm/s)	5.09		
Umf (cm/s)	4.24	3.39	14.4
Below Umf (cm/s)	3.39		

Table 3.6: U experimentally used in relation to U_{mf} in 5 cm column

is unknown. The values of the background fluidization obtained during the experiment were used to analyze and describe the results, rather than the relationship to U_{mf}.

3.1.2. X-ray

The setup for the x-ray system can be seen in Figure 3.1. The setup consists of three x-ray sources and three x-ray detectors in pairs, controlled via LabView.

The detectors have a sensitive area of 307x302 mm, or 1548x1524 px, with a resolution of 22 Hz. The detection area can be cropped up to to 307x20 mm, or 1548x100 px, allowing for a resolution of 200 Hz. Multiple crops of the 15 cm column were taken: one crop accounting for the entire diameter, resulting in a frame rate of 30 Hz, and one crop taken of 5 cm total width surrounding the injection nozzle, resulting in a frame rate of 65 Hz. The 5 cm column had a single crop encompassing the diameter column, resulting in a frame rate of 75 Hz. A simplified diagram representing the different frames within the column can be seen in Figure 3.4.

The normalized height in this research is defined as the center of mass of the bubble along the vertical axis from the top of the nozzle until the bubble exits the projection frame, approximately 22 cm in total length.

A summary of the x-ray specifications can be seen in table 3.7.

X-ray source	Yxlon Y.TU 160-D06
X-ray source limit (kV)	150
X-ray detector	Teledyne Dalsa Xineos 3131 CMOS flat panel detectors
Detector frame rate (Hz)	22 - 200
Detector Resolution (px)	1548x1524 - 1528x100
Origin-source distances (mm)	935 / 947 / 937
Origin-detector distances (mm)	273 / 268 / 294

Table 3.7: X-ray setup

3.2. Image Processing

3.2.1. 2D

The system is calibrated utilizing a dark, light, full unfluidized, and a fluidized column.

The image is pre-processed through MATLAB 2017b by removing dead pixels and rotating the image. Dead pixels adjusted through interpolation based on mean values between neighboring pixels. The image is rotated such that the distribution plate is located at the bottom of the image.

The image is then processed via ImageJ. The processing steps in ImageJ can be seen in Figure 3.5. The raw image undergoes background homogenization, thresholding, and shape detection.

The minimum intensity of the fluidized column without bubble injections is subtracted from the intensity of the bubble injection projections, removing a majority of the background. The resulting image undergoes ”rolling ball” smoothing algorithm and application of a Gaussian filter, resulting in background homogenization. The threshold method is IsoData and is fixed.

The image is binarized through the built-in particle analysis feature, which produces a Regions of Interest (ROI) for each bubble. The ROI can be exported as a list of points along the x- and y-axes, composing the outline of the bubble. This file is processed with Python 3.0 to determine characteristic features of the bubble, like the equivalent diameter. The relevant Python script can be seen in Appendix

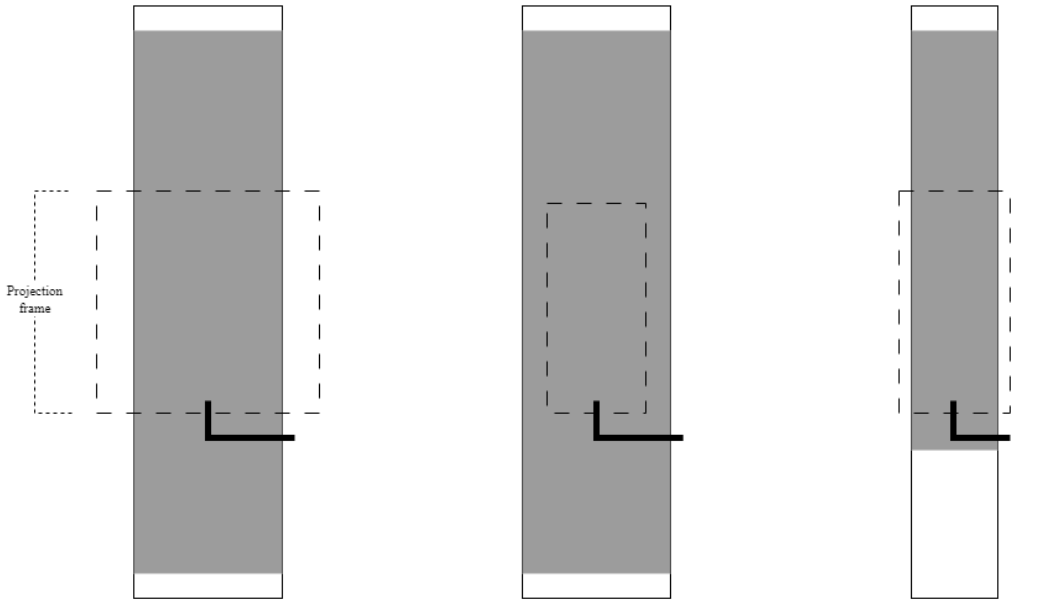

(a) D_{bed}: 15 cm, f: 30 Hz (b) D_{bed}: 15 cm, f: 65 Hz (c) D_{bed}: 5 cm, f: 75 Hz

Figure 3.4: Simplified diagram of the frame and bed height in column, not to scale

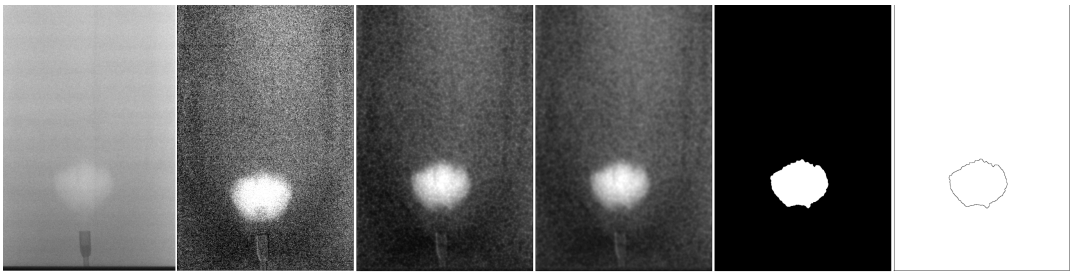

Figure 3.5: Example of image processing in ImageJ

D. This approach is simple to automate and obtain information for large quantities of data. However, certain features, like the bubble cloud, were lost through this method of image processing.

The d_{eq} of the bubble was determined through a horizontal slicing technique, refered to as slice stacking. An example of slice stacking is seen in Figure 3.6. Slice stacking divides the image into a row of single pixels along the y-axis. The volume of each ”slice” is taken as vertically axis-symmetrical cylinder with a height of y, or 1 px, and a diameter of x_i, the horizontal length of the slice. The volume of all of the ”slices” added. The d_{eq} is determined by assuming the total volume is a sphere with rotational symmetry along the axis in the z-axis. The equations for the d_{eq}, interfacial area ($a_{s,b}$), and the equivalent diameter associated with the interfacial area ($d_{eq,a}$) can be seen in equations 3.1-3.3.

If the bubble splits, then the script can recognize the two bubbles, given the bubbles are not touching or overlapping. If the bubble is small, less than 50 pixels in total area, the bubble would be regarded as noise and would not be taken into account. The minimum pixel threshold can be adjusted.

$$d_{eq} = \sqrt[3]{\frac{6}{\pi}\sum_{n=1}^{N}\frac{\pi}{4}x_i^2\Delta y} \tag{3.1}$$

$$a_{s,b} = \sum_{n=1}^{N}\pi x_i\Delta y \tag{3.2}$$

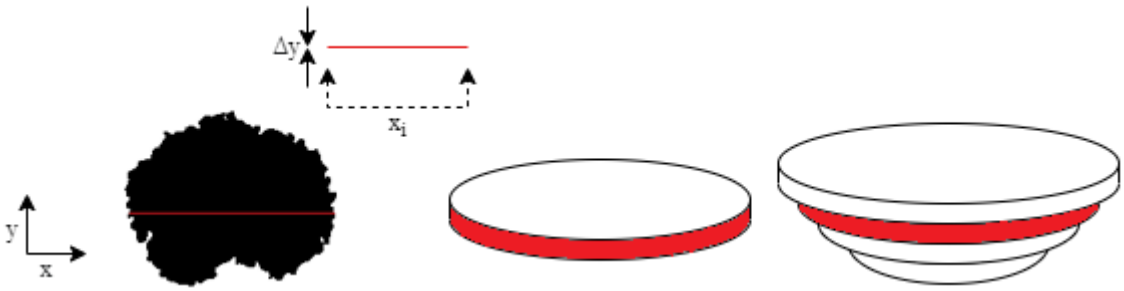

Figure 3.6: Simplified diagram of the slice stacking method

$$d_{eq,a} = \sqrt{\frac{a_{sb}}{\pi}} \tag{3.3}$$

3.2.2. 3D Reconstruction

Software developed by A.B.M. Graas was used to obtain a 3D reconstructions of the system [16]. Obtaining reconstructions of the column require projections to be taken of the calibration column with the same distance between the column, sources, and detectors as the experiments. For every 1 cm^3, approximately 36 voxels were taken. The completed 3D reconstruction calibration can be seen in 3.7. The specifics on the calibration of a 3D reconstruction can be found in section B.3.1.

After the calibration, the x-ray projections can be input into the script developed by A.B.M. Graas. The script provides a matrix based on the values of the voxels. The resulting matrix was analyzed in script developed by E.C. Wagner via MATLAB. This script utilizes the matrices to construct a 360° rotation of the column in a series of 2D images at intervals of 30°. These 2D images can be complied into a ”turn around” for a 3D understanding of the bubble at each frame. The script utilized in this research did not contain the entire length of the column and encompassed approximately 14 cm above the nozzle.

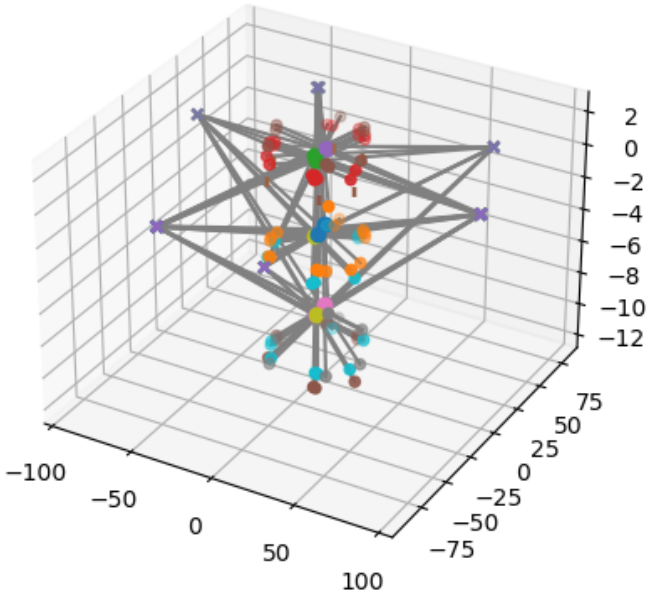

Figure 3.7: Completed reconstruction calibration

4

Results

The following chapter will discuss the results from the experiments. The previously described setup and image processing were utilized to run experiments of single bubble injections. The projections from these experiments were examined and will be discussed. A verification of the setup and techniques is assessed. The results are examined based on representative cases, the formation stage, and the rising stage. The approaches of examination are the analysis of the projections and the processed bubble motion, the statistical averages of bubbles, and the center of mass along the x- and y-axes of the bubbles, referred to as the trajectory.

The differing variables were isolated and defined as systems. Approximately 30 bubbles, captured at 3 different angles, were injected for each superficial background fluidization (U) and equivalent injection diameter ($d_{eq,inj}$) for the following systems:

1. D_{bed}: 15 cm, d_p: 0.2 mm, Q: 35 m/s
2. D_{bed}: 15 cm, d_p: 0.2 mm, Q: 17 m/s
3. D_{bed}: 15 cm, d_p: 0.5 mm, Q: 35 m/s
4. D_{bed}: 5 cm, d_p: 0.2 mm, Q: 26 m/s

By altering the injection velocity, the differences in injection volume and duration can be observe. Differing the particles will allow for investigation into the effects of size and type. The different sizes of column will allow for analysis of wall effects and slugs.

The $d_{eq,inj}$ can be compared for the different systems, as seen in tables 4.1 and 4.2.

System	1	2
t_{inj} (ms):	20	50
$d_{eq,inj}$ (cm):	2.9	3.2
t_{inj} (ms):	50	100
$d_{eq,inj}$ (cm):	4.0	4.0
t_{inj} (ms):	100	200
$d_{eq,inj}$ (cm):	5.0	5.1

Table 4.1: Comparison of $d_{eq,inj}$ for systems 1 and 2

As described in section 2.2.2, a fluidized bed has been previously described in three stages: formation, rising, and eruption. These experiments focus on the formation and rising stages.

The formation stage was approximately 3-5 frames per injection, making analysis of this region difficult. The formation stage is analyzed through the statistical averages. The rising stage was more visible within these experiments and was analyzed through the individual bubble trajectories. Within the rising stage, two distinct regions were observed: a ”stable” and an ”unstable” region. An example of the stages and regions studied in this research can be seen in Figure 4.1.

The setup for this experiment did not focus on the eruption stage. The top of the bed is approximately 40 cm above the injection nozzle; the total framing is approximately 20 cm above the nozzle; the

System	4	1	2
t_{inj} (ms):	20	20	20
$d_{eq,inj}$ (cm):	2.7	2.9	2.3
t_{inj} (ms):	50	50	50
$d_{eq,inj}$ (cm):	3.8	4.0	3.2
t_{inj} (ms):	100	100	200
$d_{eq,inj}$ (cm):	4.7	5.0	5.1
t_{inj} (ms):	200	200	
$d_{eq,inj}$ (cm):	5.9	6.5	

Table 4.2: Comparison of the $d_{eq,inj}$ for systems 1, 2, and 4

nozzle is approximately 20 cm above the distribution plate. It is assumed the top of the projection frame is reasonably far from the top of the bed such that the associated effects with the bed surface are negligible. It is also assumed the injection nozzle is far from the distribution plate such that the individual bubbles can be studied without consideration towards the behavior along the distribution plate.

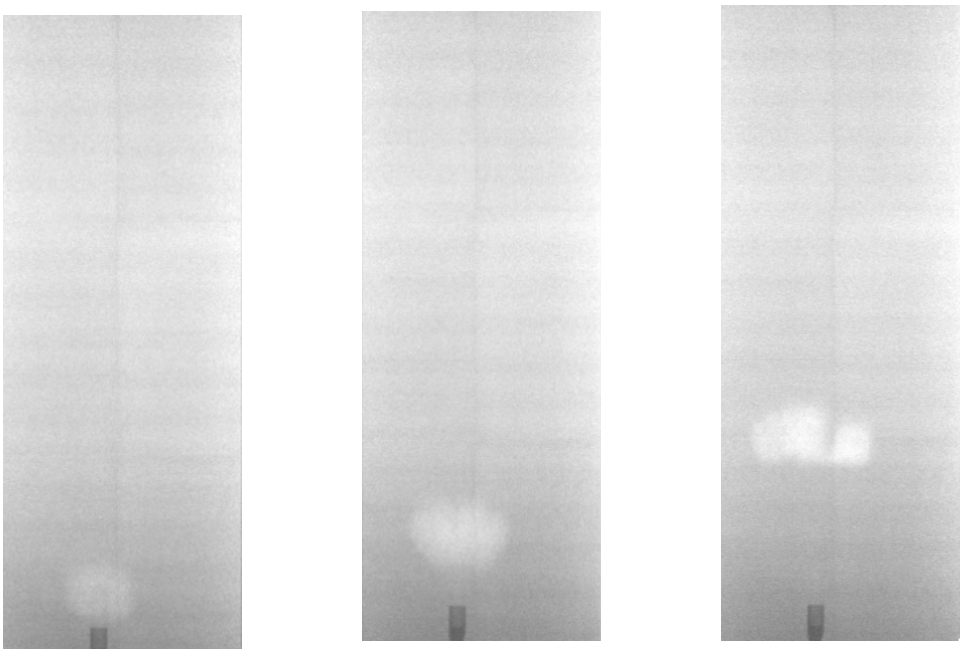

(a) Formation stage

(b) Rising stage, stable region

(c) Rising stage, unstable region

Figure 4.1: Different stages of a bubble at System 1, U: Umf, $d_{eq,inj}$: 3.6 cm

4.1. Verification

The techniques and methods of analysis utilized in this research are verified through different methods.

4.1.1. Minimum fluidization Velocity

The u_{mf} of the 0.2 and 0.5 mm particles in the 15 and 5 cm columns were determined experimentally. A particle is expected to have the same u_{mf} in sizes of cylindrical columns. The results reflect this, seen in Figures 4.2 and 4.3. The slight deviations of u_{mf} in the same particles in different diameter columns can be attributed to the differences in the tolerances of the control valves allowing gas into the different columns.

The u_{mf} of the 0.2 and 0.5 mm particles are determined to be 0.0264 and 0.129 m/s, respectively. The experimentally determined u_{mf} does not exactly correspond to the peak in ΔP in the figures because bubbling was observed at these Us. The U was adjusted until the bed was fluidized without

bubbling and was visually determined to be u_{mf}.

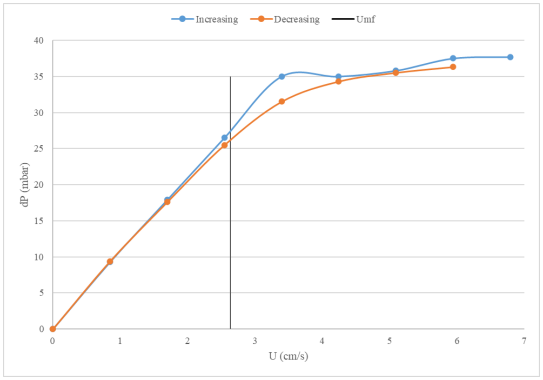

(a) 5 cm column

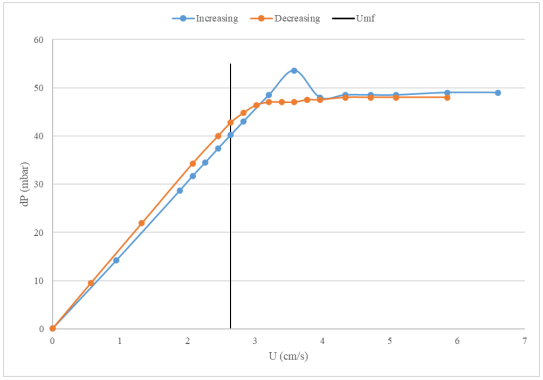

(b) 15 cm column

Figure 4.2: Fluidization velocity of a 0.2 mm particle

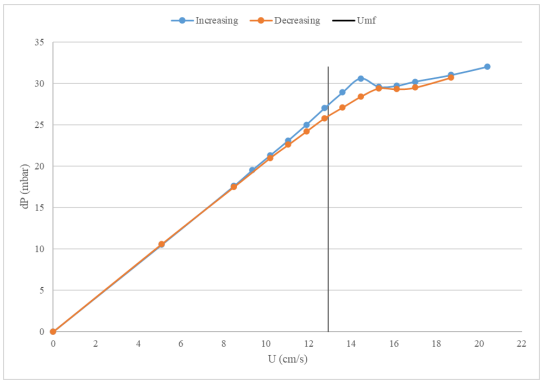

(a) 5 cm column

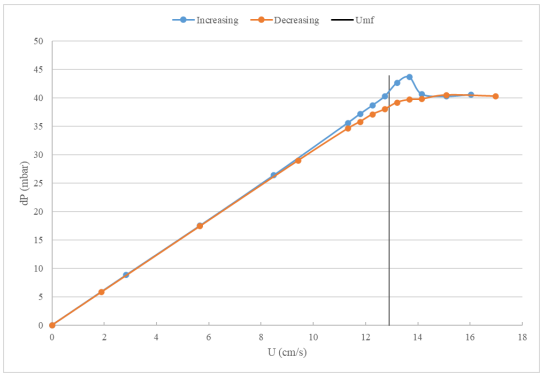

(b) 15 cm column

Figure 4.3: Fluidization velocity of a 0.5 mm particles

4.1.2. Python Analysis

The Python script, described in section 3.2, is verified through analysis of foam spheres of a known diameter, referred to as phantoms. Three phantoms of varying sizes were placed in a 5 cm column filled with 0.5 mm particles. The bed was not fluidized. The projections of the phantoms undergo the same image processing as the bubbles. A random sample of 8 projections of each phantom are taken, and the average slice stacked d_{eq} was obtained. A summary of the phantom sizes obtained from the Python script can be seen in table 4.3. These differences could arise from beam hardening, x-ray scattering effects, or the thresholding during the image analysis. The error appears to increases as the size of the particle decreases. The minimum $d_{eq,inj}$ for all systems was 20 mm, so the error from the script is considered minimal.

Diameter (mm)	Avg $d_{eq,Python}$ (mm)	Error (%)
25	24	3.7
15	13	11
10	7.8	22

Table 4.3: Comparison of actual and measured diameter of phantoms

4.1.3. Volume of Gas Injection

Based on the volume of gas injected into the nozzle, the corresponding spherical $d_{eq,inj}$ can be calculated. The average d_{eq} of the bubbles after injection for certain t_{inj} were calculated and compared to



Figure 4.4: Sample of 25, 15, 10 mm phantoms after image analysis

the $d_{eq,inj}$ for the various systems and levels of background fluidization, seen in Figures 4.5 and 4.6.

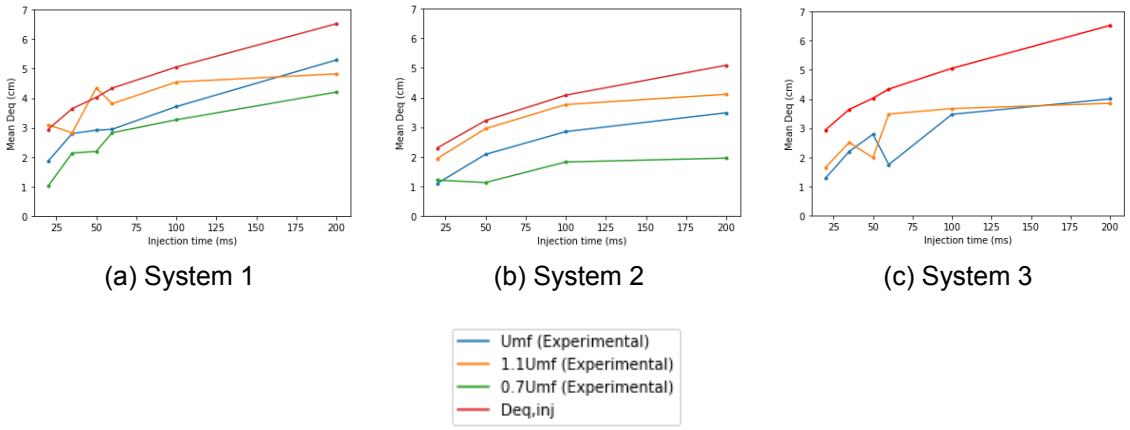

(a) System 1 (b) System 2 (c) System 3

Figure 4.5: Comparison of the $d_{eq,inj}$ to the average measured d_{eq} based on t_{inj} and U in the 15 cm column

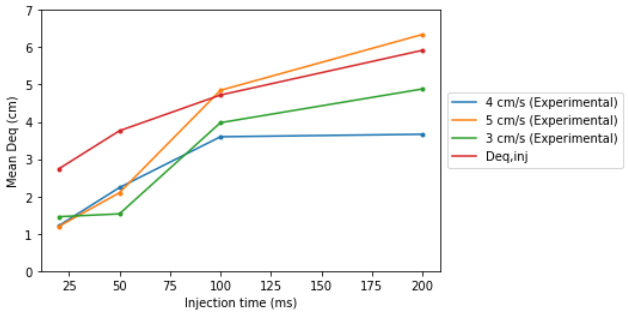

Figure 4.6: Comparison of the $d_{eq,inj}$ to the average measured d_{eq} based on t_{inj} and U in the 5 cm column

In the 15 cm column, the average image processed d_{eq} is consistently smaller compared to the $d_{eq,inj}$. A possible explanation for this could be a portion of the injected gas dissipated into the bed rather than contributed to the formation of the bubble. A study of single bubble injections from Boyce et al. found a large portion of gas would enter the dense bed, especially at high t_{inj} [14].

In the 5 cm column, the average image processed d_{eq} for the 3 and 4 cm/s are also consistently smaller compared to the $d_{eq,inj}$. However, the average image processed d_{eq} for the 5 cm/s is greater than the $d_{eq,inj}$. This behavior is observed in the study by Riechmann, which attributes the larger d_{eq} to particles entering the bubble [5]. Additionally, this behavior is seen at the highest level of background fluidization and $d_{eq,inj}$ for the 5 cm column, and the injected gas formed into slugs with a cylindrical volume. The difference in shapes utilized to measure the volumes may also account for some of these difference.

Overall, the average image processed d_{eq} aligns with behavior previously observed in similar experiments.

4.2. Representative Cases

This section focuses on detailing the motion of a selection of representative bubbles from each system. Only a select few are highlighted in this section, but for each $d_{eq,inj}$ at every system and level of

background fluidization, three processed representative bubbles can be seen in Appendix B.1.

First, a selection of five projections from the detectors are presented. The time between the selected frames varies. More projections are available in Appendix B.1. The frames selected in this section contain the formation stage, the stable region, and the unstable region, where applicable. The dead pixels were removed, and the projections were enhanced by increasing contrast and brightness. The image processed representative bubbles are then presented. The processed representative bubbles use red dots to represent the center of mass along the x- and y-axes, a blue line for the 3rd order B-spline, and black circles for the slice stacked d_{eq}. The framing around the selected bubbles is cropped to the approximate width of the projection frame of 5 cm. For some of the representative projections, it appears as though the bubble suddenly changes path. This is often due to a breakup off the bubble that is too small or dissipates too quickly to be accurately captured.

The bubbles are not consistently symmetrical. For example, when a bubble splits, two detectors may capture the split, while the third would only discern a single bubble shape. However, this phenomenon is expected to affect the projections equally, as the bubble split is assumed to be random. Therefore, axis symmetry is assumed.

4.2.1. 2D Projections

D_{bed}: 15 cm, d_p: 0.2 mm, Q: 35 m/s [System 1]

The figures in table 4.4 show the motion of a representative bubble for system at 0.7Umf with a $d_{eq,inj}$ of 4.0 cm. The bubble shrunk, which is expected for this fluidization level. The injected gas is expected to dissipate into the system rather than contribute to the formation of the bubble. The first breakup of the bubble is visible, and the offshoot bubble dissipated into the system. This breakup appears to be the described ”roof collapse”. The bubble continued to break up as it traversed the column, causing the reduction in volume of the bubble.

The figures in table 4.5 show a similar setup to the previous figures, where the level of background fluidization is at Umf. This bubble is an example of the expected behavior of a bubble in these conditions. The bubble stayed within the center of the column and does not experience drastic volume changes. The bubble at Umf does not lose as much volume as the bubble at 0.7Umf, which is expected, nor does the bubble in this example coalesce, which is expected at 1.1Umf.

The figures in table 4.6 shows a similar system, where the level of background fluidization has been increased to 1.1Umf. In the second image, a background bubble coalesced with the injected bubble, which is expected behavior of bubbles at U $\geq$ Umf. Increased stochastic bubble behavior and motion is expected at this fluidization level, making this bubble a representative example of bubbles at this fluidization level in this system.

For these bubbles, bluff bodies were observed during the rising stage for nearly all of the $d_{eq,inj}$ and fluidization levels.

The processed representative bubbles, seen in Figures 4.7.A-.C, allow for a clear understanding of how the path and d_{eq} change. In these figures, the formation stage is more difficult to distinguish, as it blends with the beginning of the rising stage.

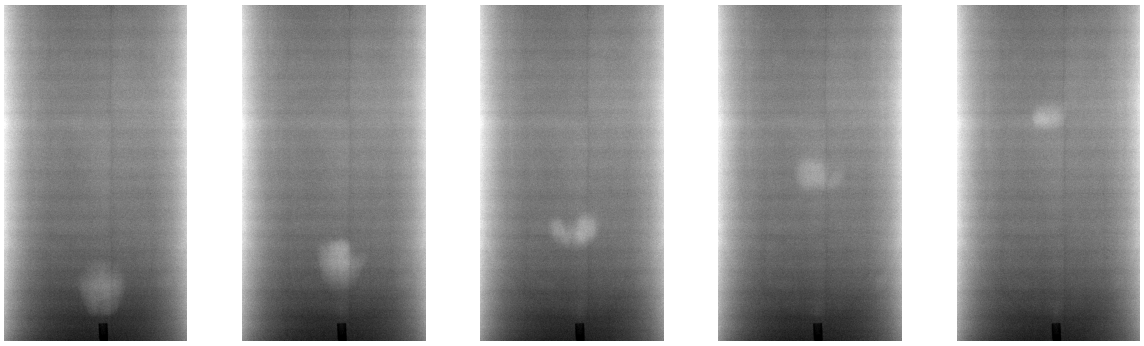

Table 4.4: 5 frames from single bubble motion in System 1, U: 0.7Umf, $d_{eq,inj}$: 4.0 cm, f: 30 Hz
More frames in Figure B.1

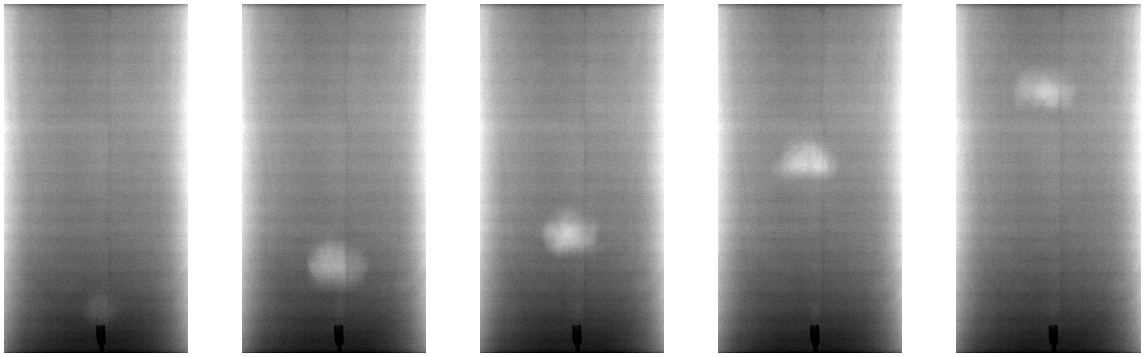

Table 4.5: 5 frames from single bubble motion in
System 1, U: Umf, $d_{eq,inj}$: 4.0 cm, f: 30 Hz
More frames in Figure B.2

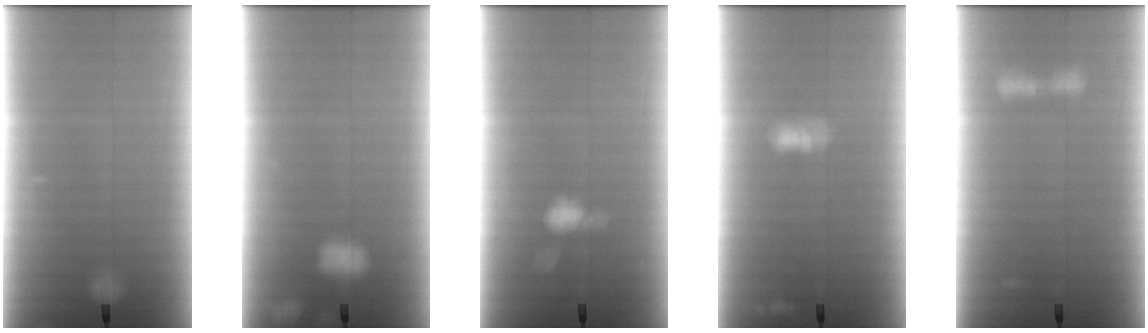

Table 4.6: 5 frames from single bubble motion in
System 1, U: 1.1Umf, $d_{eq,inj}$: 4.0 cm, f: 30 Hz
More frames in Figure B.3

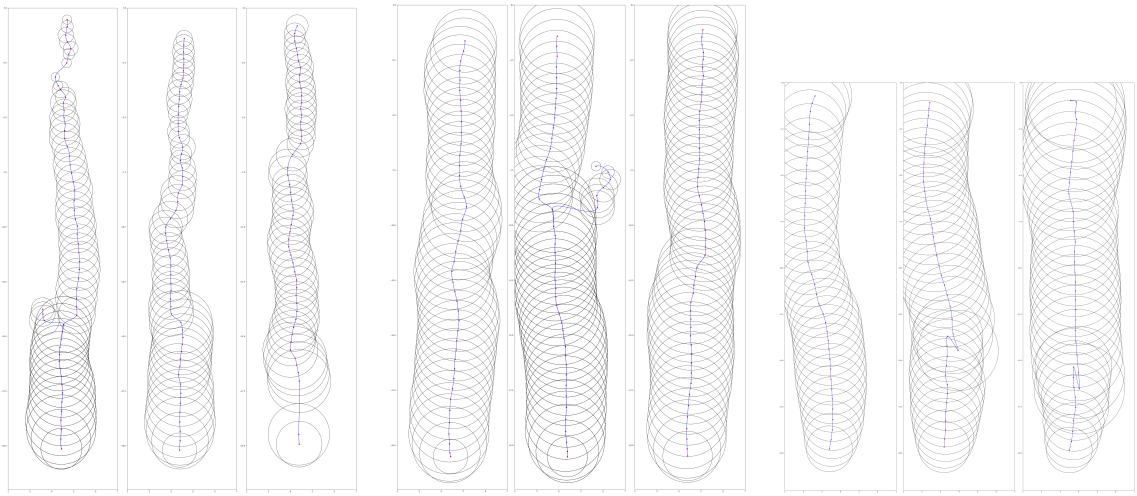

(a) 0.7Umf (b) Umf (c) 1.1Umf

Figure 4.7: Processed bubble projection
System 1, $d_{eq,inj}$: 4.0 cm

D_{bed}: 15 cm, d_p: 0.2 mm, Q: 17 m/s [System 2]

Table 4.7 shows the bubbles with $d_{eq,inj}$ of 4.0 cm for system 2, which is comparable to the representative case of table 4.5. Overall, the behavior of the bubbles when the level of background fluidization

varied was similar for both systems. The bubbles found for system 2 were relatively smaller in measured d_{eq} compared to system 1. A study of single bubble injections from Boyce et al. observed a portion of gas would enter the dense bed, especially at high t_{inj} [14]. Because the injection velocity of system 2 is less than system 1, longer t_{inj} is necessary to achieve the same $d_{eq,inj}$, which would allow for more gas to leak into the bed. Relatively smaller bubbles in system 2 for the same $d_{eq,inj}$ as system 1 was observed for all cases.

During the formation of bubbles, the bubble was observed to detach from the nozzle prior to the completion of the t_{inj}, observed in the 2nd frame of table 4.7. Even though the bubble detached, the bubble continued to receive the gas from the nozzle. The detachment of the bubble from the nozzle forces the gas to pass through the fluidized bed prior to reaching the bubble, likely allowing for further escape of the gas into the bed. This may also explain the lesser measured d_{eq} in system 2 compared to system 1.

Within system 2, the overall length of the stable region appears longer. However, when comparing the total length of the stable region for the different systems, the total length is similar. The differences in injection velocity seems to affect the formation stage more than the rising stage.

The bubble appears to suddenly change direction, especially in the processed projections. These sudden changes are associated with bubble breakup and coalescence that was not detected or filtered during image processing.

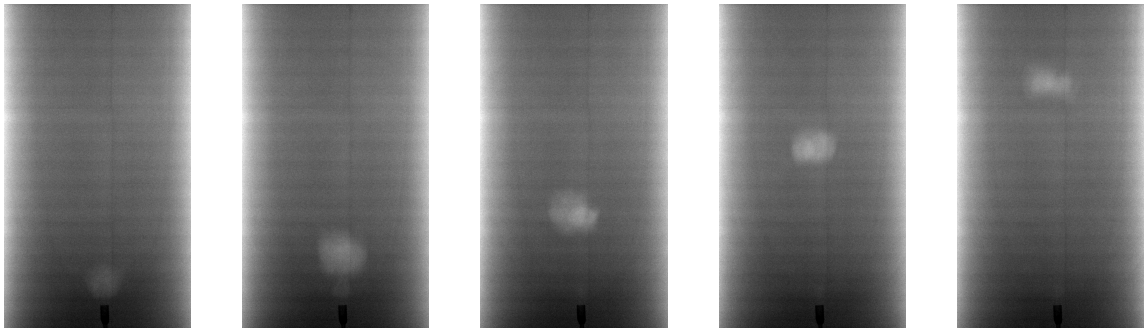

Table 4.7: 5 frames from single bubble motion in System 2, U: Umf, $d_{eq,inj}$: 4.0 cm, f: 30 Hz
More frames in Figure B.4

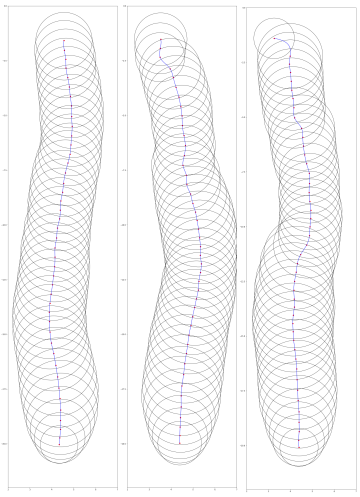

Figure 4.8: Processed bubble projection
System 2, U: Umf, $d_{eq,inj}$: 4.0 cm

D_{bed}: 15 cm, d_p: 0.5 mm, Q: 35 m/s [System 3]

For the following system, Umf and 1.1Umf were analyzed. Experiments were conducted at 0.7Umf, but the injected gas did not form bubbles. Intermittent bubbling was present at 1.1Umf, and the amount

of bubbles produced from the background fluidization was not equivalent to the amount of background bubbles compared to the systems with smaller particles.

For system 3, at $d_{eq,inj}$ of 4.3 cm at Umf, the bubbles are observed to consistently move to one side. This behavior was not observed in other experiments and is believed to be an experimental error. This set of experiments have been excluded from further analysis.

Table 4.8 can be compared to system 1 with the same conditions as in table 4.5. When comparing the representative bubbles, the bubbles are similar in size and develop a bluff body as the bubble traverses the column. The bubble for system 3 seems to have less breakage than system 1, which may be attributed to the differences in particles.

As discussed in section 2.1.2, splitting is an important factor in Geldart A particles but is negligible in Geldart B particles [23]. The bubbles in systems that utilized the 0.2 mm particles, which are classified as Geldart A/B, may have been reaching a maximum available volume that can be supported by the particles. The 0.2 mm particles would ”rain” down and split the bubbles through roof collapse in these cases, causing more breakup to occur for this particle size. This ”raining” effect has been previously observed for these 0.2 mm particles [5]. The image processed representative bubbles, seen in Figure 4.9, also suggest the breakup of the bubble is less common in system 3, as the processed bubbles show less small bubbles and less apparent sudden path changes. Sudden path changes are expected to be caused by break up of bubbles that cannot be accurately captured in the projections.

The difference in cohesiveness and size of the particles may affect the bubble cloud, as these factors could affect how the particles interact. These interactions may hinder the formation of the cloud and cause a less dense cloud to form, which would affect the interactions of the bubble and emulsion phase.

Table 4.9 shows the bubbles at $d_{eq,inj}$ of 6.5 cm. These bubbles were selected because this experiment clearly demonstrates a phenomenon that was observed at the frame rate of 65 Hz, both in systems 1 and 3. This behavior was not observed at the low frame rate, 30 Hz. As the gas was injected, the bubble is cut off prematurely, causing the formation of two bubbles: a ”large” and ”small” bubble. The two bubbles affect image processing, and the small bubble is excluded from the data presented in this and the following sections. The study by Boyce et al. observed the injection of two bubbles within their system at larger $d_{eq,inj}$, theorizing the formation of the large bubbles pushed particles down and in toward the injection site, causing the particles to cut off the bubble prematurely and forming two bubbles [14]. In these experiments, this phenomenon occurred when $d_{eq,inj} \geq 4.3$ cm for systems 1 and 3 and was most noticeable below and at Umf.

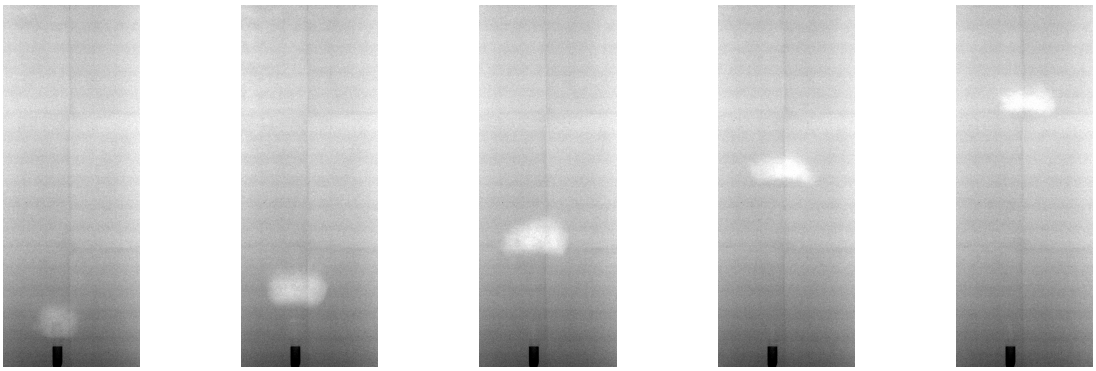

Table 4.8: 5 frames from single bubble motion in
System 3, U: Umf, $d_{eq,inj}$: 4.0 cm, f: 30 Hz
More frames in Figure B.5

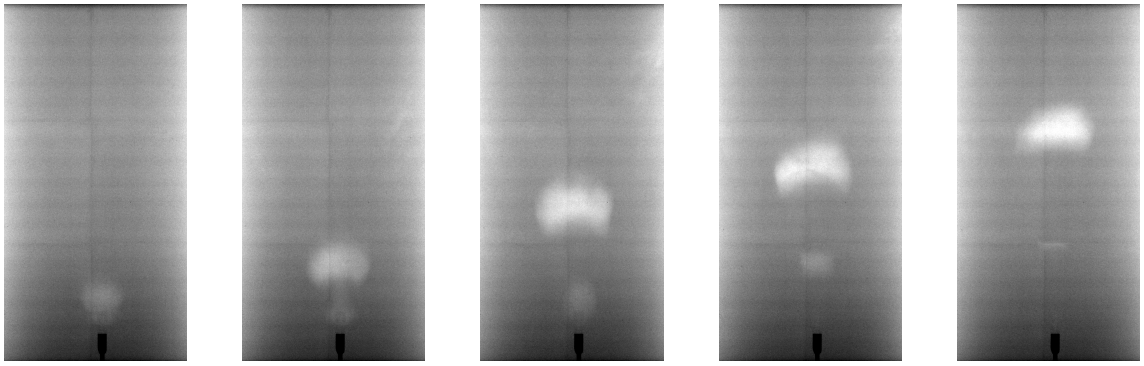

Table 4.9: 5 frames from single bubble motion in
System 3, U: Umf, $d_{eq,inj}$: 6.5 cm, f: 65 Hz
More frames in Figure B.6

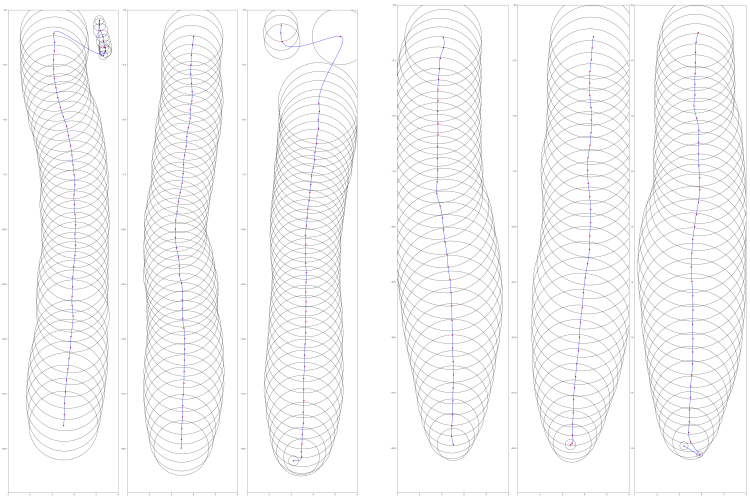

(a) $d_{eq,inj}$: 4.0 cm (b) $d_{eq,inj}$: 6.5 cm

Figure 4.9: Processed bubble projection
System 3, U: Umf

D_{bed}: 5 cm, d_p: 0.2 mm, Q: 26 m/s [System 4]

Table 4.10 shows a bubble of $d_{eq,inj}$ of 3.8 cm for system 4, which can be compared to the Tables 4.5 and 4.7. The bubbles in a 5 cm column experience more wall effects and slugging than bubbles of similar volumes in the 15 cm column. The bubble will often touch the sides of the column as it forms and begins to rise. For the representative bubble chosen for this system, the bubble is observed to slug but still dissipate before exiting the projection frame. The dissipation prior to exiting the frame suggests the volume of gas injected was not enough to sustain bubble size as it rose through the column.

At larger $d_{eq,inj}$, the slugging became more apparent. Typically, a slug would release from the nozzle and reach the walls of the column, forming a cylindrical slug in 3D. The slug then appeared to ”stall” for a brief period as gas continued to be injected into the bubble and the particles ”rained” through the roof of the bubble. Within the processed images, the circles representing the bubble appear to overlap, which is associated with the stalling of the slug. The slug then traversed the column, often breaking and coalescing. The calculations for the spherical $d_{eq,inj}$ tend to inaccurately describe the cylindrical slugs by under estimating the size.

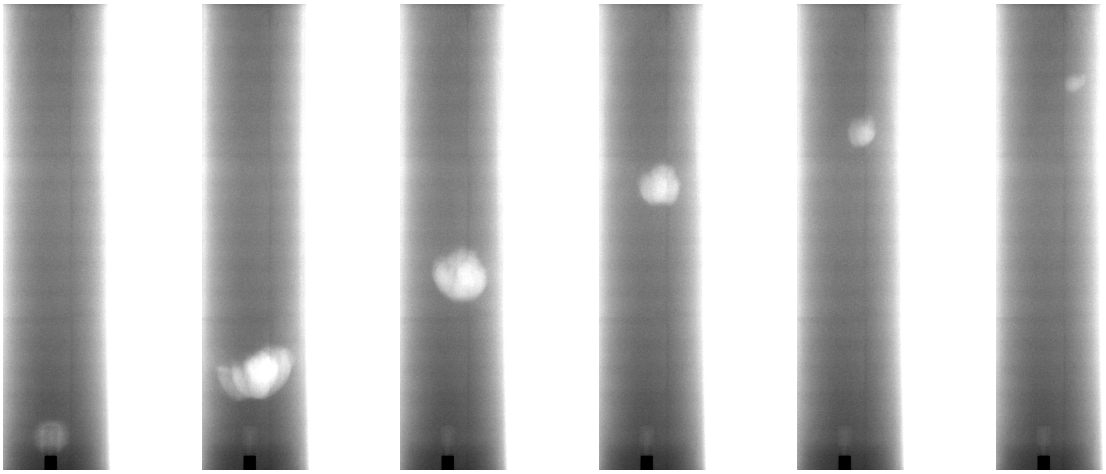

Table 4.10: 5 frames from single bubble motion in System 4, U: 4 cm/s, $d_{eq,inj}$: 3.8 cm, f: 75 Hz
More frames in Figure B.7

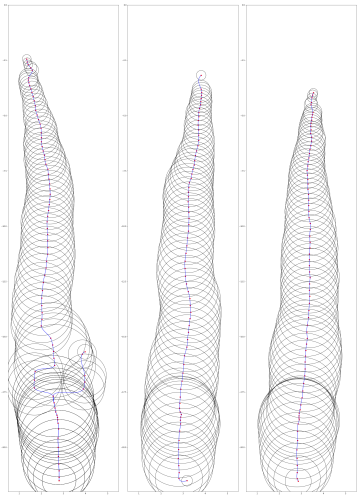

Figure 4.10: Processed bubble projection
System 4, U: 4 cm/s, $d_{eq,inj}$: 3.8 cm

4.2.2. 3D Reconstruction

The processing of the 2D projections for a 3D reconstruction was completed for a selection of bubbles in the 5 and 15 cm columns. These 3D reconstructions utilized script designed by A.B.M Graas [16]. Red represents a high gas fraction, while blue represents a low gas fraction. The provided script was developed for a 5 cm column, and the parameters within the script were set for a 5 cm column. A reconstruction of a 15 cm column that has been cropped to 5 cm was done. Fine tuning of the parameters may improve the image quality and reduce noise within the 3D reconstruction of the 15 cm column.

A select bubble from the system 4 at 4 cm/s and $d_{eq,inj}$ of 3.8 cm was reconstructed, as seen in Figure 4.11. A turn around of the 3D column can be seen in Appendix B.3.2. Figure 4.11 shows a selection of 5 frames from the 3D reconstruction of the bubble motion traversing the column. The reconstructed length is shorter than the actual frame height, approximately 14 cm. Asymmetry in a bubble is observed in this example.

A select bubble, from system 1 at Umf and $d_{eq,inj}$ of 4.0 cm, was also reconstructed, seen in Figure 4.12. The diameter of the column was 15 cm and the projection frame was cropped to 5 cm in total width around the nozzle. This 3D reconstruction is expected to have more noise and would need further

adjustments to the parameters to achieve clear reconstructions. The increased noise reflects the need for optimization to accurately characterize this cropping.

These 3D reconstruction allows for asymmetry and the bubble cloud to be more visible, which were relatively more difficult to process in 2D. Within the scope of this research, the overall processing of the 3D reconstructions was limited and was focused on establishing the use of the script within TU Delft. Calculations and other characterizations of the 3D reconstructions have been left to further research and investigation.

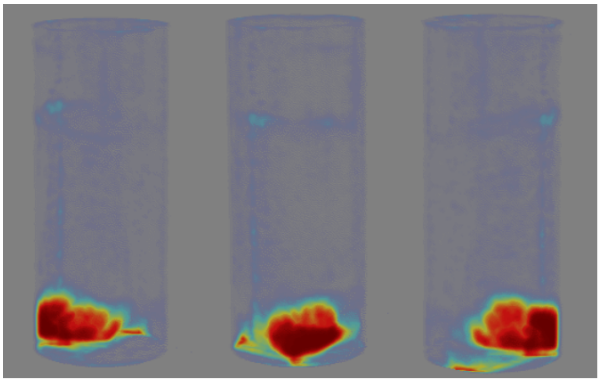

Figure 4.11: 3D Reconstruction of System 4, U: 4 cm/s, $d_{eq,inj}$: 3.8 cm, f:: 75 Hz

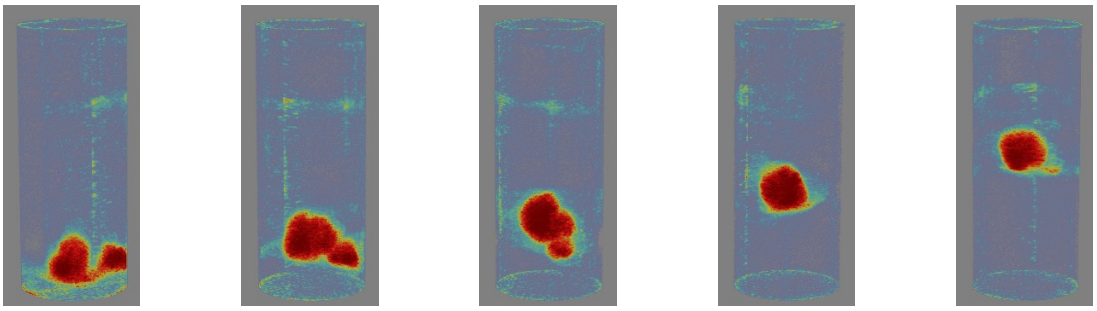

Table 4.11: 5 frames from single bubble motion in System 4, U: 4 cm/s, $d_{eq,inj}$: 3.8 cm, f: 75 Hz
More frames in Figure B.15

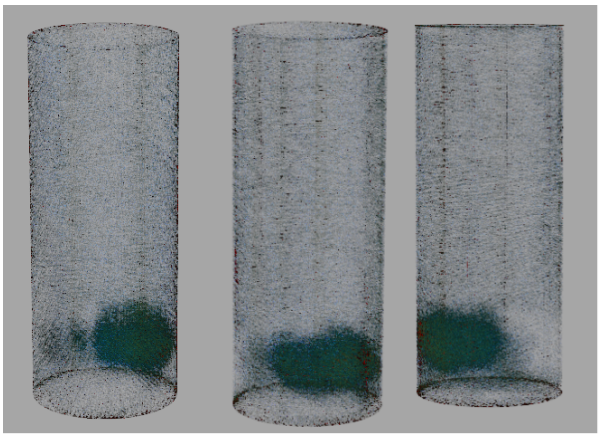

Figure 4.12: 3D Reconstruction of System 1, U: Umf, $d_{eq,inj}$: 4.0 cm, f: 65 Hz

4.3. Formation Stage

This section focuses on describing the formation stage. Due to the limited frame rate, the formation of a bubble was typically less than 5 frames at 65/75 Hz, which is insufficient for detailed descriptions.

The end of the formation stage is difficult to discern from the beginning of the rising stage when observing the trajectories of the bubbles. However, the formation stage becomes more apparent through a statistical overview of the bubbles.

The statistical overview of the bubbles took the average of 30 bubbles from 3 angles, a total of approximately 90 bubbles. The measured d_{eq} was taken over the normalized height of the bubble for the projection frame. The figures within this section define the normalized height as the distance of center of mass of the bubble in the vertical axis from the top of the nozzle until the bubble exits the projection frame, approximately 22 cm in total. The bubbles are averages and categorized by the normalized height in increments of 0.05. The definition of the normalized height in this section is used for ease of visualization. Error of the averages is taken along the horizontal and vertical axes. In some instances, the error appears large, especially near the top of the frame. The large error associated with the top of the frame is likely due to the frame capturing the bubble partially as it exits the frame.

Additionally, for systems 1 and 3, when the $d_{eq,inj}$ is or more than 4.3 cm, two bubbles were observed. For the figures in this section, the secondary, smaller bubble has been excluded. The figures containing the information from the smaller bubble can be found in Appendix B.2. The first plateau of d_{eq} then sudden increase to another plateau has been attributed to the cut off of the larger bubble at the injection point due to particle motion, described by Boyce et al. [14]. The smaller bubble tends to dissipate relatively quickly. The method of image processing led to the d_{eq} of the smaller bubble to be accounted for at the normalized height. After the smaller bubble had dissipated, the sudden large increase in d_{eq} was caused by the image processing solely accounting for the larger bubble.

The formation of the bubble in these systems can be seen as the d_{eq} steadily increases from a normalized height until the end of the formation stage (H_F). When the d_{eq} reaches a peak or stabilizes, the rising stage has begun. Once the bubble is established through the formation stage, the behavior is expected to be similar to bubbles of equal volume throughout the rising stage. The determination of H_F in this section is visually approximated. The statistical overviews were typically observed to have a positive slope (formation stage), a plateau (rising stage, stable region), and a negative slope/variance along the plateau (rising stage, unstable region). The approximate normalized height at the end of the positive slope was taken as the H_F.

D_{bed}: 15 cm, d_p: 0.2 mm, Q: 35 m/s [System 1]

Figure 4.13 is the d_{eq} of the bubble over the normalized height of the column. The figures within this section do not include the previously described secondary bubble that formed due to the particles prematurely cutting of the injected bubble. Figure B.12 includes these secondary bubbles.

Overall, the bubbles at 1.1Umf were similar to the $d_{eq,inj}$, and the bubbles at Umf and 0.7Umf were typically below $d_{eq,inj}$. The bubbles at 1.1Umf tended to increase in d_{eq} due to coalescence, while the bubbles at 0.7Umf tended to decrease in d_{eq}, likely due to shedding. The bubbles at Umf generally maintained the same d_{eq}.

Table 4.12 summarizes the H_F approximated visually. In general, the H_F increases as the $d_{eq,inj}$ increases. The bubble is observed to release from the nozzle and continue to receive the injected gas, especially as t_{inj} increases. The continued injection of gas into the bubble even though the bubble released from the nozzle leads to the continued growth of measured d_{eq} as the bubble traverses the column.

$D_{eq,inj}$ (cm):	2.9	3.6	4.0	4.3	5.0	6.5
0.7Umf	0.1	0.15	0.1	0.2	0.25	0.35
Umf	0.2	0.15	0.1	0.15	0.3	0.4
1.1Umf	0.05	0.15	0.25	0.25	0.35	0.35

Table 4.12: Visually approximated normalized H_F for system 1 at various U and $d_{eq,inj}$

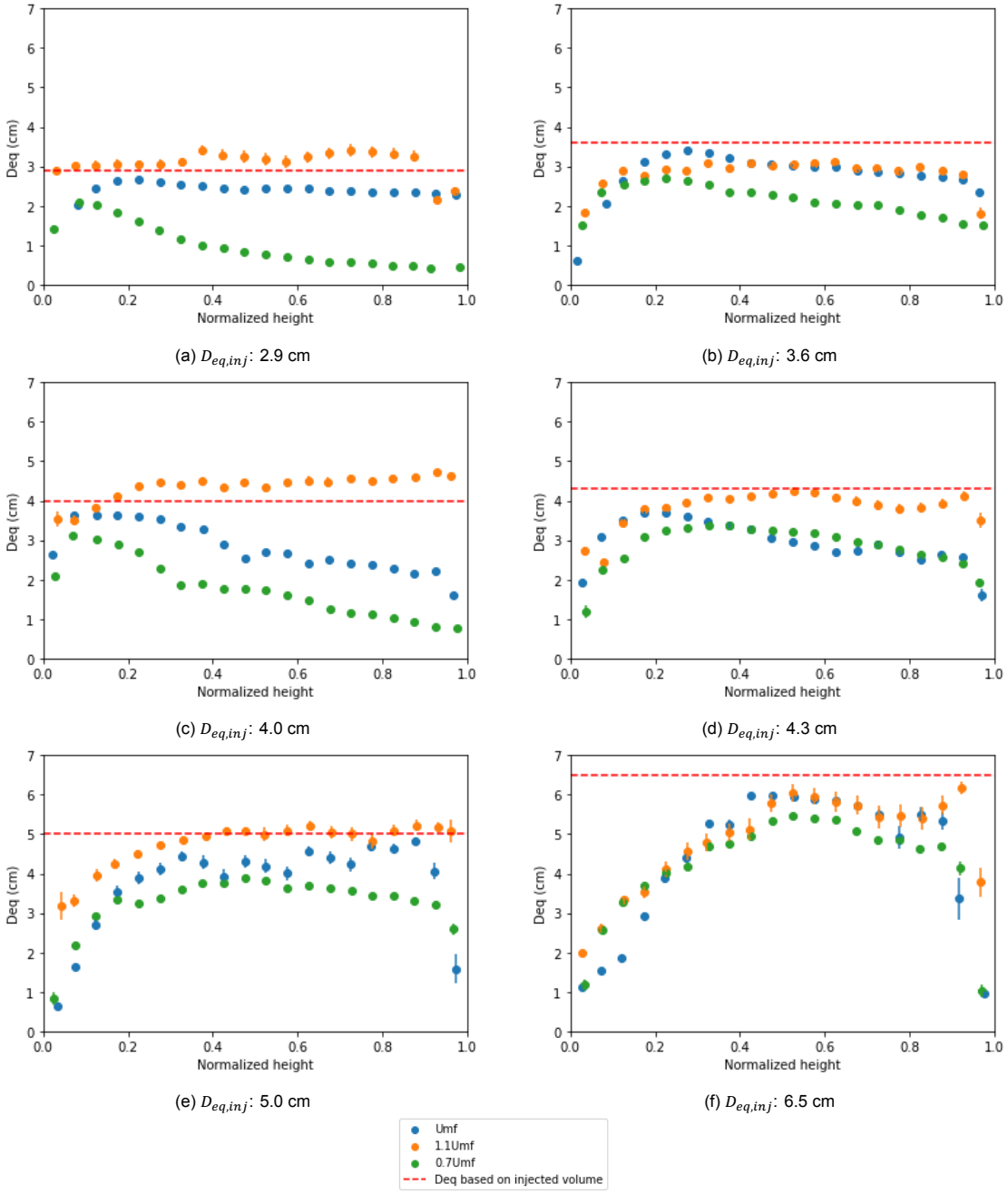

(a) $D_{eq,inj}$: 2.9 cm

(b) $D_{eq,inj}$: 3.6 cm

(c) $D_{eq,inj}$: 4.0 cm

(d) $D_{eq,inj}$: 4.3 cm

(e) $D_{eq,inj}$: 5.0 cm

(f) $D_{eq,inj}$: 6.5 cm

Figure 4.13: d_{eq} over the normalized height of the projection frame for System 1

D_{bed}: 15 cm, d_p: 0.2 mm, Q: 17 m/s [System 2]

The statistical overview of the d_{eq} over the normalized height of the column can be seen in Figure 4.14 and the H_F is summarized in table 4.13.

Systems 1 and 2 can be compared. The H_F for system 2 had a tendency to be slightly higher compared to system 1 for the same $d_{eq,inj}$. A possible explanation for this behavior may be related to the differences in injection velocity and t_{inj}. Bubbles in system 2 may have detached from the nozzle prior to the completion of gas injection more frequently than in system 1. The gas would continue to contribute the bubble formation as the bubble traversed the column, resulting in bubble growth at higher normalized heights compared to system 1. The measured d_{eq} was observed to be less for system 2 than system 1 at the same $d_{eq,inj}$. This behavior can be explained similarly. After the bubble detaches, the gas must traverse a longer distance in system 2 than system 1 to contribute to the bubble formation. This longer distance would allow for gas to leak more readily into the emulsion phase.

The injection velocity is also expected to affect the development of a cloud around the bubble, which would in turn affect the interactions of the cloud to the bulk. For a similar $d_{eq,inj}$ to be achieved in both systems, system 2 requires a longer t_{inj} because the injection velocity is less for system 2 than system 1. The surrounding particles by the bubble may be less compact around the bubble, allowing for the bubble to more readily shed gas into the emulsion phase.

The different stages and regions are well highlighted in Figure 4.14.B at 0.7Umf. The average measured d_{eq} increased (formation), plateaued (stable), and then decreased (unstable). This behavior consistently occurred for approximately 30 bubbles at 3 angles with little standard deviation, showing a trend in the behavior of the bubbles.

$D_{eq,inj}$ (cm):	2.3	3.2	4.0	5.1
0.7Umf	0.1	0.1	0.1	0.15
Umf	0.1	0.1	0.15	0.2
1.1Umf	0.1	0.15	0.4	0.2

Table 4.13: Visually approximated normalized H_F for system 2 at various U and $d_{eq,inj}$

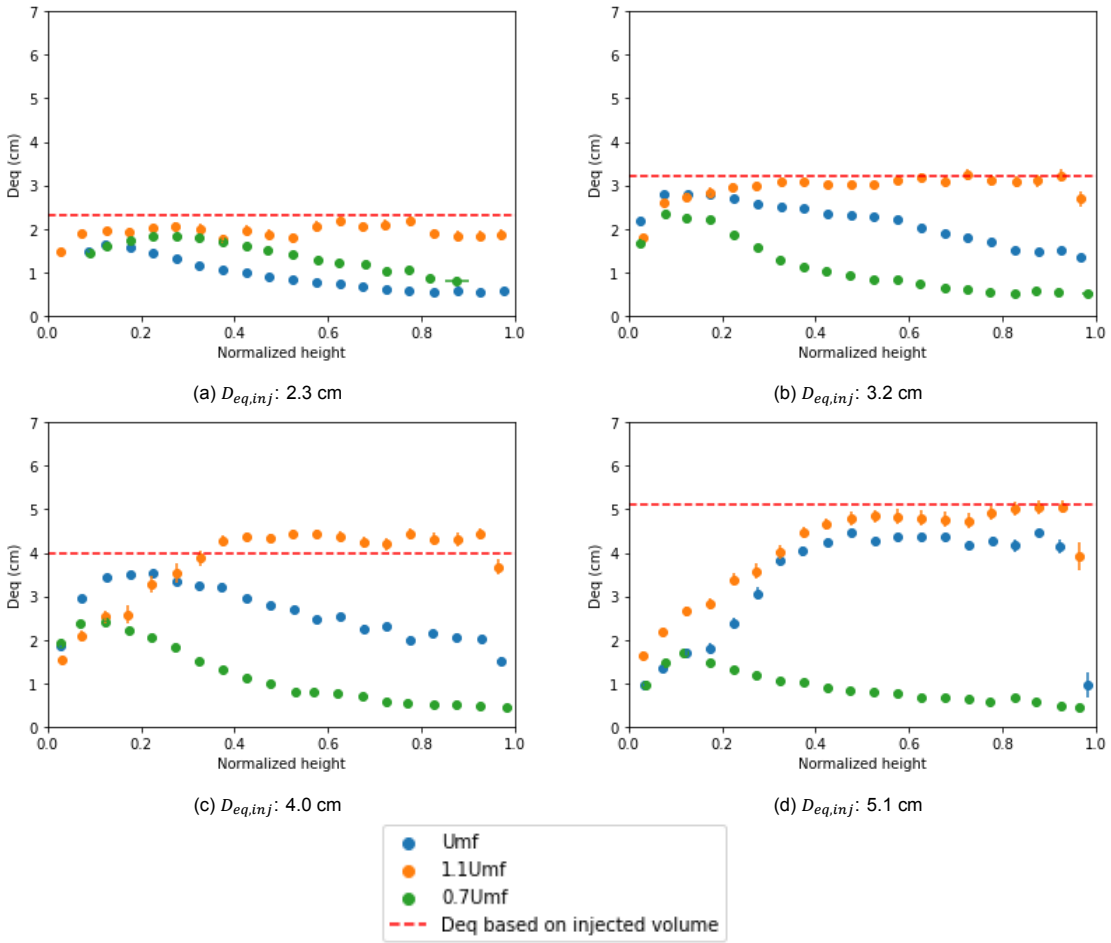

(a) $D_{eq,inj}$: 2.3 cm

(b) $D_{eq,inj}$: 3.2 cm

(c) $D_{eq,inj}$: 4.0 cm

(d) $D_{eq,inj}$: 5.1 cm

Figure 4.14: d_{eq} over the normalized height of the projection frame for system 2

D_{bed}: 15 cm, d_p: 0.5 mm, Q: 35 m/s [System 3]

For system 3, the statistical overview of the d_{eq} over the normalized height of the column can be seen in Figure 4.15, and the H_F is summarized in table 4.14. The figures within this section do not include the secondary bubble and are included in Figure B.13.

System 1 and 3 can be compared, where the major difference is the particles. For certain $d_{eq,inj}$, the measured d_{eq} appears to differ slightly between the systems. In general, the measured d_{eq} of the

bubbles at Umf for system 1 are larger than system 3, likely caused by the difference in materials of the particles. The different particles may have allowed for more gas to leak into the bed, rather than attribute to the growth of the bubble. The d_{eq} after the formation stage was consistently smaller for system 3 than system 1.

System 3 can be compared to system 1. System 1 and 3 have similar H_F, with the exception of the largest $d_{eq,inj}$. The large difference in the $d_{eq,inj}$ of 6.5 cm may be due to the differences in particle size and interactions. The forming bubble was cut off at a smaller d_{eq} for system 3 than system 1, which can be seen as the difference in the first plateau in Figures B.12 and B.13. The bubble in system 1 would traverse higher in the column while still receiving the injected gas, causing the formation stage to appear relatively longer for system 1 compared to system 3.

$D_{eq,inj}$ (cm)	2.9	3.6	4.0	4.3	5.0	6.5
Umf	0.15	0.15	0.20		0.20	0.20
1.1Umf	0.15	0.20	0.30	0.20	0.20	0.15

Table 4.14: Visually approximated H_F for system 3 at various U and $d_{eq,inj}$

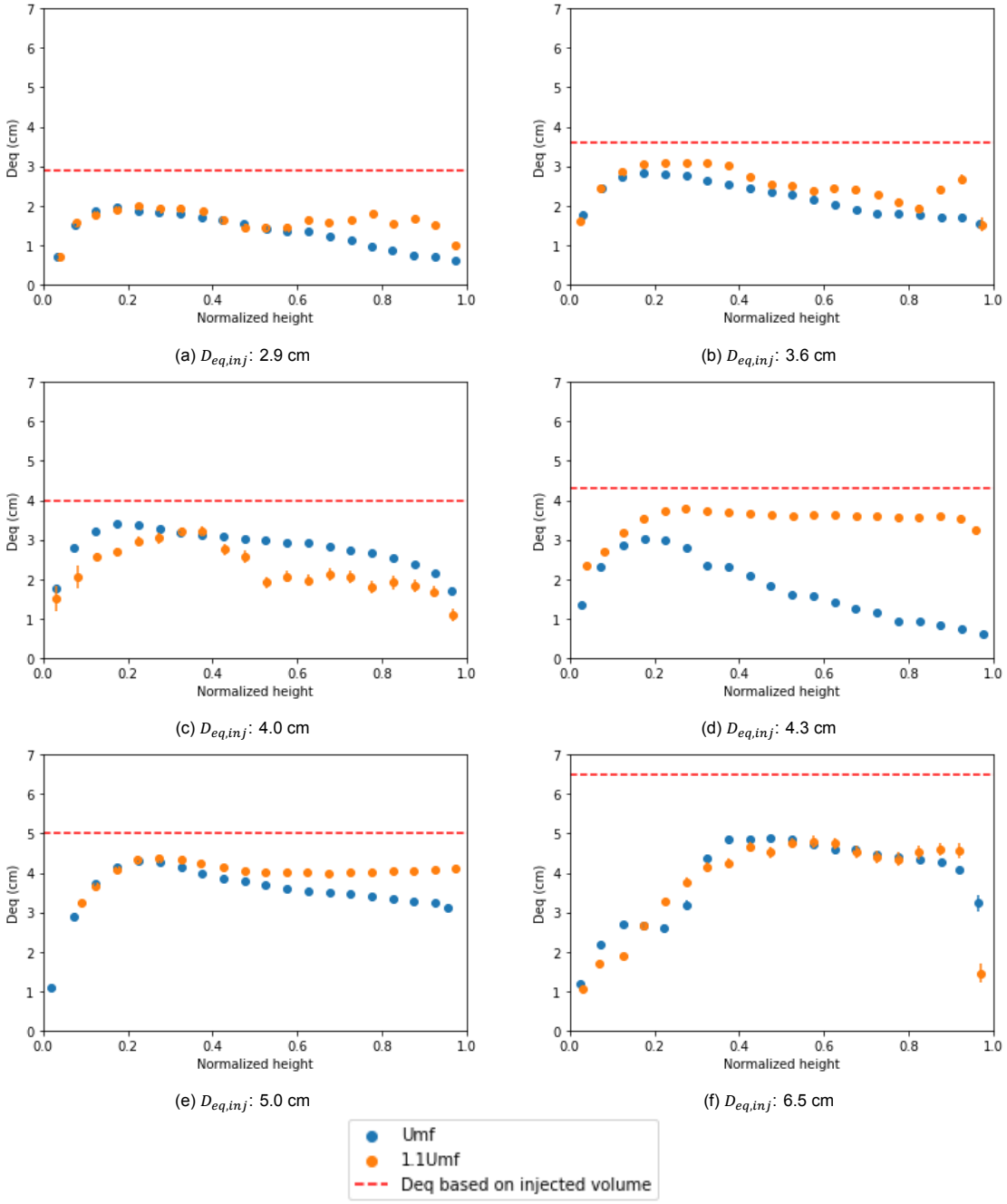

(a) $D_{eq,inj}$: 2.9 cm

(b) $D_{eq,inj}$: 3.6 cm

(c) $D_{eq,inj}$: 4.0 cm

(d) $D_{eq,inj}$: 4.3 cm

(e) $D_{eq,inj}$: 5.0 cm

(f) $D_{eq,inj}$: 6.5 cm

Figure 4.15: d_{eq} over the normalized height of the projection frame for system 3

D_{bed}: 5 cm, d_p: 0.2 mm, Q: 26 m/s [System 4]

The statistical overview of the d_{eq} over the normalized height of the column can be seen in Figure 4.16, and the H_F is summarized in table 4.15.

Slugging is expected to affect a multitude of aspects of the bubbles, including the different regions. The slug forms as gas is injected into the system, engulfing the width of the column. Slugs were not formed in the 15 cm column and were behavior exclusive to system 4.

System 4 can be compared to systems 1 and 2. Overall, the H_F is lower for system 4 compared to system 1 and 2. The slugs were observed to ”stall” in place as gas continued to be injected, lowering the formation stage of the bubble. The center of mass along the vertical axis of the overall slug would not readily increase as the gas contributed to the slow growth of the height of the cylindrical slug.

$D_{eq,inj}$ (cm):	2.7	3.7	4.7	5.9
0.7Umf	0.15	0.1	0.15	0.2
Umf	0.05	0.15	0.2	0.3
1.1Umf	0.25	0.15	0.2	0.3

Table 4.15: Visually approximated H_F for system 4 at various U and $d_{eq,inj}$

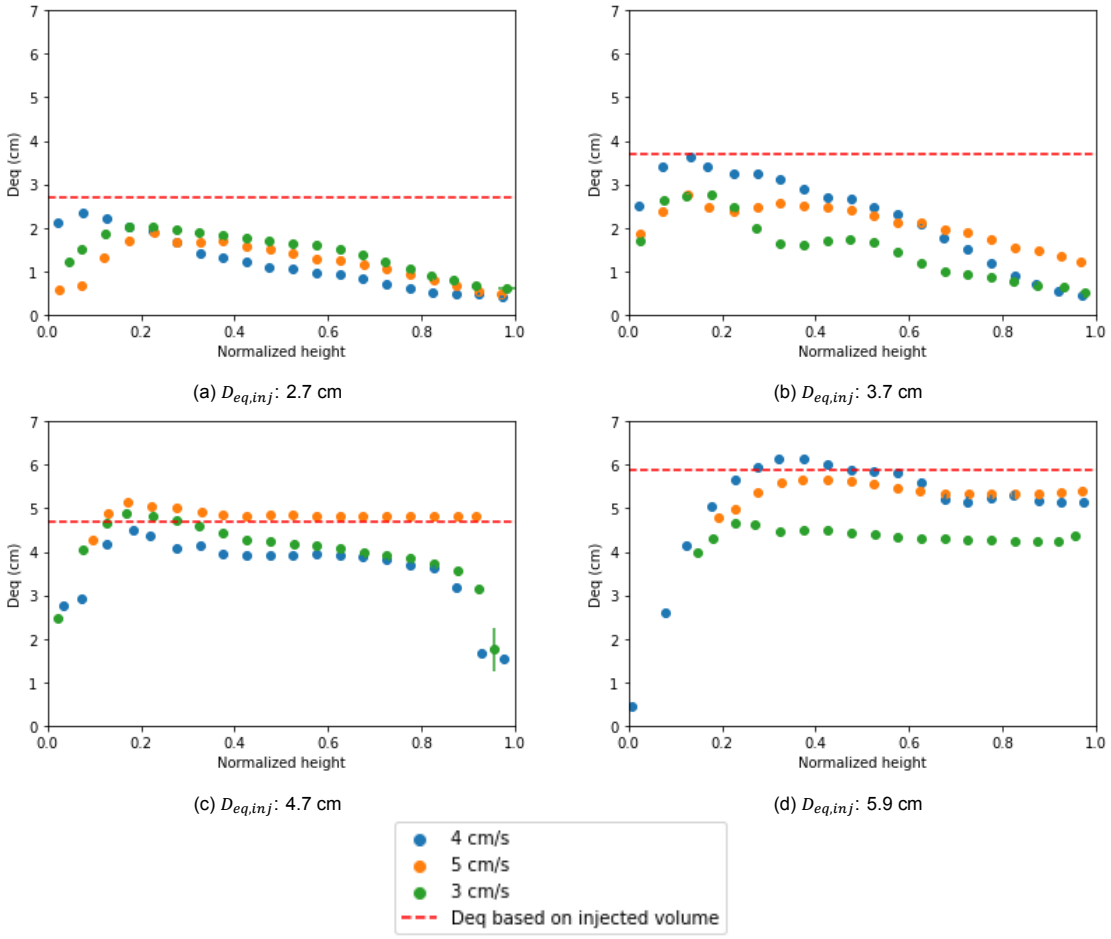

(a) $D_{eq,inj}$: 2.7 cm

(b) $D_{eq,inj}$: 3.7 cm

(c) $D_{eq,inj}$: 4.7 cm

(d) $D_{eq,inj}$: 5.9 cm

Figure 4.16: d_{eq} over the normalized height of the projection frame for system 4

4.4. Rising Stage

This section discusses the rising stage through the analysis of the bubble trajectory, which is the motion of the center of mass of the bubble along the horizontal and vertical axes. Within the rising stage, two regions were observed, labelled the ”stable” and ”unstable” regions. These region names are meant to describe the general apparent motion of the bubble. At the ”stable” region, the bubble motion exhibits relatively less natural variance along the x-axis, with little to no breakage or coalescence. At the ”unstable” region, the bubble will more readily break up and coalesce.

The changes in region are especially visible when plotting the trajectories. In this section, the figures show approximately 30 bubble trajectories for each plot. The trajectory plots are approximately 22 cm along the vertical axis and approximately 5 cm along the horizontal axis. The boundary between the formation stage and the rising stage, specifically the stable region, is not clear in the trajectories, as these phenomena occurred closely. The statistical overview of the bubble provides a more clear image on the border between the stages. The end of the stable region becomes more apparent in the trajectories, as the natural variance sharply widens when the ”unstable” region is reached. The normalized height at which the stable region ends (H_S) is taken. The unstable region can be caused by an increased breakup and coalescence as well as the motion of the emulsion phase. The H_S in

this section is visually approximated by observing the approximate normalized height where the bubble trajectories tend to increase in variance. The sudden increase in variance along the horizontal axis indicates the majority of bubbles move paths at that region. The H_S includes the formation stage.

The exact cause of the stable and unstable stages is difficult to decipher based on this research. The emulsion phase motion and bubble cloud are suspected to be the main contributors to the development of the stages.

For the Geldart A/B type particles, the stable region is not present when the level of background fluidization is greater than Umf because the background bubbles often predominated the system and often coalesced with injected bubbles during the formation stage.

Additionally, an estimate of the angle in degrees of the trajectory along the unstable region based on a center line is taken. An example of how the angles are found can be seen in Figure 4.17. The rectilinear section is visually approximated such that the stable region is within a lower and upper boundary. Within these boundaries, the horizontal center is found computationally, which is taken as the point at the end of the stable region. A center line through the point at the end of the stable region is drawn and continued to the end of the frame. The least and greatest points of trajectory along the horizontal axis is found, and straight lines are drawn to these points. The angles between the center line and the least and greatest points of trajectory along the horizontal axis are taken as θ_1 and θ_2, respectively.

This is repeated for all systems, $d_{eq,inj}$, and levels of background fluidization. The straight lines would often cut off portions of the trajectories, which may affect the accuracy of the angles. Additionally, the end of the stable region was estimated by eye, which may lead to additional inaccuracies. Overall, these angles of the trajectories provide information on the natural variance in the horizontal axis for the unstable region. A wider angle corresponds to more variance along the horizontal axis and in the unstable region.

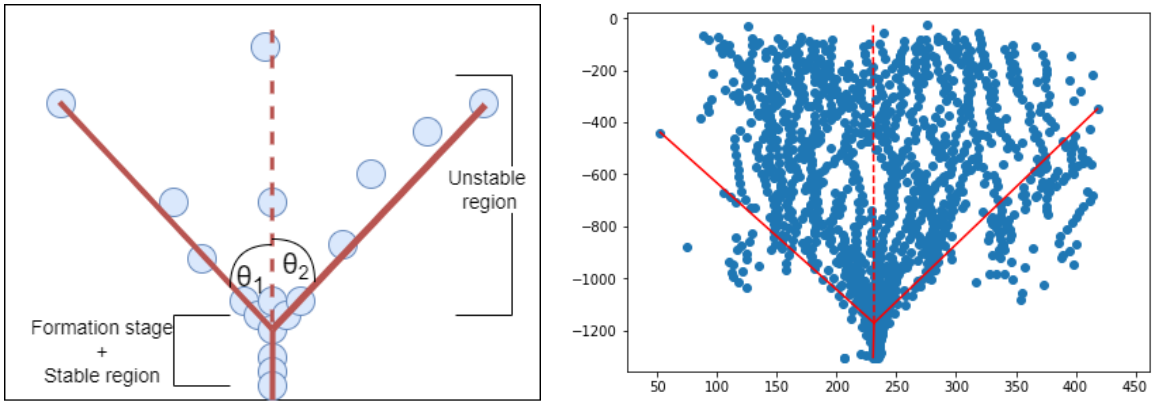

(a) Simplified diagram

(b) Example in pixles for Umf, $d_{eq,inj}$: 4.3 cm

Figure 4.17: Angle measurement of the unstable region

D_{bed}: 15 cm, d_p: 0.2 mm, Q: 35 m/s [System 1]

Table 4.20 contain the trajectories of the center of mass of the bubbles in the horizontal and vertical axes for 30 bubbles for the various levels of background fluidization and $d_{eq,inj}$.

The trajectories of the bubbles at 0.7Umf and Umf appear to stable and unstable regions. The unstable region is believed to form when the natural variance between the bubble increases, causing a widening of the overall shape of the center of mass figures. Table 4.16 shows the approximate H_S based on the individual bubble trajectories.

A bubble injected at 0.7Umf and a $d_{eq,inj}$ of 3.6 cm shows an increase in the natural variance of the bubbles, associated with H_S, occurred at a height of 4 cm above the nozzle. This corresponding to a normalized height of around 0.25. When referring to related statistical analysis of the same system, levels of background fluidization, and $d_{eq,inj}$ in Figure 4.13.B, the average d_{eq} of the bubbles began to decrease at the normalized height of approximately 0.25 to 0.3, signaling H_S. A comparison between the approximate H_S based on the statistical averages and the trajectories can be made.

In general, as the $d_{eq,inj}$ increased, it appears as though the stable region also increases. A portion of the lengthening can be attributed to the increasing formation stage. As previously discussed in section 4.3, the H_F increases when $d_{eq,inj}$ increases, likely due to the bubble prematurely detaching from the nozzle while gas continues to be injected. The bubble will continue to grow in d_{eq} as the bubble rises in the column. Even for trials where this behavior is observed, a plateau in the statistical average d_{eq} is often visible, suggesting a stable stage occurs.

The angles of the trajectories along the lower and upper horizontal axis were found for all levels of background fluidization, seen in tables 4.17-4.19. The angles provide insight into the unstable region, with increased angles suggesting more variance. In general, the angles decreased as the $d_{eq,inj}$ increased. In some instances, the angle was lower than expected, likely due to the method of measuring the angles, which tended to cut off portions of the trajectories.

The development of a stable and unstable region may be due to the emulsion phase motion, discussed in section 2.1.3. As the bubble is formed, the injection of the gas through the nozzle is the primary factor on the bubble. After the injection is complete, the bubbles seem to maintain size, then change. This change may be attributed to the levels of background fluidization, and thus, the emulsion phase motion. The motion of the emulsion phase may push the bubble and cause these changes, like decreasing size and motion path.

At 1.1Umf, increased stochastic behavior is observed. Increasing the fluidization level will lead to increased frequency of background bubbles, which will breakup and coalescence with the injected bubble. The stable region was not observable in the individual bubbles for 1.1Umf. There were no apparent trends as the t_{inj} changed for this level of background fluidization.

$d_{eq,inj}$ (cm):	2.9	3.6	4.0	4.3	5.0	6.5
0.7Umf	0.16	0.20	0.23	0.20	0.43	0.45
Umf	0.20	0.18	0.20	0.23	0.32	0.32

Table 4.16: Visually approximate H_S for system 1 at various U and $d_{eq,inj}$

$d_{eq,inj}$ (cm)	2.9	3.6	4.0	4.3	5.0	6.5
Lower x-axis angle (°)	27.2	8.4	14.0	6.7	4.1	1.4
Upper x-axis angle (°)	14.7	5.4	10.1	9.5	9.8	4.4

Table 4.17: Approximate angle in degrees of unstable region with relation to center line at 0.7Umf

$d_{eq,inj}$ (cm)	2.9	3.6	4.0	4.3	5.0	6.5
Lower x-axis angle (°)	4.6	6.3	11.6	13.3	6.3	9.7
Upper x-axis angle (°)	5.5	6.4	7.1	12.5	8.9	3.3

Table 4.18: Approximate angle in degrees in degrees in degrees of unstable region with relation to center line at Umf

$d_{eq,inj}$ (cm)	2.9	3.6	4.0	4.3	5.0	6.5
Lower x-axis angle (°)	12.7	6.5	9.1	9.7	7.0	7.0
Upper x-axis angle (°)	12.5	12.7	13.3	12.0	10.0	19.1

Table 4.19: Approximate angle in degrees in degrees of unstable region with relation to center line at 1.1Umf

	$d_{eq,inj}$: 2.9 cm	$d_{eq,inj}$: 3.6 cm	$d_{eq,inj}$: 4.0 cm	$d_{eq,inj}$: 4.3 cm	$d_{eq,inj}$: 5.0 cm	$d_{eq,inj}$: 6.5 cm
0.7 Umf	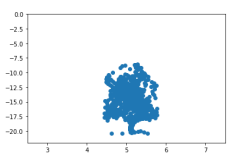	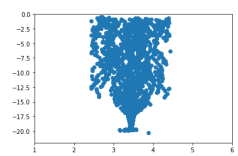	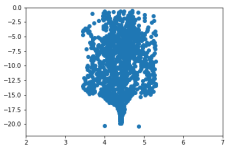	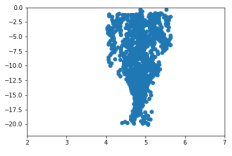	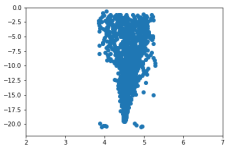	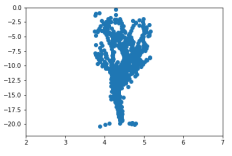
Umf	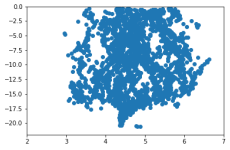	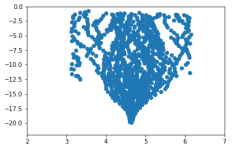	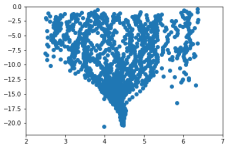	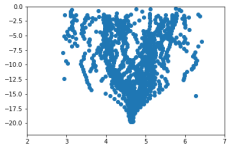	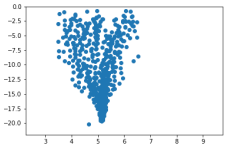	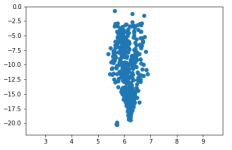
1.1 Umf	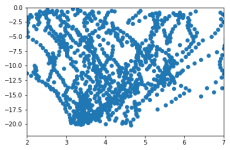	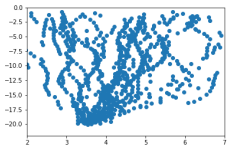	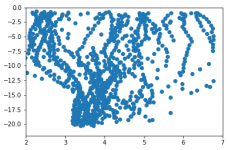	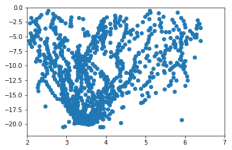	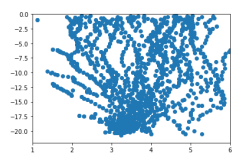	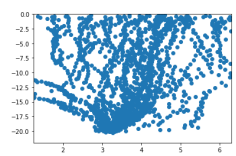

Table 4.20: Trajectory of bubble motion based on the center of mass in the x- and y-axes
System 1

D_{bed}: 15 cm, d_p: 0.2 mm, Q: 17 m/s [System 2]

The center of mass of 30 bubbles are shown in table 4.25. The H_S can be seen in table 4.21.

Systems 1 and 2 can be compared according to 4.1. The bubbles at 0.7Umf and a $d_{eq,inj}$ of 2.3 cm dissipated quickly and is difficult to analyze based on the trajectory. These systems are observed to have a similar length in the stable region and a similar natural variance in the unstable region. When inspecting the visual differences in H_S of systems 1 and 2, H_S appears longer for system 1 at a higher $d_{eq,inj}$ than system 2. When calculated, the length of the normalized height of the stable region is similar for both systems for the same $d_{eq,inj}$. The similarities in the stable region suggest that after the formation of the bubble, the dynamics are not especially affected by the formation, so bubbles of similar size in similar systems will behave similarly during the rising stage even if the formation of the bubble is different.

The variance along the horizontal axis within the unstable region is also similar for both systems, which suggests that the unstable region is generally unaffected by the changes in the injection velocity. The angle of the lower and upper x-axis can be found in tables 4.22-4.24. In general, the angles of the trajectory for system 2 also decrease at increasing $d_{eq,inj}$, suggesting a decreasing variance. When compared to the angles in system 1 for like Us and $d_{eq,inj}$, the angle are fairly similar. The similarity in angles despite differences in injection velocity suggests that changing injection velocity will not have a large effect on the unstable stage. This supports the belief that the formation stage is mostly affected by the differing injection velocities, while the rising stage is affected to a lesser extent.

$d_{eq,inj}$ (cm):	2.3	3.2	4.0	5.1
0.7Umf		0.18	0.18	0.23
Umf	0.18	0.18	0.20	0.27

Table 4.21: Visually approximate H_S for system 2 at various U and $d_{eq,inj}$

$d_{eq,inj}$ (cm)	2.3	3.2	4.0	5.1
Lower x-axis angle (°)		15.6	10.6	3.7
Upper x-axis angle (°)		6.4	6.5	6.3

Table 4.22: Approximate angle in degrees in degrees of unstable region with relation to center line at 0.7Umf

$d_{eq,inj}$ (cm)	2.3	3.2	4.0	5.1
Lower x-axis angle (°)	8.0	4.7	11.0	2.2
Upper x-axis angle (°)	5.4	5.3	10.6	6.3

Table 4.23: Approximate angle in degrees in degrees of unstable region with relation to center line at Umf

$d_{eq,inj}$ (cm)	2.3	3.2	4.0	5.1
Lower x-axis angle (°)	8.5	20.4	8.8	20.4
Upper x-axis angle (°)	28.8	14.8	15.9	10.2

Table 4.24: Approximate angle in degrees in degrees of unstable region with relation to center line at 1.1Umf

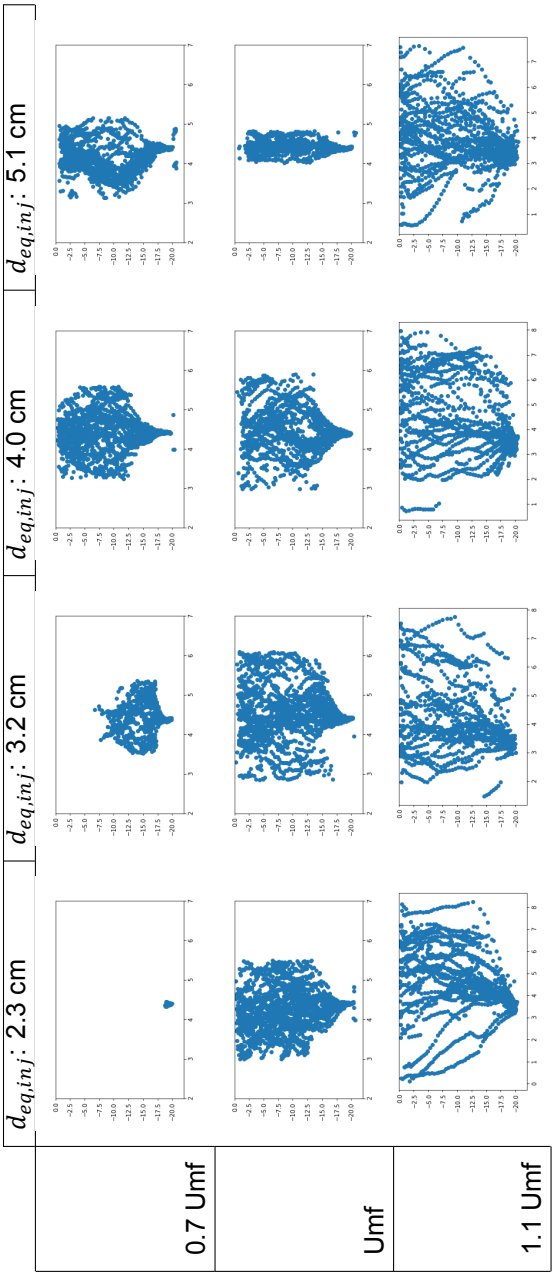

Table 4.25: Trajectory of bubble motion based on the center of mass in the x- and y-axes
System 2

D_{bed}: 15 cm, d_p: 0.5 mm, Q: 35 m/s [System 3]

The trajectory of the center of mass of the bubbles for system 3 are shown in table 4.29. The visually estimated H_S of system 3 can be seen in table 4.26. The data at Umf and a $d_{eq,inj}$ of 4.3 cm is excluded, as the bubbles exhibited behavior that was not observed with other like systems and was assumed to be experimental error. For systems utilizing the smaller particles, the H_S at 1.1Umf was too short to assess. However, the H_S for system 3 at 1.1Umf is longer at certain $d_{eq,inj}$ because background bubbles were less frequent in system 3 due to the difference in particles.

At a $d_{eq,inj}$ of 2.9 cm for both levels of background fluidization, the bubbles are unable to consistently exit the frame. At Umf, the bubbles dissipated before exiting the frame. At 1.1Umf, fewer bubbles compared to increased $d_{eq,inj}$ were able to exit the frame. The bubbles that were able to exit the frame typically did so after coalescing with the background bubbles. Therefore, the $d_{eq,inj}$ was determined to be insufficient to effectively form stable bubbles.

This system can be compared to system 1, differing in particles. The H_S at Umf is similar for all $d_{eq,inj}$ in both systems. When calculated, the length of the normalized height of the stable region at Umf is similar for systems 1 and 3, suggesting these different particles may have a strong effect on the stable region.

In general, the natural variances along the horizontal axis were more pronounced for system 1 compared to system 3, which comparing the difference in angles of the unstable region in tables 4.27 and 4.28. The stable regions for the different particles appear to be similar, and the unstable region seems to be more affected by the different particle sizes. At Umf, the decreasing apparent natural variance along the horizontal axis is likely due to the difference in breakup of particles. As previously discussed, bubble breakup is an important factor for Geldart A particles but negligible for Geldart B particles [23]. The particles in system 1 are classified as Geldart A/B, and the particles of system 3 are Geldart B. System 3 may be less inclined to exhibit bubble breakage, so less natural variance is expected. The angles of the trajectories are smaller for system 3 than system 1, suggesting less variance along the x-axis. Additionally, the motion of the emulsion phase for the particles utilized in system 3 may differ from the particles in system 1. The motion of the emulsion phase for the 0.5 mm particles may carry the bubbles further from the injection point and cause a larger variance along the x-axis.

At 1.1Umf, background bubbles were more frequent for system 1 than system 3, leading to an increased variance along the x-axis, which was observed in these experiments and in the angles of the trajectories.

$d_{eq,inj}$ (cm):	2.9	3.6	4.0	4.3	5.0	6.5
Umf	0.14	0.14	0.20		0.27	0.23
1.1Umf		0.14		0.14		0.16

Table 4.26: Visually approximated normalized H_S for system 3 at various U and $d_{eq,inj}$

$d_{eq,inj}$ (cm)	2.9	3.6	4.0	4.3	5.0	6.5
Lower x-axis angle (°)	24.2	9.2	2.6		2.1	14.2
Upper x-axis angle (°)	17.7	9.2	3.9		3.1	5.9

Table 4.27: Approximate angle in degrees in degrees of unstable region with relation to center line at Umf

$d_{eq,inj}$ (cm)	2.9	3.6	4.0	4.3	5.0	6.5
Lower x-axis angle (°)	7.6	5.0	8.5	2.5	13.0	11.3
Upper x-axis angle (°)	8.5	7.8	7.3	8.4	10.2	15.1

Table 4.28: Approximate angle in degrees in degrees of unstable region with relation to center line at 1.1Umf

	$d_{eq,inj}$: 2.9 cm	$d_{eq,inj}$: 3.6 cm	$d_{eq,inj}$: 4.0 cm	$d_{eq,inj}$: 4.3 cm	$d_{eq,inj}$: 5.0 cm	$d_{eq,inj}$: 6.5 cm
Umf	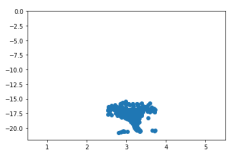	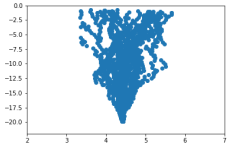	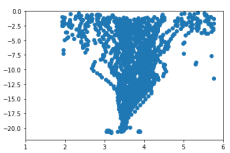	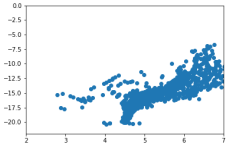	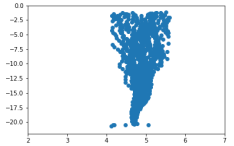	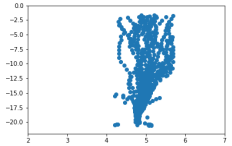
1.1 Umf	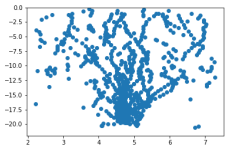	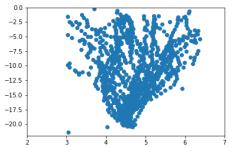	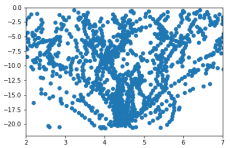	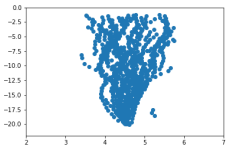	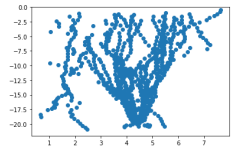	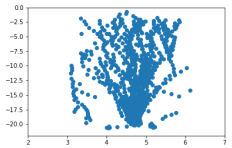

Table 4.29: Trajectory of bubble motion based on the center of mass in the x- and y-axes
System 3

D_{bed}: 5 cm, d_p: 0.2 mm, Q: 26 m/s [System 4]

The trajectory of the center of mass of the bubbles can be seen in table 4.31. The visually estimated H_S based on the trajectory can be seen in table 4.30. Large differences are expected between the statistical analysis and the trajectory based H_S. The statistical analysis of the rising stage is believed to be inaccurate due to slugging effects. Wall effects and slugs are major factors for system 4. When $d_{eq,inj} \geq 3.7$ cm, the bubble is defined as a slug, which accounts for the majority of the experiments in system 4.

Systems 1, 2, and 4 can be compared based on $d_{eq,inj}$. Overall, the H_S of system 4 is less than than system 1 and 2. The slugging in system 4 is difficult to compare in terms of variance in the horizontal axis. The H_S of system 4 is lower than the other comparable systems likely due to slugging. The slug appeared to remain in the same place above the nozzle as gas is injected. The height of the slug increased slowly, as the injected gas must fill the entire diameter of the column for the center of mass to increase. The slug would not move until the particles began to rain down.

For all levels of background fluidization when $d_{eq,inj}$ was 2.7 cm, dissipation occurred before the bubble could exit the frame. The end of the stable region is still visible. Within the projections, the sudden shift of the center of mass towards the column wall is likely due to slugging. As discussed previously, the slug would take up the entirety of the column, the particles would ”rain” down into the bubble, then the bubble would split it, often unevenly. The uneven split causes the center of mass to shift to either side of the wall. The slugs would coalesce shortly after, so the trajectory appears to become approximately rectilinear again due to coalescence. The effect of the emulsion phase motion may be present, but slugging appears to have a larger effect on the bubble motion and regions.

$d_{eq,inj}$ (cm):	2.7	3.7	4.7	5.9
0.7Umf	0.09	0.09	0.18	0.20
Umf	0.14	0.16	0.16	0.20
1.1Umf	0.09	0.09		0.23

Table 4.30: Visually approximate normalized H_S for system 4 at various U and $d_{eq,inj}$

Table 4.31: Trajectory of bubble motion based on the center of mass in the x- and y-axes
System 4

4.5. Velocity and Dynamics Analysis

The motion and development of the bubble over the column is believed to be able to expressed in terms of correlations and equations. In section 2.2, various methods of analyzing bubbles were described, and the following section investigates these correlations.

4.5.1. D_{eq} Correlations

The Kato-Wen and Werther correlations were selected for comparison to the experiments. The corresponding equations can be seen in section 2.2.3.

The figures of the Kato-Wen and Werther correlations can be found in Appendix C.1. A selection are provided in Figure 4.18. The heights used in these correlations corresponded to the normalized heights of the projection frame at 0.3, 0.6, and 0.8.

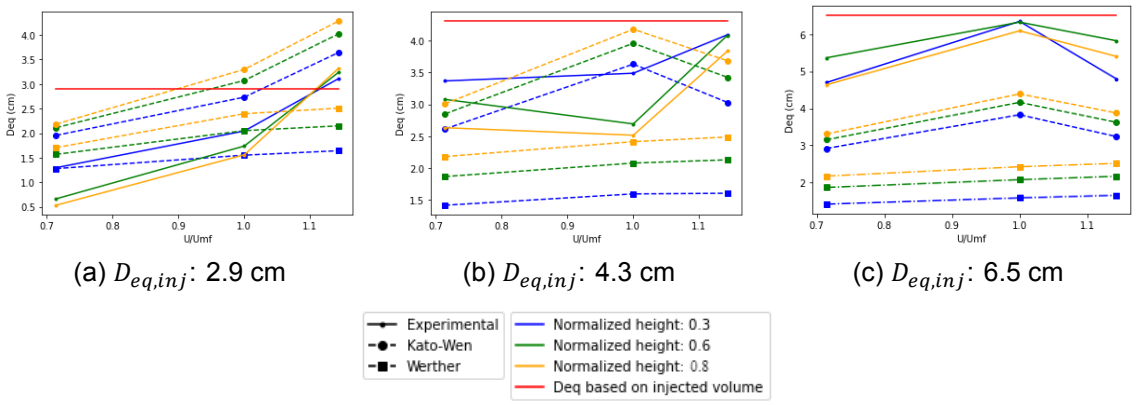

(a) $D_{eq,inj}$: 2.9 cm (b) $D_{eq,inj}$: 4.3 cm (c) $D_{eq,inj}$: 6.5 cm

Figure 4.18: Comparison of the experimental and Kato-Wen and Werther correlations at three normalized heights in the column D_{bed}: 15 cm, d_p:0.2mm, Q: 35 m/s [System 1]
Additional figures provided in Figure C.1

The study by Riechmann found the correlations regarding d_{eq} and U/Umf tended to decrease in accuracy as Umf and the height of the bubble in the column increased [5]. Similar behavior was observed in these experiments. The wall effects are expected to be present at $d_{eq} \geq 0.1D$, which is above the minimum injected d_{eq}. The wall effects appeared to have a greater effect on larger $d_{eq,inj}$, as the correlations became increasingly dissimilar.

Few consistencies were found between the selected correlations and systems 1 and 2. System 3 appeared to be relatively more similar to the correlations, even at larger $d_{eq,inj}$. System 4 experienced slugging, which had a greater effect on the experimental d_{eq} and caused a greater deviation between the correlations and experiments.

In general, these correlations were not specifically designed for the use when the level of background fluidization is less than or equal to Umf and for injected bubbles. For the systems where D_{bed} is 15 cm, the smaller $d_{eq,inj}$ was better represented by the Werther correlation. As the $d_{eq,inj}$ increased, the Kato-Wen correlation represented the bubbles more accurately, especially for the bubble at lower normalized heights. The larger $d_{eq,inj}$ varied drastically from both correlations. These correlations were designed for naturally forming bubbles, while the bubbles within this research were injected.

4.5.2. Bubble Rise Velocity

The bubble rise velocity of the bubbles was analyzed with two methods: discrete and derivation of a B-spline. The discrete calculation can be seen in equation 2.5. The B-spline bubble rise velocity was calculated based on the derivation of a 3rd order B-spline fit through the center of masses of the individually plotted bubbles and was then averaged. For this analysis, two bubbles were selected: a bubble that obtained the largest d_{eq} and a bubble that obtained the d_{eq} closest to the average while traversing the column. Both the discrete and derived B-spline bubble rise velocity was found for each bubble and compared in Figure 4.19. The percent difference between the discrete and derived B-spline bubble rise velocity can be seen in table 4.32. Both methods of finding the bubble rise velocity appear to have similar noise and either may be suitable for future calculations.

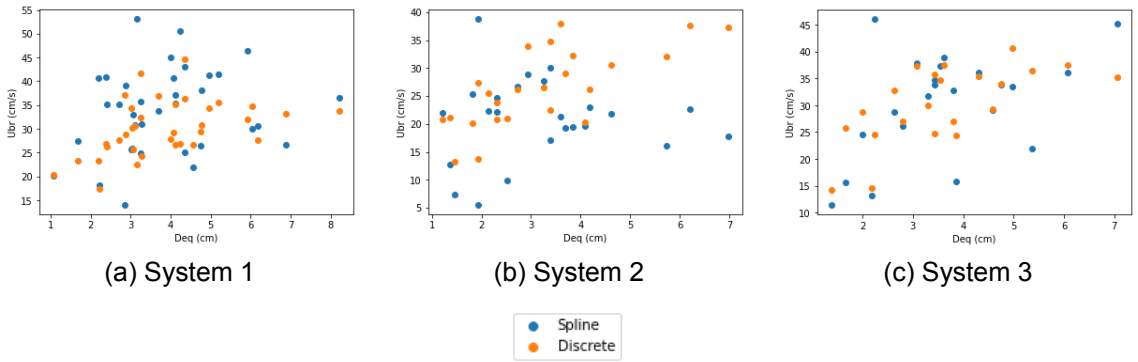

(a) System 1 (b) System 2 (c) System 3

Figure 4.19: Comparison of the Discrete and B-Spline derived velocities for all systems

	System 1	System 2	System 3
% Difference	27.8	23.4	17.9

Table 4.32: Percent difference of bubble rise velocity obtained from the discrete and derived B-spline methods in at 15 cm column

4.5.3. Froude number of the Column

The excess velocity-based Froude number (Fr_{column}), described in section 2.1.4, is examined for the systems in this research. Figure 4.20 is the representation of the Fr_{column}.

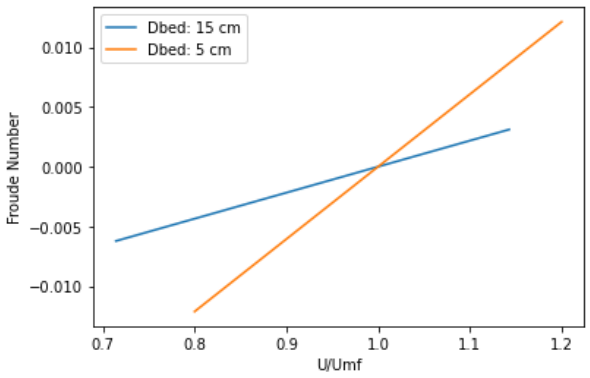

Figure 4.20: Fr_{column} based on D_{bed}

The Fr_{column} was designed to model CFD-DEM simulations of mixing times within a column. The Fr_{column} could also describe the nature within the entirety of the column and was able to describe the general bubbling within the beds in this research when level of background fluidization is greater than or equal to Umf. However, the Fr_{column} is not designed to describe the individual bubbles. The development of a more relevant framework of describing the Froude number based on the level of background fluidization, injection velocity, and particle was necessary for this research.

4.5.4. Davidson and Harrison

The relationship between the Davidson and Harrison correlation and the bubble rise velocity from this research can be found in Figures 4.21 and 4.22.

The experimental data and the Davidson and Harrison correlation do not align closely. The Davidson and Harrison correlation is able to have an initial approach of the bubble rise velocity but is unable to accurately model the experimental results. The experimental results are typically less than the Davidson and Harrison correlation, do not follow a similar curve, and appear to be approximately linear. The comparison of these results and the ones from Riechmann showed a similar bubble rise velocity for bubbles of similar d_{eq} and level of background fluidization. The results from Riechmann also appear to be somewhat linear with natural variation along the bubble rise velocity. Riechmann also found the

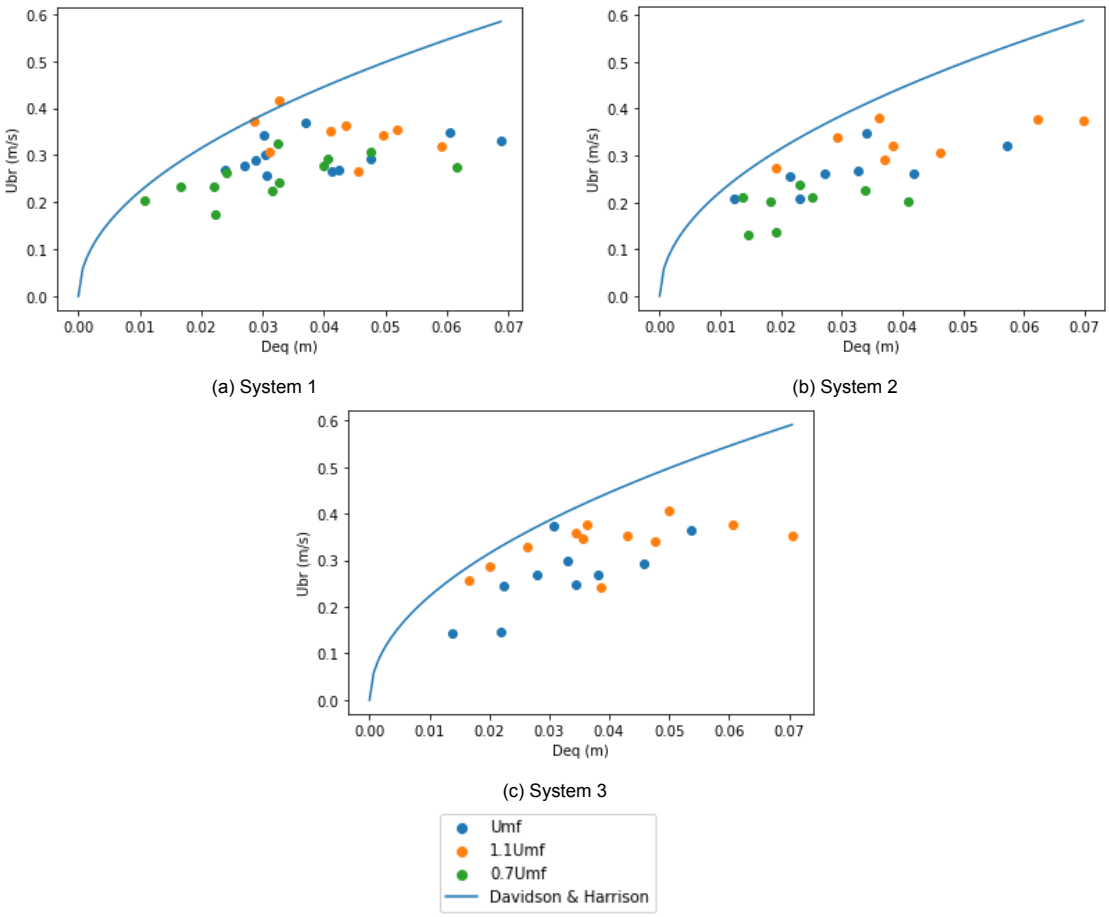

(a) System 1

(b) System 2

(c) System 3

Figure 4.21: Comparison of bubble rise velocity to Davidson and Harrison correlation in 15 cm column

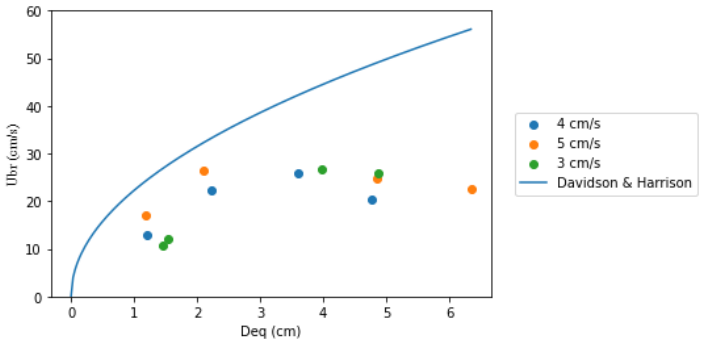

Figure 4.22: Comparison of bubble rise velocity to Davidson and Harrison correlation in 5 cm column System 4

Davidson and Harrison correlation to inadequately describe the experimental bubble rise velocity [5]. The Davidson and Harrison correlation does not account for a variety of factors that affect bubbles, taking the Froude number as a single value. This research further investigates other approaches to the Froude number for increased accuracy.

4.5.5. Froude Number

To understand the relationship of the gas-solid bubbles to the analogy of the gas-liquid bubbles, the shape and bubble rise velocity should be described. Within the ellipsoidal regime of a gas-liquid bubble, the bubble rise velocity is approximately constant. An analysis of the shape and bubble rise velocity of

the gas-solid bubbles is conducted.

An ellipsoidal bubble, or bluff body, is defined as when the width of the bubble (W) is greater than the height (L). The average aspect ratio of bubbles over the normalized height of the projection frame can be seen in Appendix C.5. The overall trend reveals the bubbles can be generally considered bluff bodies. The points at which the length is greater than the width of the bubble are when $d_{eq,inj}$ are large or during the bubble formation. The average aspect ratios range from 0.63 to 0.79, while similar studies found an average aspect ratio of 0.62 [5].

The bubble should also be a bluff body at the various levels of background fluidization for differing bubble rise velocities. For each experiment, two bubbles were analyzed: one with the largest measured d_{eq} and the other with a measured d_{eq} closest to the average. The aspect ratio and bubble rise velocity were found for each bubble and can be seen in Appendix C.6. The bubbles below Umf had a tendency to be elongated (L > W), and some bubbles may not be described as bluff bodies. However, the majority of the bubbles can be considered bluff bodies, even at differing bubble rise velocities.

The bubble rise velocity should be approximately constant, even as the d_{eq} changes. Riechmann found that even as d_{eq} increased, the bubble rise velocity remained approximately constant [5]. From these experiments, this relationship can be seen in Figure 4.23. These figures show the bubble rise velocity is approximately constant for the variety of d_{eq} at varying levels of background fluidization.

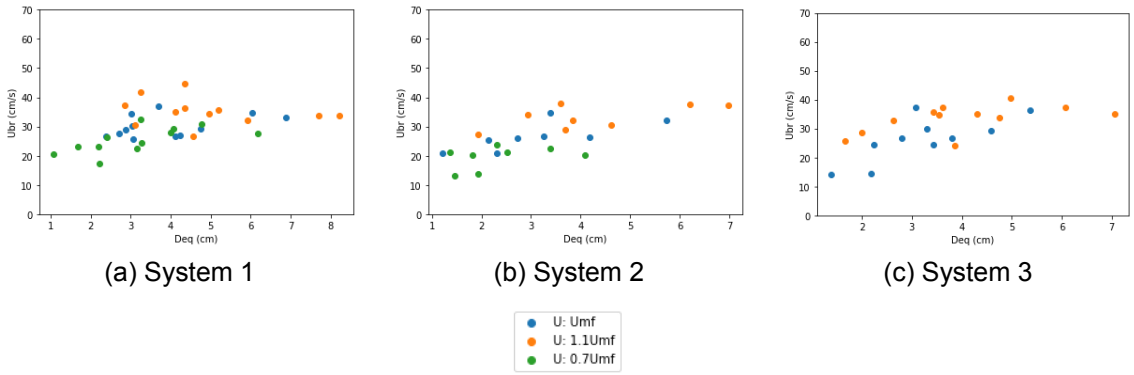

(a) System 1 (b) System 2 (c) System 3

Figure 4.23: U_{br} by D_{eq}

Therefore, it can be assumed that the bubbles will form ellipsoidal bluff bodies in these systems and be able to maintain an approximately constant bubble rise velocity as d_{eq} varies.

The relationships of the Froude number are discussed in detail in section 2.2.5. The perpendicular drag coefficient and spherical volume based drag coefficient can be calculated for each system and levels of background fluidization. The $\frac{V}{A_\perp}$ or d_{eq} and ρU^2 were plotted, seen in Figure 4.24. The line of best fit was calculated, and the slope was taken as the relationship to the drag coefficient. The $C_{D\perp}$ and C_{DV} were measured through this method. The resulting drag coefficients can be found in table 4.33. The slope of the drag coefficient for system 1 at 1.1Umf was negative or nearly negative, likely due to bubble coalescence.

	System 1		System 2		System 3	
	$C_{D\perp}$	C_{DV}	$C_{D\perp}$	C_{DV}	$C_{D\perp}$	C_{DV}
1.1Umf	0.144	-1.67	2.58	5.15	1.22	3.74
Umf	0.738	3.20	1.04	4.53	0.701	2.77
0.7Umf	2.07	5.26	1.05	3.53		

Table 4.33: $C_{D\perp}$ and C_{DV} based on levels of background fluidization and system

The Froude number was calculated by taking the different drag coefficients as constants and utilizing equation 2.6. The Froude number from the perpendicular drag coefficient ($Fr_\perp$), the spherical volume based drag coefficient (Fr_v), and the percent difference between the Froude numbers can be seen in table 4.34. The Froude number based on the perpendicular drag coefficient is related to a non spherical bubble, while the Froude number based on the volume is related to a spherical bubble. The bubbles

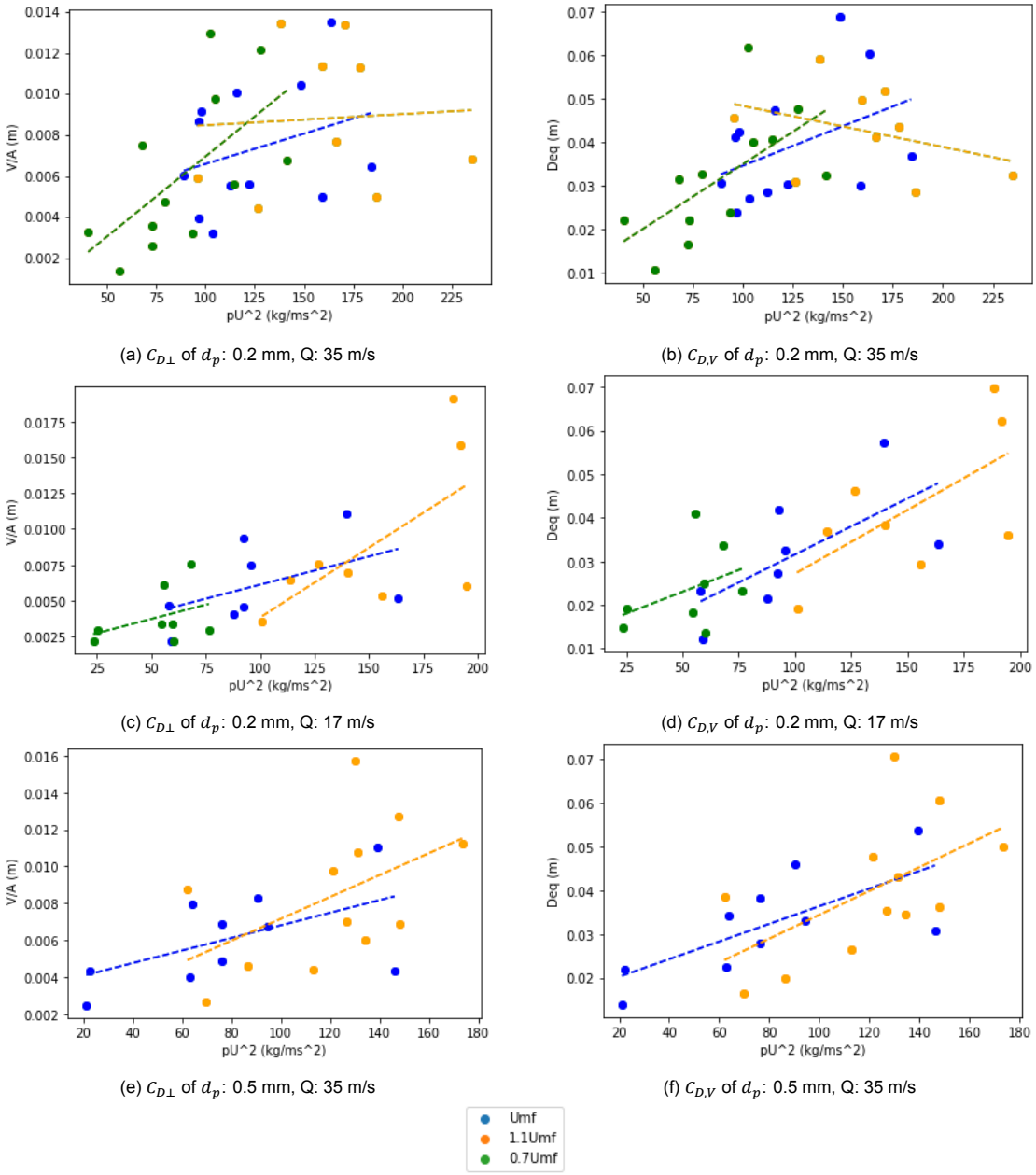

(a) $C_{D\perp}$ of d_p: 0.2 mm, Q: 35 m/s

(b) $C_{D,V}$ of d_p: 0.2 mm, Q: 35 m/s

(c) $C_{D\perp}$ of d_p: 0.2 mm, Q: 17 m/s

(d) $C_{D,V}$ of d_p: 0.2 mm, Q: 17 m/s

(e) $C_{D\perp}$ of d_p: 0.5 mm, Q: 35 m/s

(f) $C_{D,V}$ of d_p: 0.5 mm, Q: 35 m/s

Figure 4.24: Characteristic shape by ρU^2

were observed to have a tendency to form ellipsoids, so the Froude number from perpendicular drag coefficient was further investigated. The Froude number was also calculated for each of the bubbles based on equation 2.7 and is referred to as Fr_{eq}.

The $Fr_{\perp}$, Davidson and Harrison correlation, and the individually calculated Fr_{eq} are compared based on system in Figure 4.25. Additional comparisons seperated by system and level of background fluidization of the $Fr_{\perp}$, Fr_v, individually calculated Fr_{eq}, and the Davidson and Harrison correlation are in Figures C.7-C.9. Based on the individually calculated Fr_{eq}, the Froude number appears to be affected by previously unaccounted variables, like the background fluidization, d_{eq}, and particles. The individually calculated Fr_{eq} are generally not constant and seems to decrease for certain cases.

More data may be necessary to more accurately describe the dynamics of a bubble, as the Froude number in this research appear to be inadequate at describing the individual bubble behavior.

	System 1			System 2			System 3		
	$Fr_{\perp}$	Fr_v	% difference	$Fr_{\perp}$	Fr_v	% difference	$Fr_{\perp}$	Fr_v	% difference
1.1Umf	3.73	1.09	109	0.880	0.623	34	1.28	0.731	55
Umf	1.60	0.791	68	1.39	0.664	70	1.69	0.850	66
0.7Umf	0.983	0.617	46	1.38	0.753	59			

Table 4.34: Froude number calculated based on $C_{D\perp}$, C_{DV}, and the percent difference

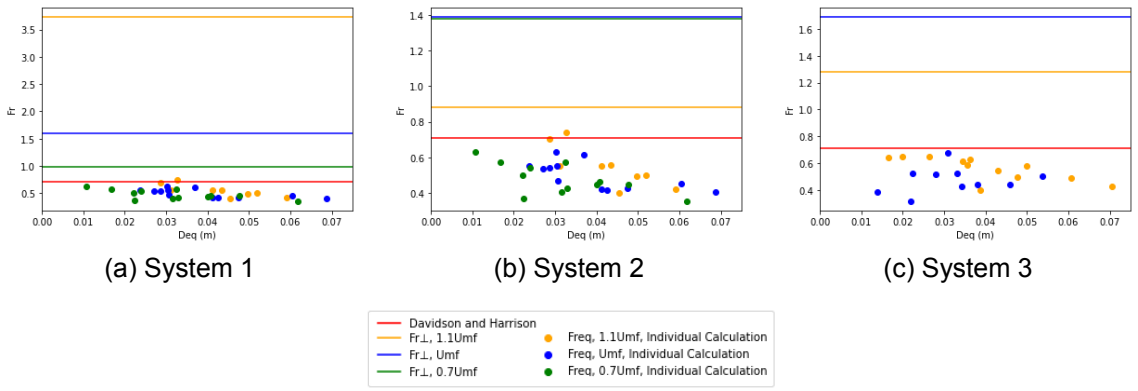

(a) System 1 (b) System 2 (c) System 3

Figure 4.25: Comparison of different Froude numbers based on level of background fluidization

5

Conclusion and Recommendations

5.1. Conclusions

The overall goals of this work were to conduct preliminary explorations of the possibilities and limitations of a 3D time-resolved reconstructions and to study bubble dynamics though analysis of individually injected bubble from 2D projections.

These experiments utilized a setup consisting of three x-ray sources/detectors around a 3D column with a central injection nozzle. The positioning of the x-ray sources/detectors allows for 3D reconstructions to be modeled through scripts developed by A.B.M. Graas. This research used the scripts for preliminary models of the 3D column to lay groundwork for future use. The investigation of the bubble dynamics focused on bubble analysis from 2D projections. The background fluidization, injected volume, injection velocity, particles, and column diameter were varied. The interactions of these factors allowed for insight into a complex system. Relevant correlations were examined.

The setup of the column within this experiment allowed for the observation of an injected bubble in the approximate center of a column. In general, the bubble would travel towards the surface of the bed and develop into an ellipsoid. While the size of the bubble was dependent on a variety of factors, broadly, the bubbles would shrink below minimum fluidization, maintain size at minimum fluidization, and grow due to coalescence above minimum fluidization. The frame of the x-ray sources/detectors focused on the injection nozzle such that the study of the formation and rising stages were possible. The formation stage consisted of the injection and initial growth of the bubble. The rising stage occurred when the bubble no longer increased in size from the injection and began to traverse the column. Within the rising stage, two regions were observed: the ”stable” and ”unstable” regions. The stable region occurred directly after the formation stage and was observed when the trajectory of the bubble had little motion along the horizontal axis of the column. The unstable region occurred after the stable region and was observed when the trajectory of the bubble sharply increased in variance along the horizontal axis of the column. These regions within the rising stage were believed to be influenced by the bubble cloud and emulsion phase motion. The bubble cloud was believed to be influenced by the injection volume and level of background fluidization, which in turn, influenced the interactions with the emulsion phase.

The dynamics of the bubbles were initially understood through a simple analogy to gas-liquid bubbles. Through this analogy, the gas-solid bubbles are expected to have a constant Froude number when the drag coefficient and the shape of the bubble is constant. Additionally, the bubble cloud is expected to have a significant pressure difference over a small length, leading to the expectation the cloud is not negligible and should be taken into account. However, this research lacked the capability to properly analyze the bubble clouds. Previous correlations based on the Froude number were insufficient for describing the motion of an individual bubble, often designed to understand the dynamics of the overall column or not accounting for various parameters. This research investigated the use of a Froude number through the direct calculation of the drag coefficient. The resulting Froude numbers suggested the Froude number is not constant and is dependent on parameters that have not previously been taken into account, like the background fluidization level and particles. More data and further analysis are necessary to gain conclusive insight into the effect of various factors on the Froude

number.

This research analyzed three fluidization rates: below, at, and above minimum fluidization. Generally, bubbles below minimum fluidization tended to be smaller and dissipate more readily when compared to bubbles of the same injected volume at minimum fluidization. Bubbles at minimum fluidization tended to maintain volume with relatively little change in size. Bubbles above minimum fluidization were often relatively larger because of the coalescence associated with interaction with background bubbles.

The background fluidization was affected by the different particles. At the same fluidization level, the Geldart A/B particles have more frequent background bubbling compared to the Geldart B particles. The more frequent background bubbles readily coalesce with the injected bubbles, affecting the measured bubble size for similar volumes of injection. The bubble cloud around the bubble may also be affected by the particles, as the cohesion and size of the particles may lead to different particle-particle interactions.

In addition to the background fluidization and particles, this research investigated the effects of altering the volume and velocity of the injected gas. The injection duration could be changed to isolate these variables. By increasing the volume of injected gas for like setups, the spherical equivalent diameter of the bubble increased, the natural variance along the horizontal axis of column decreased, the length of the formation stage of the bubble increased, and the length of the rising stage remained similar. These changes in the formation stage were suspected to be associated with the bubble cloud. The velocity of the injection was also varied. As the velocity of the injected gas increased, the spherical equivalent diameter of the bubble increased for similar injection volumes. The formation stage was mostly affected. Slower injection velocities require a longer injection duration for equivalent injection volumes, thus, allowing for more of the injected gas to leak into the emulsion phase and resulting in smaller bubbles with suspected less compact clouds. Longer injection times were observed to form two distinct bubbles from a single injection, as the particles were pushed and prematurely ”cut off” the injection.

The column diameter was varied between 15 and 5 cm. The 5 cm column was affected by slugging, while the 15 cm was not. The effects of slugging on the column were significant and made comparison between the systems difficult. The bubbles in a 5 cm column were observed to have a formation and rising region, but the ”stable” and ”unstable” regions were affected by the slugging.

Overall, the effects of the background fluidization, injection volume and velocity, particle size, and column diameter suggest an intricate connection of factors affecting bubbles forming and rising within a fluidized bed. These results suggest certain unaccounted parameters should be taken into consideration, especially when investigating correlations. Future studies investigating these parameters are necessary to develop more refined correlations that are able to better describe bubbles within a fluidized bed.

5.2. Recommendations

Throughout this research, a variety of opportunities for further research became evident.

The 3D reconstructions of the experimental data could be further analyzed. Preliminary 3D reconstructions in this research seemed to be able to more accurately discern the bubble cloud, allowing for further studies on the interactions between the bubble, cloud, and emulsion phases. These interactions were suspected to have a significant influence on the dynamics of the bubble.

A natural progression of this study would involve the utilization of the data from this research to analyze current CFD models. The speculated dynamics within this research can be used to refine CFD models, allowing for further incorporation of a fundamental understanding of bubble dynamics and the development of digital twin data sets.

This research was originally intended to develop a detailed study of the formation stage of the bubble. However, because of the cropping of the projection frame, there were typically less than five frames of the formation stage, which is insufficient for an accurate study. Future experiments could crop to a smaller frame focused around the nozzle, increasing the frame rate and allowing for a more in depth study of specifically the bubble formation.

Additions and changes to the experiments within this research could also implemented. The particles in these experiments were of different size and material, making direct comparisons difficult. Particles of the same material and different sizes would be preferred. Certain particles are expected to

have a larger delayed bubbling regime, where the bed is fluidized and minimal background bubbling is present. Using these particles would allow for less frequent bubble interactions with the injected bubbles, which led to difficulties within this research. Additionally, this research focused on three levels of background fluidization. The majority of correlations for fluidized beds are designed for background fluidized levels above the minimum fluidization level, where industrial fluidized beds typically operate. A more developed understanding of the correlations related to the bubbles and the dynamics of a bubble could be understood by further increasing the levels of background fluidization. Additional studies further isolating factors would be beneficial to clarifying certain speculations and assumptions made within this research.

Bibliography

[1] J.A.M. Kuipers, W. Prins, and W.P.M. Van Swaaij. “Theoretical and experimental bubble formation at a single orifice in a two-dimensional gas-fluidized bed”. *Chemical Engineering Science* 46.11 (1991), pp. 2881–2894. ISSN: 0009-2509. DOI: https://doi.org/10.1016/0009-2509(91)85157-S. URL: https://www.sciencedirect.com/science/article/pii/000925099185157S.

[2] Liang-Shih Fan and Chao Zhu. “Dense-Phase Fluidized Beds”. *Principles of Gas-Solid Flows*. Cambridge Series in Chemical Engineering. Cambridge University Press, 1998, pp. 371–420. DOI: 10.1017/CBO9780511530142.010.

[3] J. R. Grace. *Essentials of fluidization technology*. Ed. by J. R. Grace, X. Bi, and N. Ellis. Weinheim, Germany: Wiley-VCH Verlag, Apr. 2020.

[4] S. Oka. “Fluidized bed”. *A-to-Z Guide to Thermodynamics, Heat and Mass Transfer, and Fluids Engineering*. Begellhouse, Feb. 2011. DOI: 10.1615/atoz.f.fluidized_bed. URL: https://doi.org/10.1615/atoz.f.fluidized_bed.

[5] Riechmann, Philipp Fedor. “Cross verified independent measurements of correlated bubble property distributions as part of the scale-up of a catalytic bubbling fluidized bed reactor”. en (2022). DOI: 10.5075/EPFL-THESIS-9873. URL: http://infoscience.epfl.ch/record/298825.

[6] A Lotfabad, S. Movahedirad, and M. Sadeghi. “Bubble Formation on a Single Orifice in a Gas Solid Fluidized Bed Using Digital Image Analysis”. *Iranian Journal of Chemical Engineering* 13 (Jan. 2016).

[7] Kamal Nosrati et al. “Experimental study on the pressure wave attenuation across gas-solid fluidized bed by single bubble injection”. *Powder Technology* 305 (2017), pp. 620–624. ISSN: 0032-5910. DOI: https://doi.org/10.1016/j.powtec.2016.10.051. URL: https://www.sciencedirect.com/science/article/pii/S003259101630732X.

[8] Fatemeh Mostafaei et al. “Investigating the bubble dynamics in fluidized bed by CFD-DEM”. *Powder Technology* 366 (2020), pp. 938–948. ISSN: 0032-5910. DOI: https://doi.org/10.1016/j.powtec.2020.03.011. URL: https://www.sciencedirect.com/science/article/pii/S003259102030200X.

[9] R. Andreux and J. Chaouki. “Behaviors of the bubble, cloud, and emulsion phases in a fluidized bed”. *AIChE Journal* 54.2 (2008), pp. 406–414. DOI: https://doi.org/10.1002/aic.11390. eprint: https://aiche.onlinelibrary.wiley.com/doi/pdf/10.1002/aic.11390. URL: https://aiche.onlinelibrary.wiley.com/doi/abs/10.1002/aic.11390.

[10] S.M. Okhovat-Alavian, J. Behin, and N. Mostoufi. “Investigating bubble dynamics in a semi-cylindrical gas-solid fluidized bed”. *Powder Technology* 370 (2020), pp. 129–136. ISSN: 0032-5910. DOI: https://doi.org/10.1016/j.powtec.2020.05.032. URL: https://www.sciencedirect.com/science/article/pii/S003259102030396X.

[11] P.N. Rowe and B.A. Partridge. “An x-ray study of bubbles in fluidised beds”. *Chemical Engineering Research and Design* 43 (1965), S116–S134. ISSN: 0263-8762. DOI: https://doi.org/10.1016/S0263-8762(97)80009-3. URL: https://www.sciencedirect.com/science/article/pii/S0263876297800093.

[12] J. G. Yates, P. N. Rowe, and D. J. Cheesman. “Gas entry effects in fluidized bed reactors”. *AIChE Journal* 30.6 (1984), pp. 890–894. DOI: https://doi.org/10.1002/aic.690300603. eprint: https://aiche.onlinelibrary.wiley.com/doi/pdf/10.1002/aic.690300603. URL: https://aiche.onlinelibrary.wiley.com/doi/abs/10.1002/aic.690300603.

[13] Simon Maurer et al. “Influence of vertical internals on a bubbling fluidized bed characterized by X-ray tomography”. *International Journal of Multiphase Flow* 75 (2015), pp. 237–249. ISSN: 0301-9322. DOI: https://doi.org/10.1016/j.ijmultiphaseflow.2015.06.001. URL: https://www.sciencedirect.com/science/article/pii/S0301932215001378.

[14] C.M. Boyce et al. “Magnetic resonance imaging of single bubbles injected into incipiently fluidized beds”. *Chemical Engineering Science* 200 (2019), pp. 147–166. ISSN: 0009-2509. DOI: https://doi.org/10.1016/j.ces.2019.01.047. URL: https://www.sciencedirect.com/science/article/pii/S0009250919301411.

[15] N. T. Brauer. “Bubble Dynamics in a Sand Fluidized Bed in the Presence of Biomass Pellets”. PhD thesis. 2020.

[16] Adriaan B.M. Graas et al. “X-ray Tomography for Fully-3D Time-Resolved Reconstruction of Bubbling Fluidized Beds”. Under review. 2023.

[17] R. D. Toomey and H. F. Johnstone. “Gaseous Fluidization of Solid Particles”. *Chem. Eng. Progress* 48.5 (May 1952), pp. 220–226.

[18] D. Kunii and O. Levenspiel. “Bubbling Bed Model. Model for Flow of Gas through a Fluidized Bed”. *Industrial & Engineering Chemistry Fundamentals* 7.3 (1968), pp. 446–452. DOI: 10.1021/i160027a016. eprint: https://doi.org/10.1021/i160027a016. URL: https://doi.org/10.1021/i160027a016.

[19] Andrew Lee and David C. Miller. “A One-Dimensional (1-D) Three-Region Model for a Bubbling Fluidized-Bed Adsorber”. *Industrial & Engineering Chemistry Research* (2012), p. 121219160808001.

[20] A. Anantharaman, R. Cocco, and J.W. Chew. “Evaluation of correlations for minimum fluidization velocity (Umf) in gas-solid fluidization”. *Powder Technology* 323 (2018), pp. 454–485. ISSN: 0032-5910. DOI: https://doi.org/10.1016/j.powtec.2017.10.016. URL: https://www.sciencedirect.com/science/article/pii/S0032591017308008.

[21] D. Kunii and O. Levenspiel. *Fluidization Engineering*. en. Ed. by Howard Brenner. 2nd ed. Oxford, England: Butterworth-Heinemann, Apr. 1991.

[22] D. Gidaspow. *Multiphase flow and fluidization*. en. San Diego, CA: Academic Press, Feb. 1994.

[23] Jeong-Hoo Choi, Jae-Ek Son, and Sang-Done Kim. “Generalized Model for Bubble Size and Frequency in Gas-Fluidized Beds”. *Industrial & Engineering Chemistry Research* 37.6 (May 1998), pp. 2559–2564. DOI: 10.1021/ie970915v. URL: https://doi.org/10.1021/ie970915v.

[24] Xiaoli Zhu et al. “Effects of pressure and particle size on bubble behaviors in a pseudo 2D pressured fluidized bed with Geldart A/B, B and D particles”. *Chemical Engineering Journal* (2023), p. 143904. ISSN: 1385-8947. DOI: https://doi.org/10.1016/j.cej.2023.143904. URL: https://www.sciencedirect.com/science/article/pii/S1385894723026359.

[25] J. Werther and O. Molerus. “The local structure of gas fluidized beds —II. The spatial distribution of bubbles”. *International Journal of Multiphase Flow* 1.1 (1973), pp. 123–138. ISSN: 0301-9322. DOI: https://doi.org/10.1016/0301-9322(73)90008-6. URL: https://www.sciencedirect.com/science/article/pii/0301932273900086.

[26] Wilhelm RH and M Kwauk. “Fluidization of solid particles”. *Chemical Engineering Progress* 44 (1948), pp. 201–218.

[27] Karl-Ernst Wirth. “Fluid mechanics of circulating fluidized beds”. *Chemical Engineering & Technology* 14.1 (1991), pp. 29–38. DOI: https://doi.org/10.1002/ceat.270140105. eprint: https://onlinelibrary.wiley.com/doi/pdf/10.1002/ceat.270140105. URL: https://onlinelibrary.wiley.com/doi/abs/10.1002/ceat.270140105.

[28] Kenya Kuwagi et al. “Validation of Dimensionless Parameters for Distinguishing between Homogeneous and Bubbling Fluidizations”. *Open Journal of Fluid Dynamics* 11 (Jan. 2021), pp. 81–97. DOI: 10.4236/ojfd.2021.112006.

[29] Mohammad-Sadegh Salehi, Maryam Askarishahi, and Stefan Radl. “Quantification of Solid Mixing in Bubbling Fluidized Beds via Two-Fluid Model Simulations”. *Industrial & Engineering Chemistry Research* 59.22 (2020), pp. 10606–10621. DOI: 10.1021/acs.iecr.9b06343. eprint: https://doi.org/10.1021/acs.iecr.9b06343. URL: https://doi.org/10.1021/acs.iecr.9b06343.

[30] Yinuo Yao, Craig S. Criddle, and Oliver B. Fringer. “Competing flow and collision effects in a monodispersed liquid–solid fluidized bed at a moderate Archimedes number”. *Journal of Fluid Mechanics* 927 (2021), A28. DOI: 10.1017/jfm.2021.780.

[31] L.G. Gibilaro and P.N. Rowe. “A model for a segregating gas fluidised bed”. *Chemical Engineering Science* 29.6 (1974), pp. 1403–1412. ISSN: 0009-2509. DOI: https://doi.org/10.1016/0009-2509(74)80164-8. URL: https://www.sciencedirect.com/science/article/pii/0009250974801648.

[32] J.F. Davidson and D. Harrison. *Fluidised Particles*. Cambridge, England: Cambridge University Press, Jan. 1963.

[33] John M. Matsen. “Scale-up of fluidized bed processes: Principle and practice”. *Powder Technology* 88.3 (1996). First International Particle Technology Forum, pp. 237–244. ISSN: 0032-5910. DOI: https://doi.org/10.1016/S0032-5910(96)03126-9. URL: https://www.sciencedirect.com/science/article/pii/S0032591096031269.

[34] R. Clift and J.R. Grace. “The mechanism of bubble break-up in fluidised beds”. *Chemical Engineering Science* 27.12 (1972), pp. 2309–2310. ISSN: 0009-2509. DOI: https://doi.org/10.1016/0009-2509(72)85111-X. URL: https://www.sciencedirect.com/science/article/pii/000925097285111X.

[35] D.H. Sharp. “An overview of Rayleigh-Taylor instability”. *Physica D: Nonlinear Phenomena* 12.1 (1984), pp. 3–18. ISSN: 0167-2789. DOI: https://doi.org/10.1016/0167-2789(84)90510-4. URL: https://www.sciencedirect.com/science/article/pii/0167278984905104.

[36] J. van der Schaaf, J.C. Schouten, and C.M. van den Bleek. “Origin, propagation and attenuation of pressure waves in gas—solid fluidized beds”. *Powder Technology* 95.3 (1998), pp. 220–233. ISSN: 0032-5910. DOI: https://doi.org/10.1016/S0032-5910(97)03341-X. URL: https://www.sciencedirect.com/science/article/pii/S003259109703341X.

[37] Shayan Karimipour and Todd Pugsley. “A critical evaluation of literature correlations for predicting bubble size and velocity in gas–solid fluidized beds”. *Powder Technology* 205.1 (2011), pp. 1–14. ISSN: 0032-5910. DOI: https://doi.org/10.1016/j.powtec.2010.09.016. URL: https://www.sciencedirect.com/science/article/pii/S0032591010004936.

[38] J. WERTHER. “Effect of Gas Distributor on Hydrodynamics of Gas Fluidized Beds”. *German Chem. Eng.* 1 (1978), pp. 166–174.

[39] K. Kato and C.Y. Wen. “Bubble assemblage model for fluidized bed catalytic reactors”. *Chemical Engineering Science* 24.8 (1969), pp. 1351–1369. ISSN: 0009-2509. DOI: https://doi.org/10.1016/0009-2509(69)85055-4. URL: https://www.sciencedirect.com/science/article/pii/0009250969850554.

[40] M. Baur et al. *Correction of beam hardening in X-ray radiograms*. Nov. 2018.

[41] A. I. Mazurov and N. N. Potrakhov. “Effect of Scattered X-Ray Radiation on Imaging Quality and Techniques for Its Suppression□”. *Biomedical Engineering* 48.5 (Jan. 2015), pp. 241–245. DOI: 10.1007/s10527-015-9461-6. URL: https://doi.org/10.1007/s10527-015-9461-6.

[42] B. Nett. *X-ray interactions*. 2016. URL: https://howradiologyworks.com/x-ray-interactions (visited on 05/02/2023).

[43] Gary S. Bust and Cathryn N. Mitchell. “History, current state, and future directions of ionospheric imaging”. *Reviews of Geophysics* 46.1 (Feb. 2008). DOI: 10.1029/2006rg000212. URL: https://doi.org/10.1029/2006rg000212.

[44] William M Haynes, ed. *CRC handbook of chemistry and physics, 92nd edition*. 92nd ed. Boca Raton, FL: CRC Press, Dec. 2011.

[45] R. Clift, J.R. Grace, and M.E. Weber. *Bubbles, Drops, and Particles*. Dover Civil and Mechanical Engineering Series. Dover Publications, 2005. ISBN: 9780486445809. URL: https://books.google.nl/books?id=UUrOmD8niUQC.

[46] Clayton T. Crowe, ed. *Multiphase Flow Handbook*. CRC Press, Sept. 2005. DOI: 10.1201/9781420040470. URL: https://doi.org/10.1201/9781420040470.

Symbols

Abbreviation	Description
A_c	Area of curvature
A_p	Area perpendicular
$C_{D\perp}$	Perpendicular drag coefficient
$C_{D,V}$	Volume based drag coefficient
$C_{DV\propto}$	Volume based drag coefficient based on proportion to $C_{D\perp}$
d_0	Werther variable
$d_{b0,eq}$	Initial equivalent diameter of the bubble
D_{bed}	Diameter of the fluidized bed reactor
ΔP	Difference in pressure
d_{eq}	Equivalent diameter of the bubble
$d_{eq,inj}$	Equivalent spherical diameter based on injected volume of gas
d_p	Diameter of particle
f	Frequency
F_B	Buoyancy force
F_D	Frag force
Fr	Froude number
Fr_{column}	Froude number of a column
Fr_{eq}	equivalent diameter based Froude number
Fr_v	spherical volume based Froude number
$Fr_\perp$	perpendicular area based Froude number
g	Acceleration of gravity
γ	Force per length on the bubble
H	Height of bubble in the column
H_{bed}	height of bed
H_F	Normalized height of the end of the formation stage
H_S	Normalized height of the end of the stable region
L	Length of bubble
μ	Attenuation coefficient
Δp_b	Pressure drop within the bed
$\Delta p_{b,max}$	Peak pressure within the bed
ρ_p	Density of particle
Q	Injection velocity
R_c	Radius of curvature
t_{inj}	Injection duration
U	Background fluidization level
u_{br}	Bubble rise velocity
u_{mb}	Minimum bubbling velocity
u_{mf}	Minimum fluidization velocity
V	Volume
W	Width of bubble
Y_M	Center of mass along y-axis

Abbreviations

CFD-DEM Computation fluid dynamics - Discrete Element Method.

CT Computed tomography.

FPD Flat plane detector.

MRI Magnetic resonance imaging.

P&ID Piping and instrumentation diagram.

PMMA Polymethyl methacrylate.

ROI Region of Interest.

SIRT Simultaneous iterative reconstruction technique.

Appendix A

A.1. Dynamics of a gas-liquid bubble

A comparison to the dynamics within a gas-liquid bubble column is made.

The forces acting on a bubble can be summarized as the buoyant (F_B) and drag (F_D) forces.

$$F_B = \Delta\rho g V \tag{A.1}$$

$$F_D = \frac{1}{2}\rho U^2 A C_D \tag{A.2}$$

where ρ is the density, V is the volume, U is the velocity in this section, A is the area, and C_D is the drag coefficient.

A quasi-steady state of the bubble is assumed, allowing for F_B to equal F_D. So,

$$\Delta\rho g V = \frac{1}{2}\rho U^2 A C_D \tag{A.3}$$

Separating the drag coefficient results in:

$$C_D = 2\frac{\Delta\rho}{\rho}\frac{g}{U^2}\frac{V}{A} = \frac{2}{Fr^2} \tag{A.4}$$

where the Fr is the Froude number.

The Froude number can be calculated based on a relationship to the drag coefficient. The drag coefficient can be calculated depending on the shape of the bubble, like a sphere or ellipsoid.

When the bubble is a sphere, the area (A_V) and volume are taken for a sphere. The corresponding drag force is as follows:

$$F_D = \frac{1}{2}\rho U^2 A_V C_{DV} \tag{A.5}$$

where C_{DV} is the spherical drag coefficient.

The perpendicular area of the bubble ($A_\perp$) can also be taken. The corresponding drag force is as follows:

$$F_D = \frac{1}{2}\rho U^2 A_\perp C_{D\perp} \tag{A.6}$$

where $C_{D\perp}$ is the perpendicular drag coefficient.

The relationship between the perpendicular and spherical area of the bubble ($\frac{A_\perp}{A_V}$) is related to the shape of the bubble, where a sphere is equal to 1.

To better understand the relationship of the drag coefficient and the Froude number, the definition of the Froude number is analyzed.

$$Fr^2 = \frac{\rho}{\Delta\rho}\frac{U^2}{g}\frac{A}{V} \tag{A.7}$$

$$U^2 = \frac{\Delta\rho}{\rho} g \frac{V}{A} Fr^2 \tag{A.8}$$

The perpendicular shape of the bubble is analyzed. Replacing the Froude number with the drag coefficient and multiplying of $\frac{A_V}{A_V}$ allows for:

$$U^2 = \frac{\Delta\rho}{\rho} g \frac{V}{A_\perp} \frac{A_V}{A_V} \frac{2}{C_{D\perp}} \tag{A.9}$$

The relationship in a sphere of $\frac{V}{A_V}$ is $\frac{2}{3} d_{eq}$, so

$$\frac{\rho}{\Delta\rho} \frac{U^2}{g} \frac{1}{d_{eq}} = \frac{4}{3} \frac{1}{C_{D\perp}} \frac{A_V}{A_\perp} = Fr_{eq}^2 \tag{A.10}$$

where Fr_{eq} is the Froude number based on the equivalent diameter of the bubble.

Therefore, if $C_{D\perp} \frac{A_\perp}{A_V}$ a constant, then the Froude number will also be a constant. In general, $C_{D\perp}$ is a function of the equivalent diameter Reynolds number ($Re_{eq} = \frac{U d_{eq}}{\nu}$) and the shape, allowing for an interdependence on shape, flow, and interfacial rheology to be present in gas-liquid bubbles.

For bubbles of a fixed shape and simple, fixed interfacial rheology, the perpendicular drag coefficient is essentially a function only of the equivalent diameter Reynolds number. For bluff body bubbles that have a high Reynolds number, the drag coefficient is dominated by interial forces. If the bluff body bubbles that have a high Reynolds number are fixed shapes, the perpendicular drag coefficient is approximately constant, as it is a function of only the shape. Then, the Froude number will be approximately constant and the velocity will be proportional to the square root of the equivalent diameter ($U \propto \sqrt{d_{eq}}$).

The shape of gas-liquid bubbles form in different regimes, which can be seen in Figure A.1.

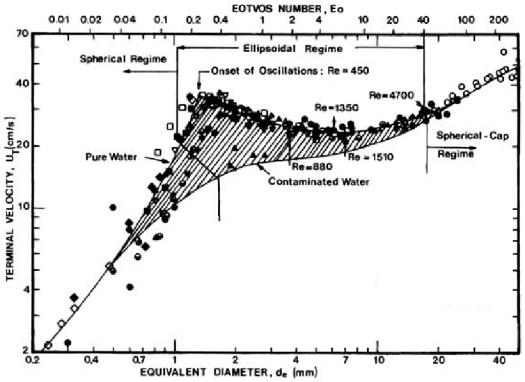

Figure A.1: Terminal velocity of air bubbles in differing levels of contaminated water at 20 °C [45]

Within the spherical regime, the shape is approximately constant, the perpendicular drag coefficient is not approximately constant, and there is a dependence on the equivalent diameter Reynolds number. The Froude number is not approximately constant for this region.

Within the ellipsoidal regime, the shape is not constant. A dynamic interplay between the shape, flow, and interfacial rheology is present and will determine the rise velocity and dynamics of the bubbles.

Within the spherical cap regime, bubbles are approximately constant bluff bodies and have a high equivalent diameter Reynolds number. The Froude number is assumed to be constant for this regime.

A variety of different mechanistic models can be constructed. For example, a simple model, seen in Figure A.2, can be constructed for a gas-liquid bubble such that there is a bluff body that is not a constant shape, has a constant perpendicular drag coefficient, and has a separated flow in the back. Additionally, this simple model can assume a simple interfacial rheology, where the shape of the bubble is determined by the static surface tension (γ) and the normal shear difference across the interface.

The drag force for this bubble is:

$$F_D \sim (P_O - P_B) A_\perp \sim (P_O - P_L) A_\perp \sim \frac{1}{2} \rho U^2 A_\perp C_{D\perp} \tag{A.11}$$

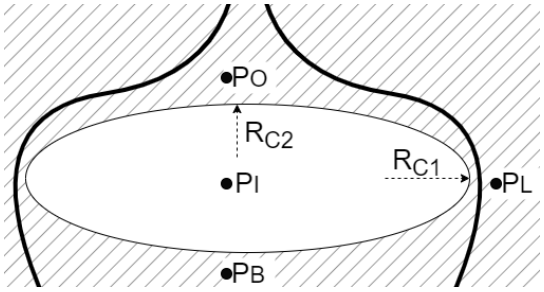

Figure A.2: Simplified diagram of the example gas-liquid bluff body bubble
R_C: Radius of curvature; P_O: stagnant pressure; P_L: lateral pressure; P_I: internal pressure; P_B: back pressure

Through division of the length, the relationship of the force to the radius of the curvature can be found:

$$R_{C\perp} \sim \frac{\gamma}{(P_O - P_L)} \sim \frac{\gamma}{\rho U^2} \tag{A.12}$$

$$\frac{V}{A_\perp} \tilde{\propto} R_{C\perp} \tilde{\propto} \frac{\gamma}{\rho U^2} \tag{A.13}$$

Multiplying both sides by $\frac{A_V}{A_V}$ results in:

$$\frac{A_V}{A_\perp} \tilde{\propto} \frac{\gamma}{\rho U^2} \frac{1}{d_{eq}} \tilde{\propto} Fr_{eq}^2 \tag{A.14}$$

By replacing Fr_{eq}^2, the relationship to the velocity is obtained.

$$U \approx constant\left(\frac{\gamma \Delta \rho g}{\rho^2}\right)^{\frac{1}{4}} \tag{A.15}$$

From literature, the constant is suggested to be approximately 1.5 [46]. This predicts a constant velocity in the ellipsoidal regime regardless of the bubble size, which is a reasonable first order approximation. The focus of this simple model is to illustrate the interplay of the shape, flow, and interfacial rheology, which are a vital in determination of the bubble rise velocity and dynamics.

B

Appendix B

B.1. Individual Bubble Paths

The total vertical height of the frame is approximately 22 cm. The total horizontal width of the frame is approximately 5 cm. The projections are sequential.

For the processed bubble projection, at certain $d_{eq,inj}$, the secondary bubble that formed from the premature cut off of the injected bubble is visible. In these cases, the B-spline and simplified bubble outlines appear to overlap due to the secondary bubble.

B.1.1. D_{bed} : 15 cm, d_p: 0.2 mm, Q: 35 m/s [System 1]

Single Bubble Projection

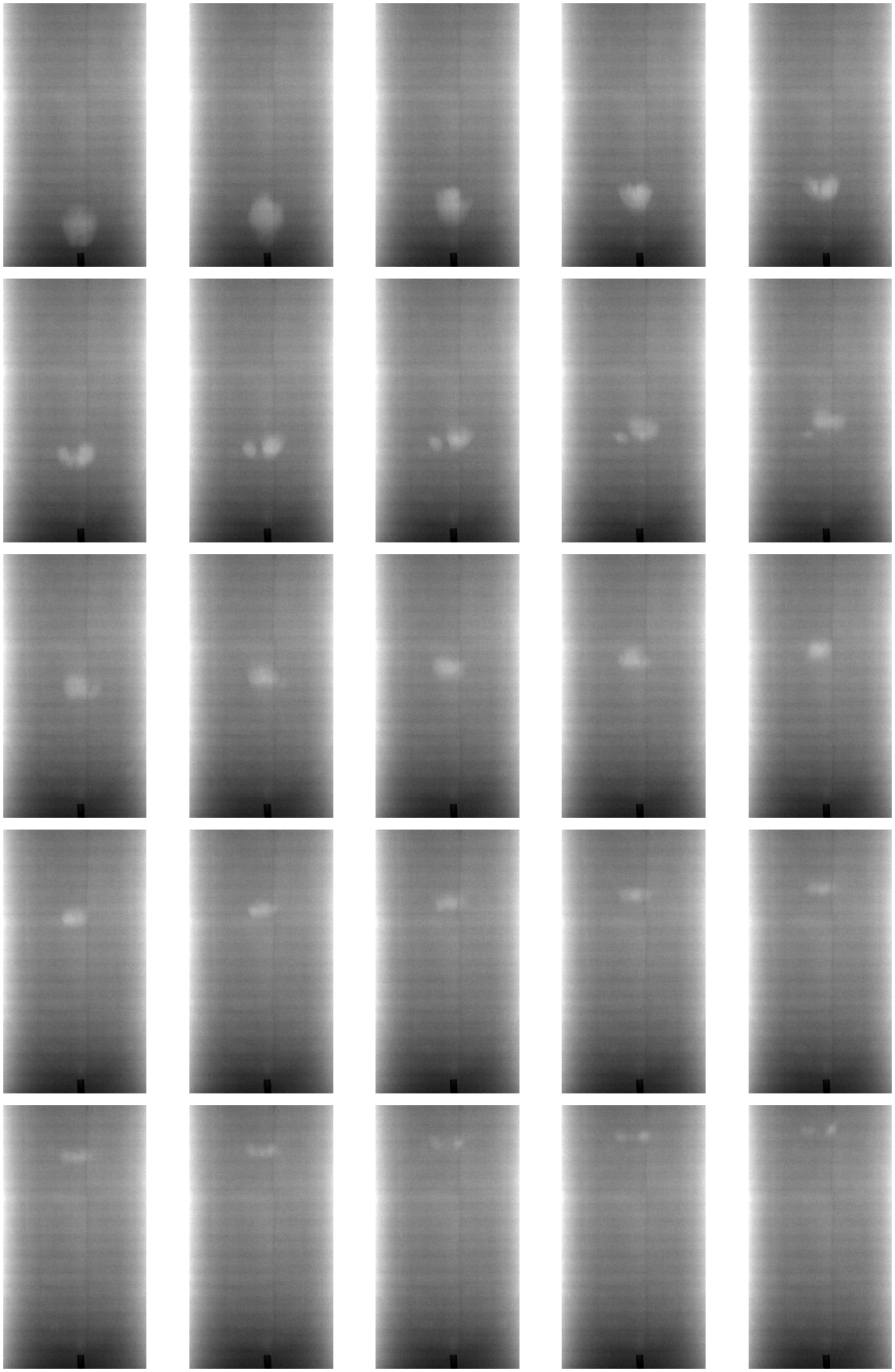

Table B.1: Single bubble motion in
System 1, U: 0.7Umf, $d_{eq,inj}$: 4.0 cm, f: 30 Hz

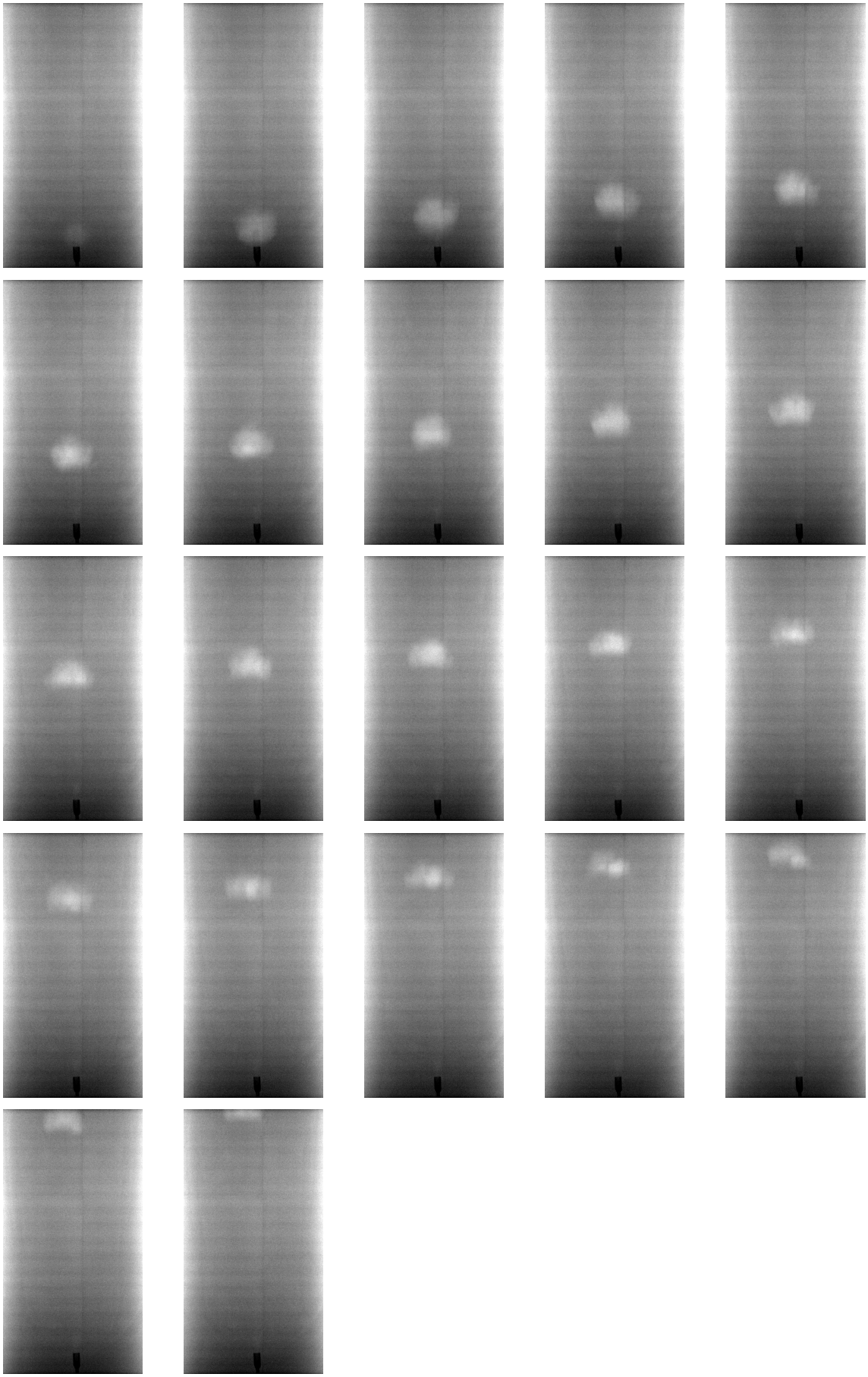

Table B.2: Single bubble motion in
System 1, U: Umf, $d_{eq,inj}$: 4.0 cm, f: 30 Hz

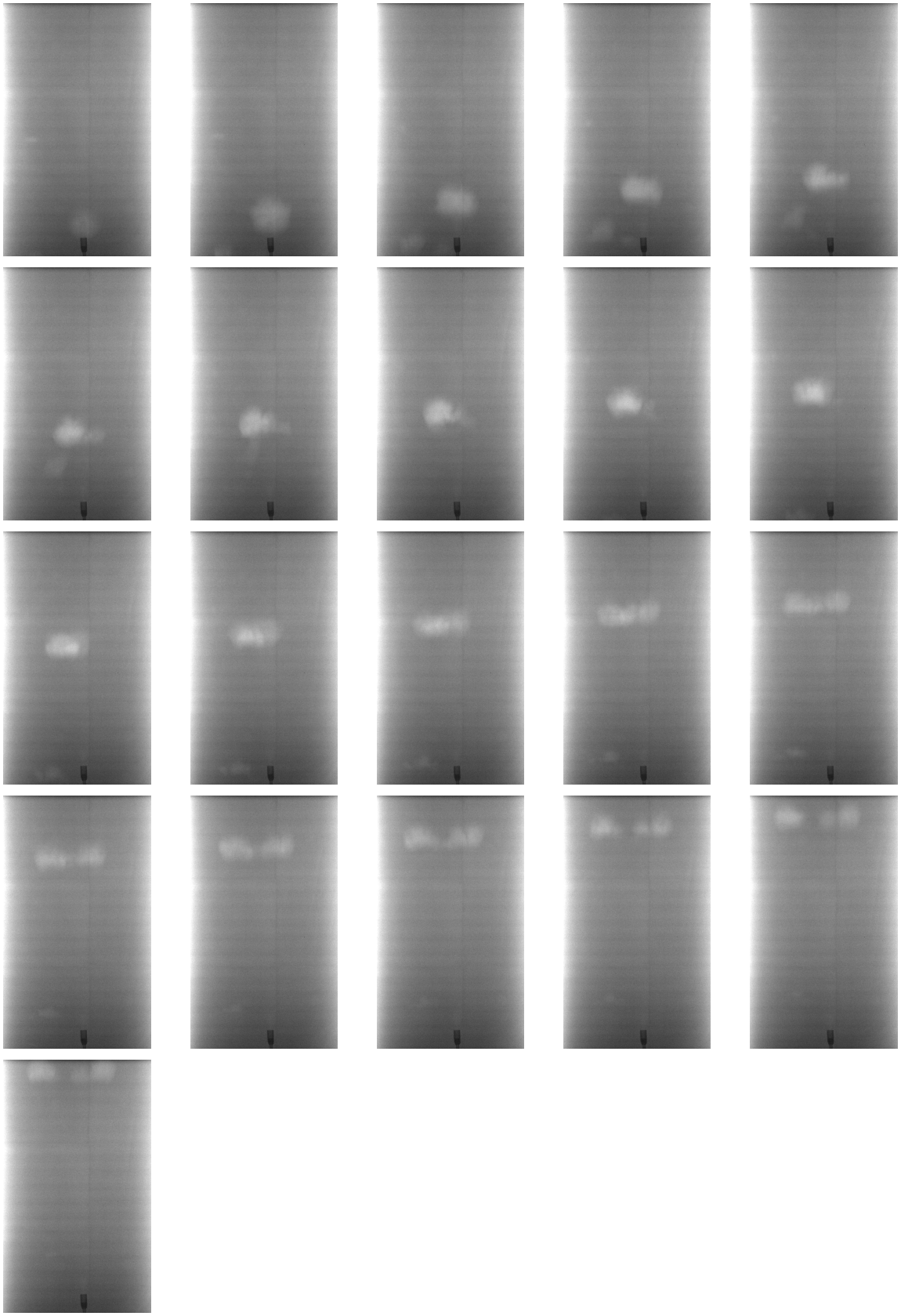

Table B.3: Single bubble motion in
System 1, U: 1.1Umf, $d_{eq,inj}$: 4.0 cm, f: 30 Hz

Processed Bubble Projection

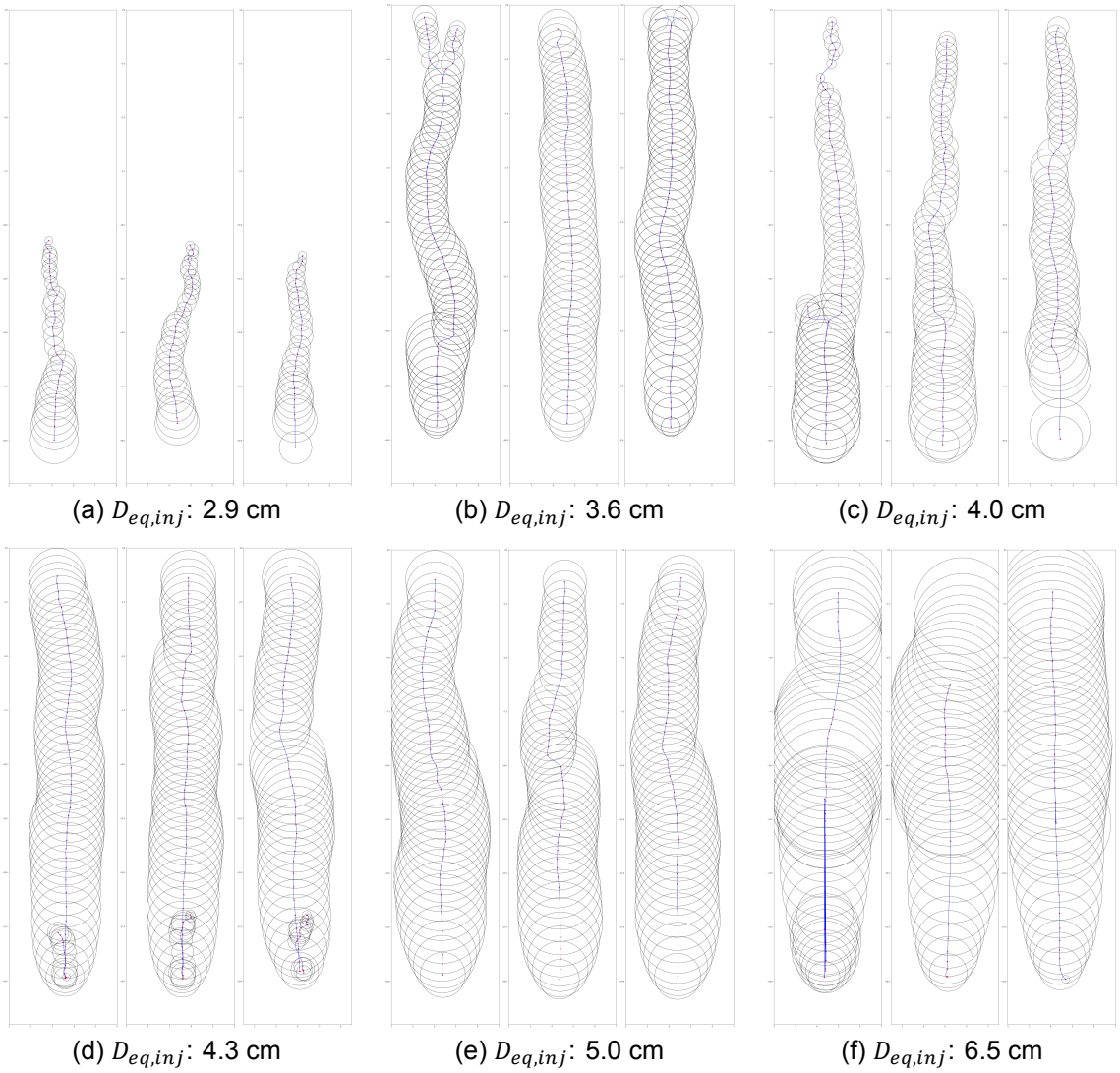

(a) $D_{eq,inj}$: 2.9 cm (b) $D_{eq,inj}$: 3.6 cm (c) $D_{eq,inj}$: 4.0 cm

(d) $D_{eq,inj}$: 4.3 cm (e) $D_{eq,inj}$: 5.0 cm (f) $D_{eq,inj}$: 6.5 cm

Figure B.1: Processed bubble projection
System 1, U: 0.7Umf, f: 65 Hz

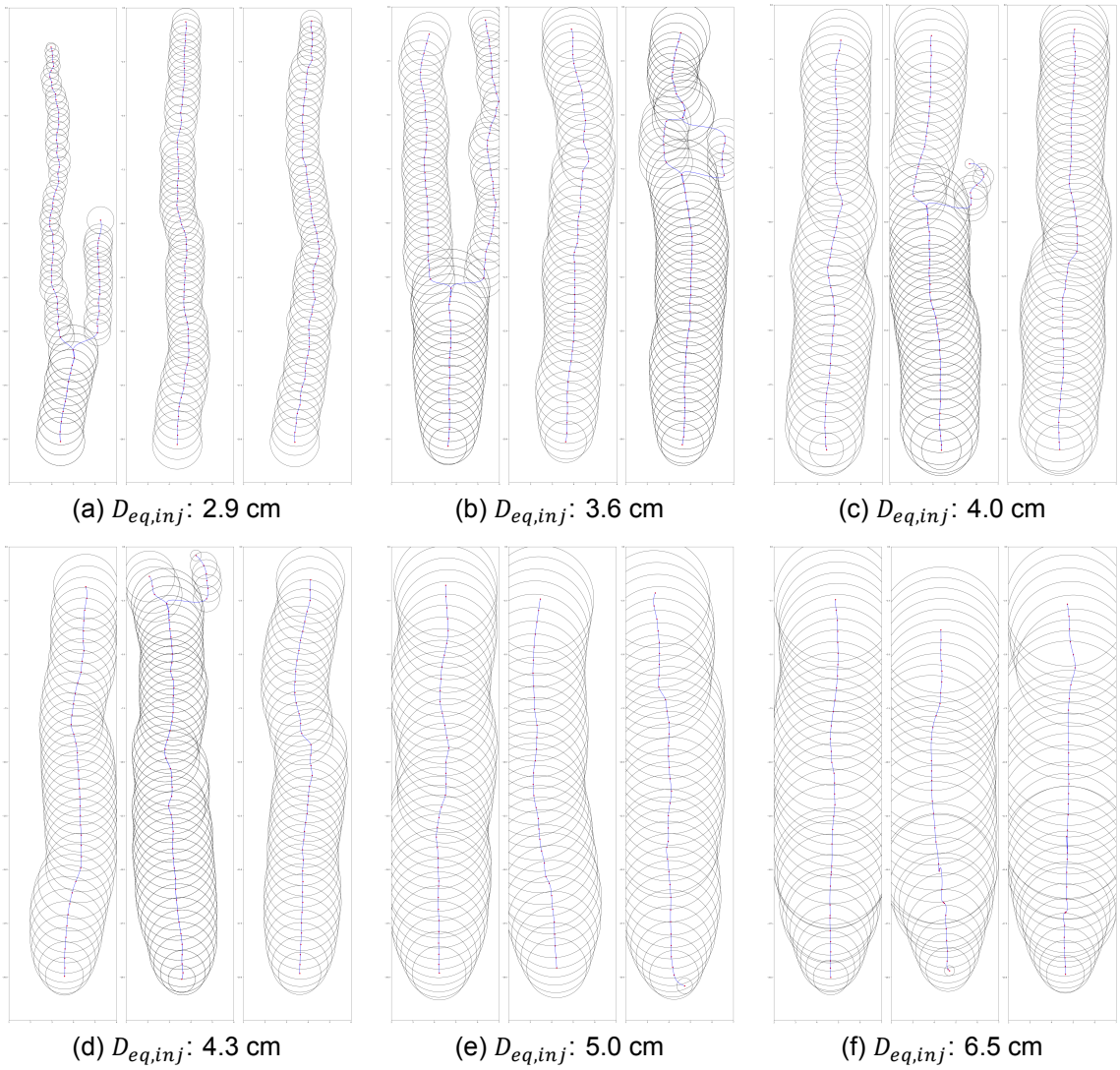

(a) $D_{eq,inj}$: 2.9 cm (b) $D_{eq,inj}$: 3.6 cm (c) $D_{eq,inj}$: 4.0 cm

(d) $D_{eq,inj}$: 4.3 cm (e) $D_{eq,inj}$: 5.0 cm (f) $D_{eq,inj}$: 6.5 cm

Figure B.2: Processed bubble projection
System 1, U: Umf, f: 65 Hz

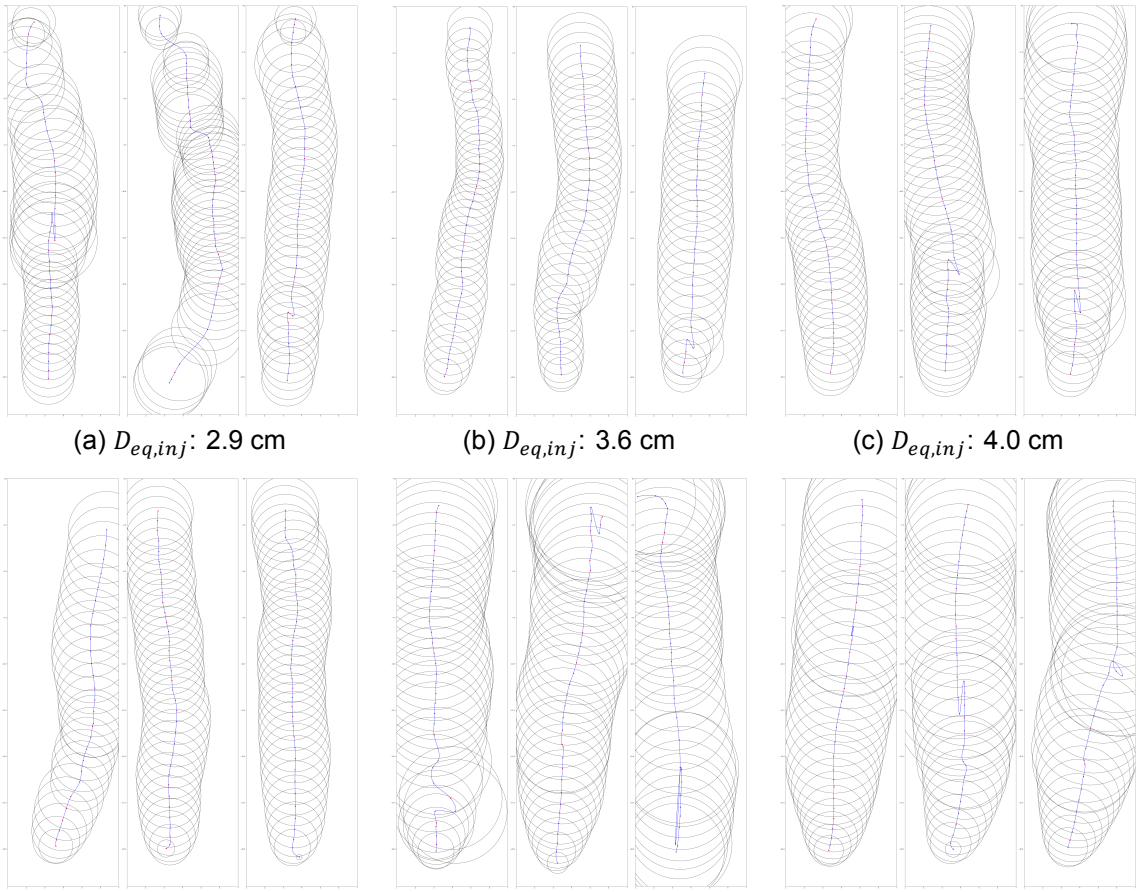

(a) $D_{eq,inj}$: 2.9 cm (b) $D_{eq,inj}$: 3.6 cm (c) $D_{eq,inj}$: 4.0 cm

(d) $D_{eq,inj}$: 4.3 cm (e) $D_{eq,inj}$: 5.0 cm (f) $D_{eq,inj}$: 6.5 cm

Figure B.3: Processed bubble projection
System 1, U: 1.1Umf, f: 30 Hz

B.1.2. D_{bed} : 15 cm, d_p: 0.2 mm, Q: 17 m/s [System 2]

Single Bubble Projection

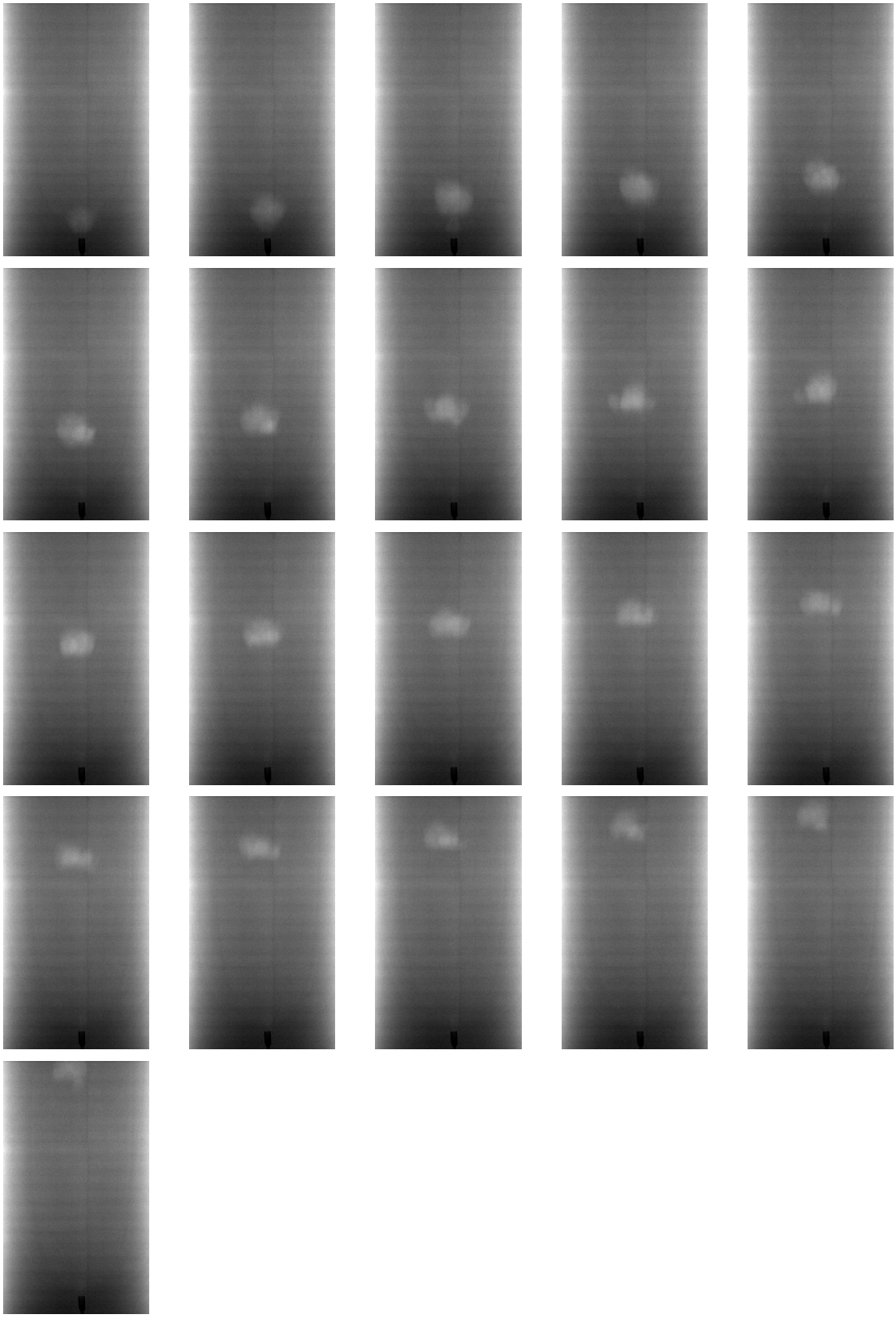

Table B.4: Single bubble motion in
System 2, U: Umf, $d_{eq,inj}$: 4.0 cm, f: 30 Hz

Processed Bubble Projection

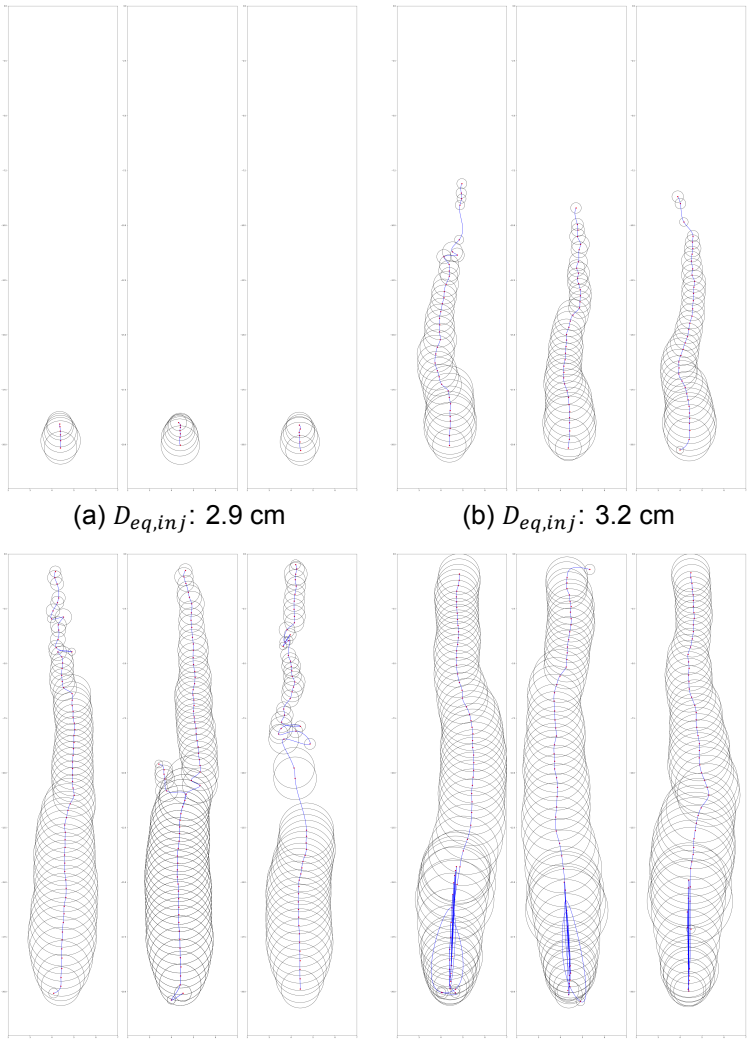

(a) $D_{eq,inj}$: 2.9 cm (b) $D_{eq,inj}$: 3.2 cm

(c) $D_{eq,inj}$: 4.0 cm (d) $D_{eq,inj}$: 5.1 cm

Figure B.4: Processed bubble projection
System 2, U: 0.7Umf, f: 30 Hz

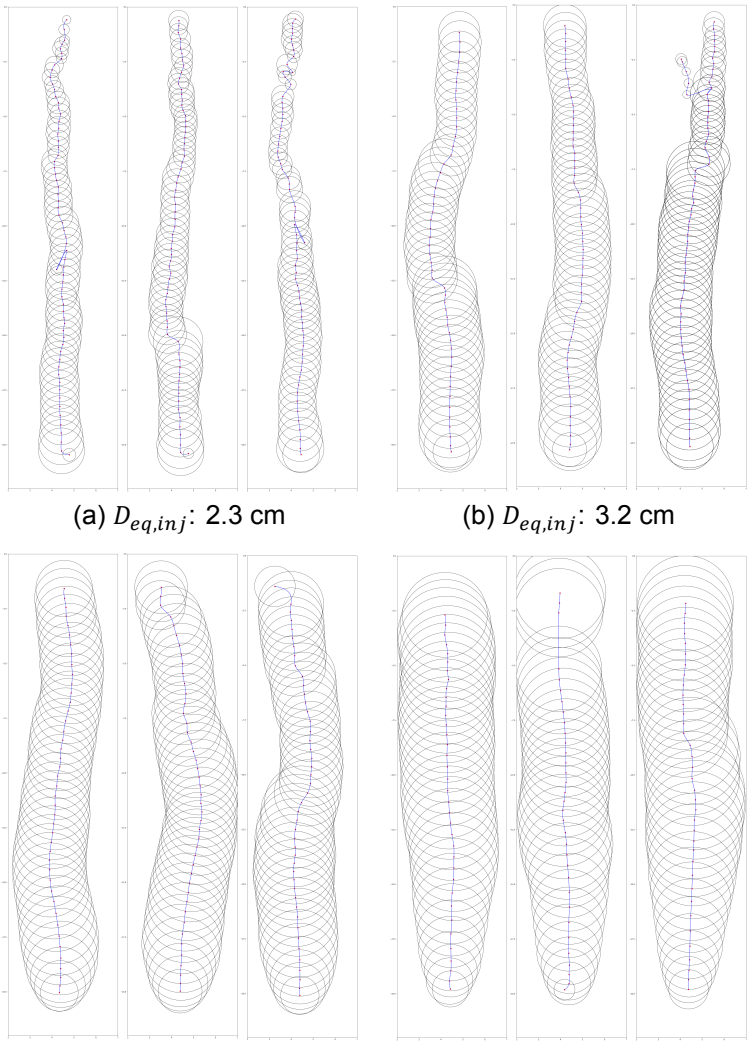

(a) $D_{eq,inj}$: 2.3 cm (b) $D_{eq,inj}$: 3.2 cm

(c) $D_{eq,inj}$: 4.0 cm (d) $D_{eq,inj}$: 5.1 cm

Figure B.5: Processed bubble projection
System 2, U: Umf, f: 65 Hz

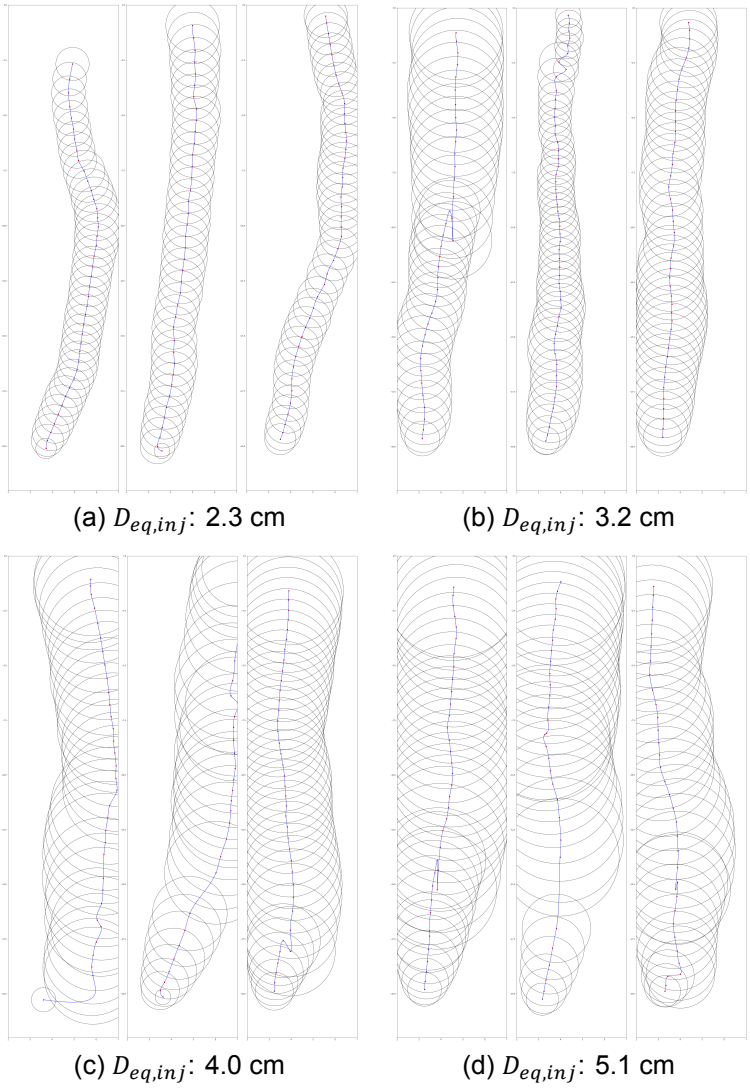

(a) $D_{eq,inj}$: 2.3 cm (b) $D_{eq,inj}$: 3.2 cm

(c) $D_{eq,inj}$: 4.0 cm (d) $D_{eq,inj}$: 5.1 cm

Figure B.6: Processed bubble projection
System 2, U: 1.1Umf, f: 65 Hz

B.1.3. D_{bed} : 15 cm, d_p: 0.5 mm, Q: 35 m/s [System 3] Single Bubble Projection

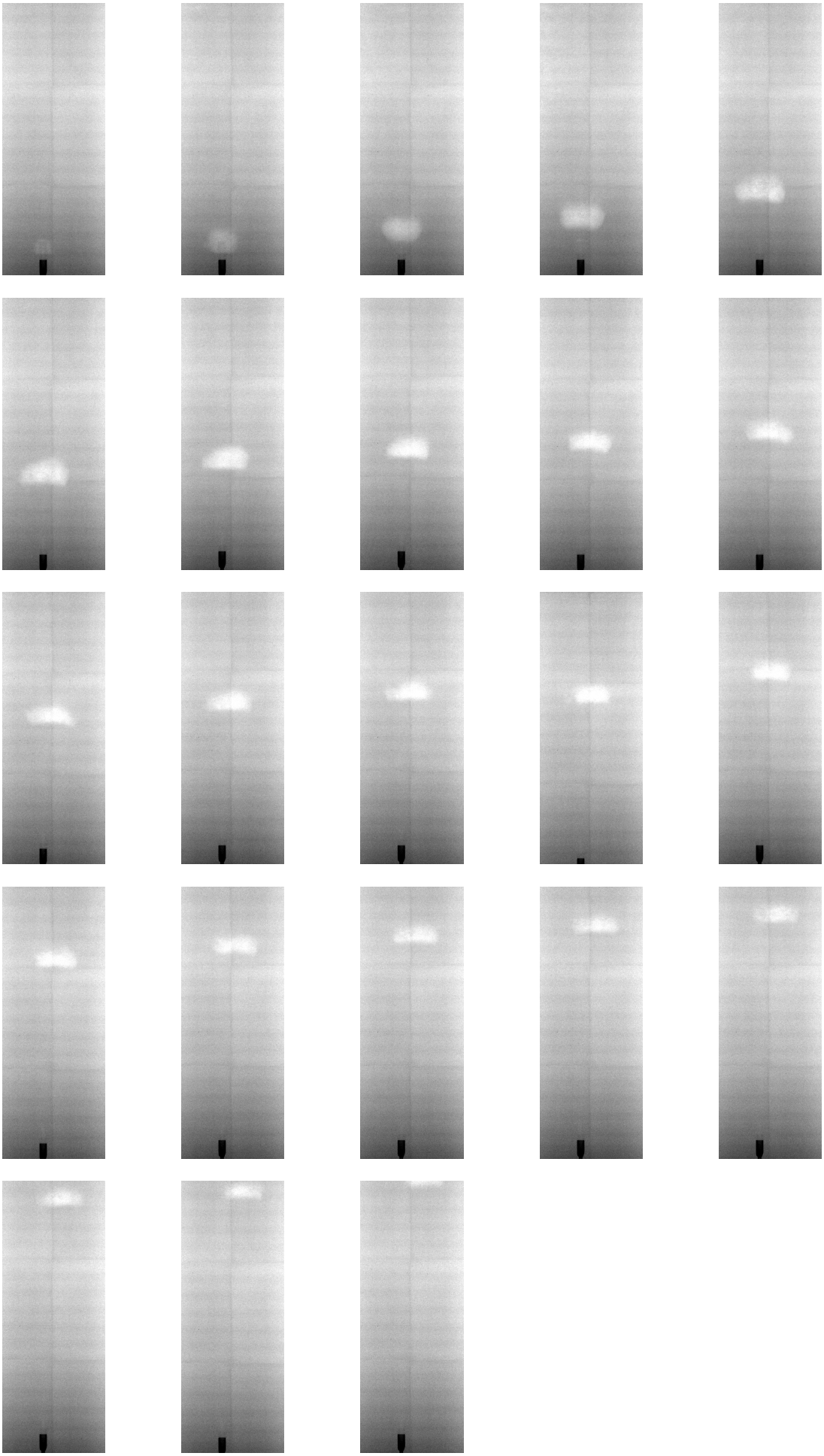

Table B.5: Single bubble motion in
System 3, U: Umf, $d_{eq,inj}$: 4.0 cm, f: 30 Hz

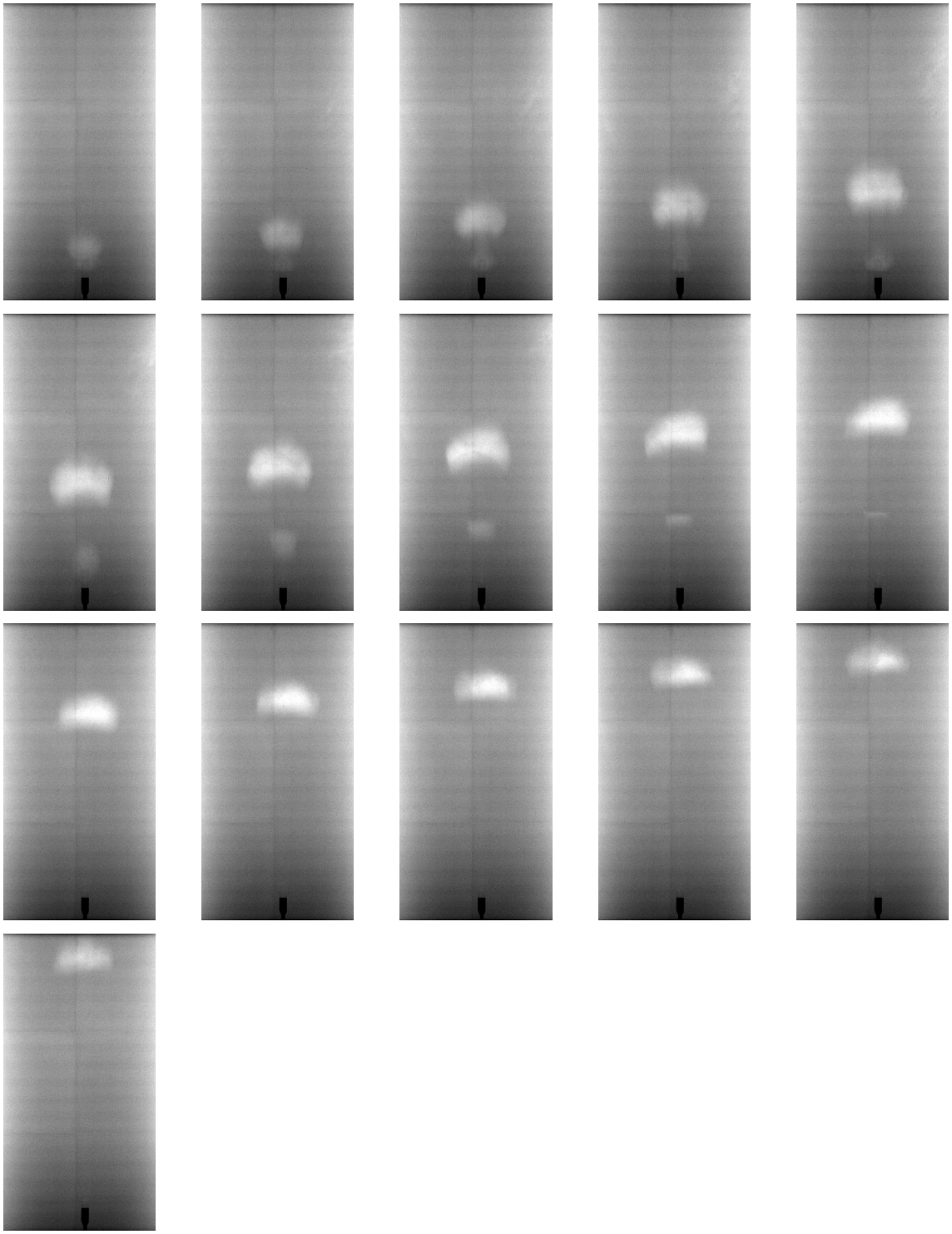

Table B.6: Single bubble motion in
System 3, U: Umf, $d_{eq,inj}$: 6.5 cm, f: 30 Hz

Processed Bubble Projection

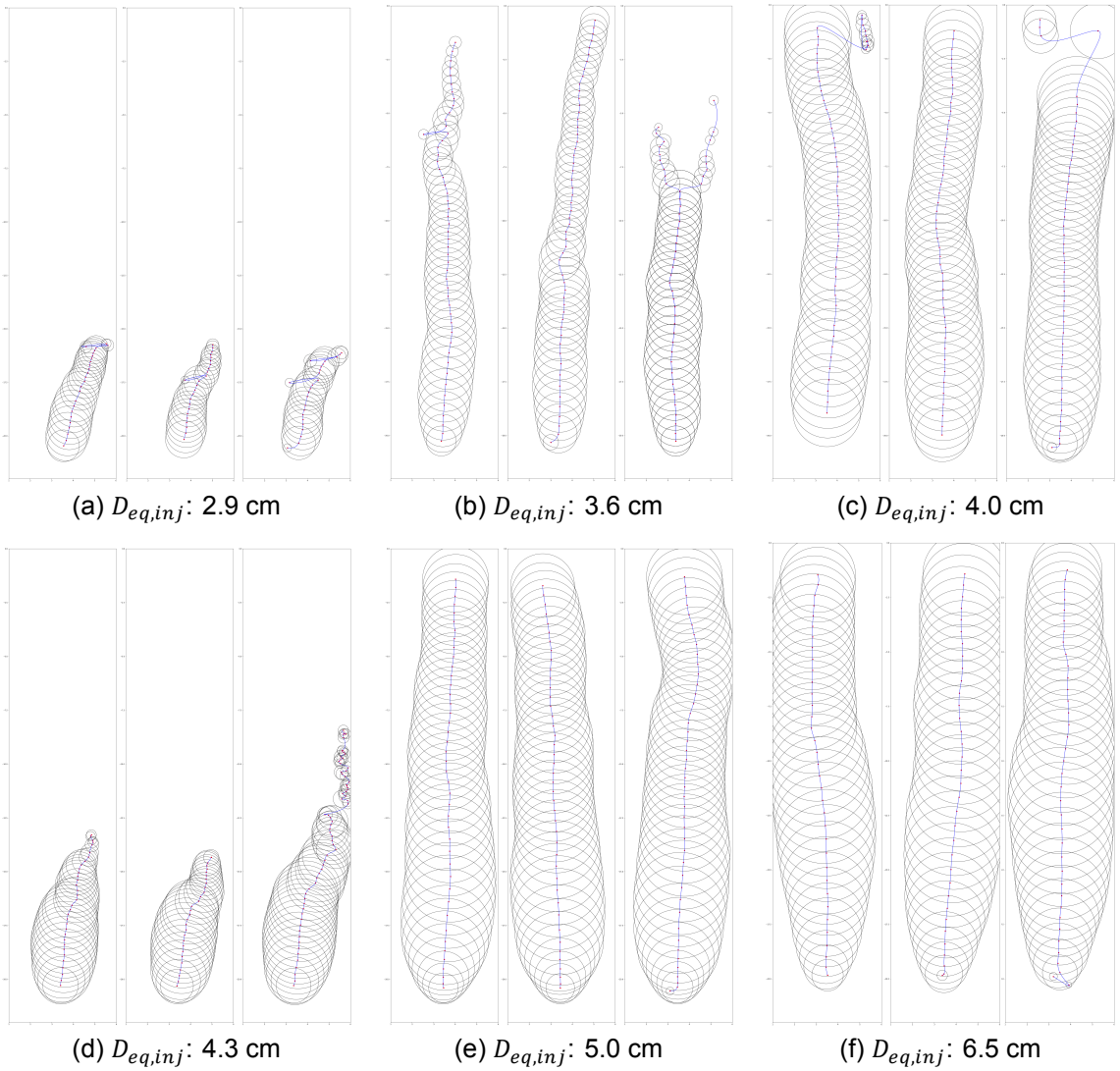

(a) $D_{eq,inj}$: 2.9 cm (b) $D_{eq,inj}$: 3.6 cm (c) $D_{eq,inj}$: 4.0 cm

(d) $D_{eq,inj}$: 4.3 cm (e) $D_{eq,inj}$: 5.0 cm (f) $D_{eq,inj}$: 6.5 cm

Figure B.7: Processed bubble projection
System 3, U: Umf, f: 65 Hz

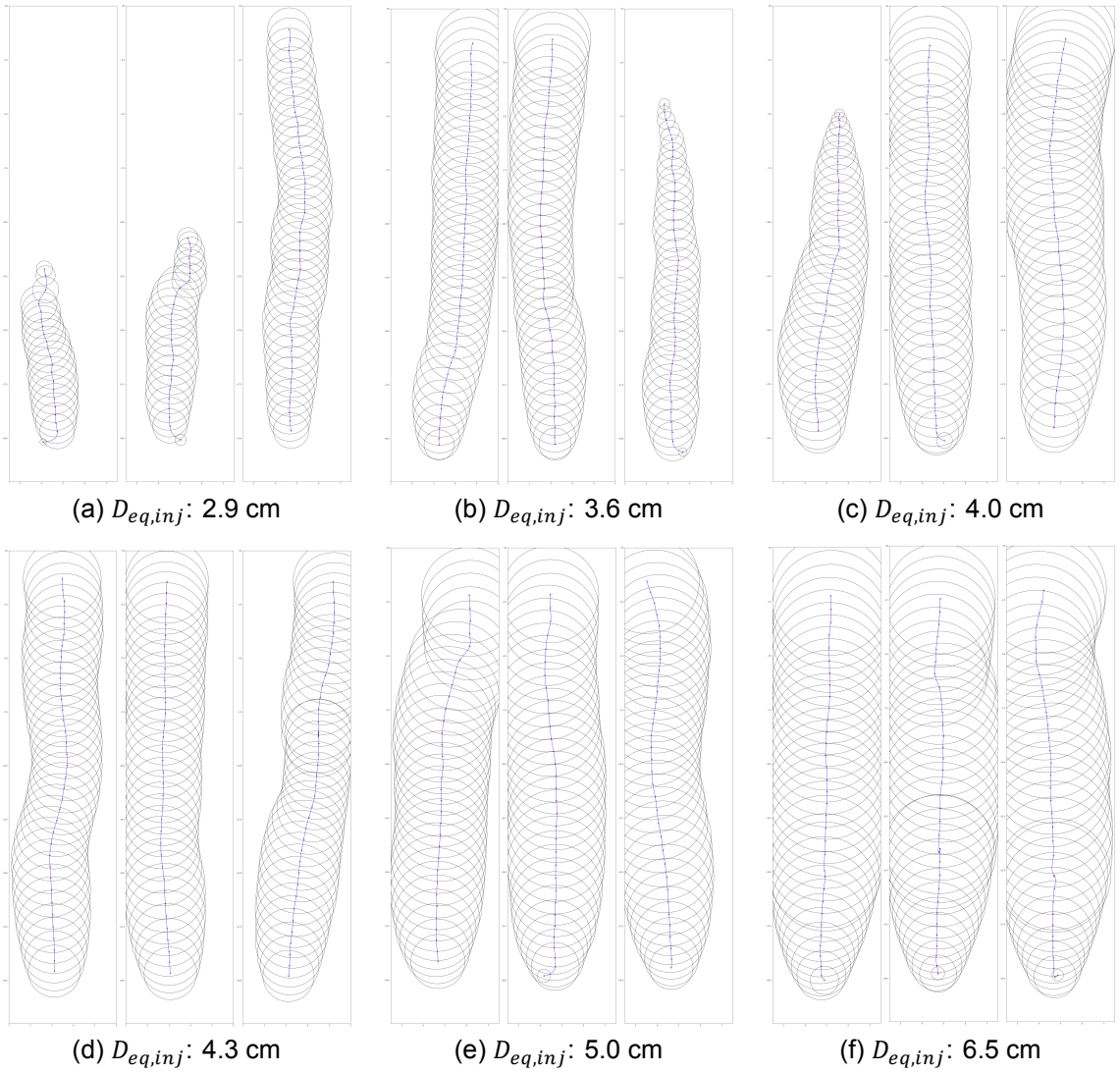

(a) $D_{eq,inj}$: 2.9 cm (b) $D_{eq,inj}$: 3.6 cm (c) $D_{eq,inj}$: 4.0 cm

(d) $D_{eq,inj}$: 4.3 cm (e) $D_{eq,inj}$: 5.0 cm (f) $D_{eq,inj}$: 6.5 cm

Figure B.8: Processed bubble projection
System 3, U: 1.1Umf, f: 65 Hz

B.1.4. D_{bed} : 5 cm, d_p: 0.2 mm, Q: 26 m/s [System 4]

Single Bubble Projection

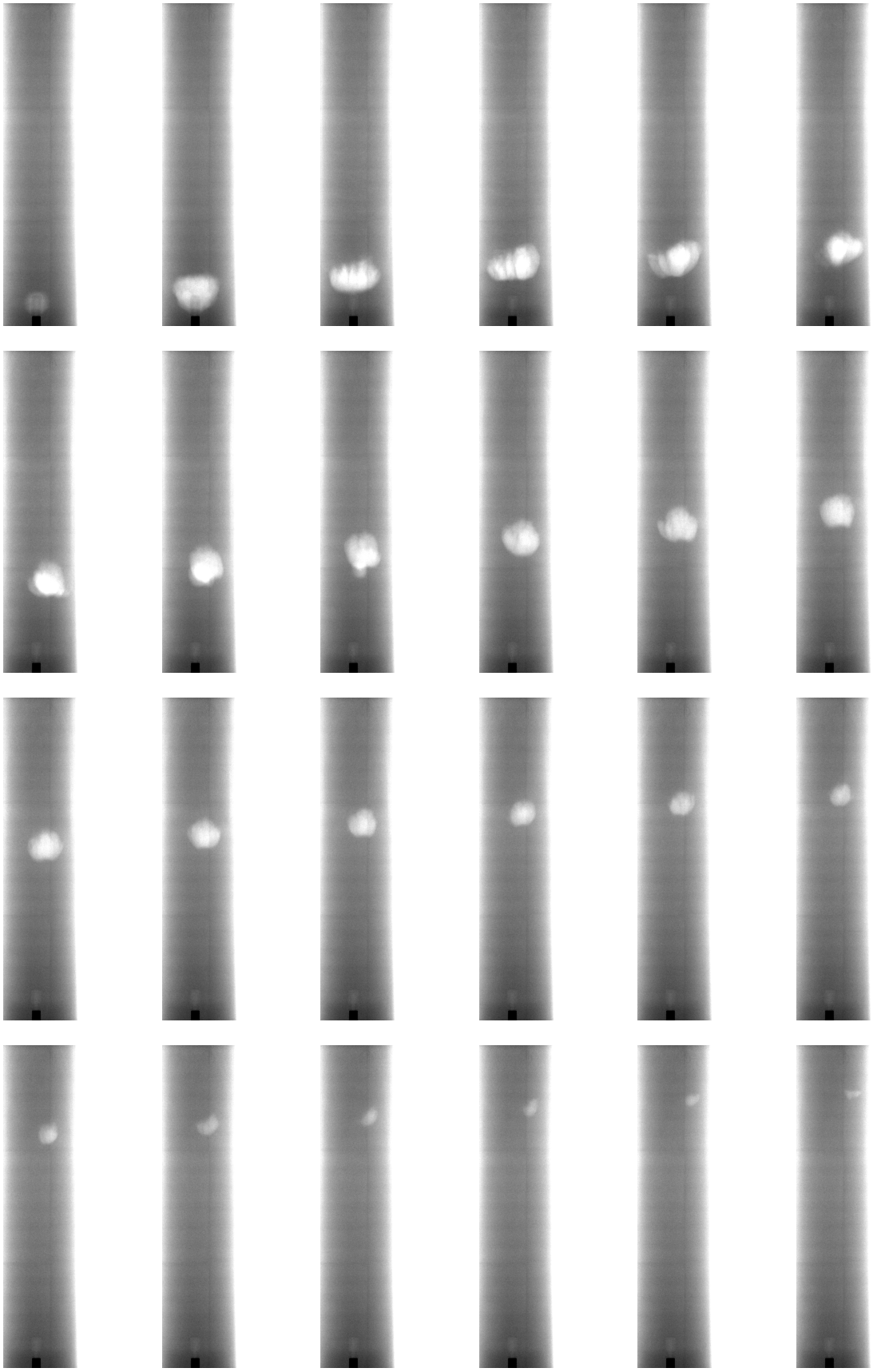

Table B.7: Single bubble motion in
System 4, U: 4 cm/s, $d_{eq,inj}$: 3.8 cm, f: 75 Hz

Processed Bubble Projection

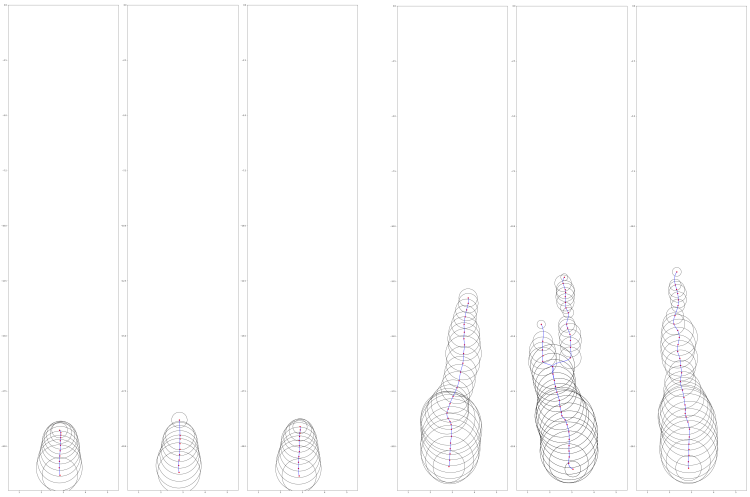

(a) $D_{eq,inj}$: 2.7 cm (b) $D_{eq,inj}$: 3.7 cm

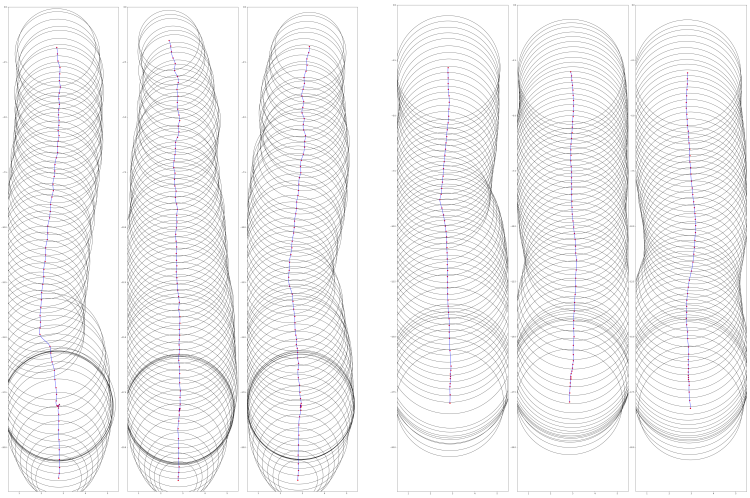

(c) $D_{eq,inj}$: 4.7 cm (d) $D_{eq,inj}$: 5.9 cm

Figure B.9: Processed bubble projection
System 4, U: 3 cm/s, f: 75 Hz

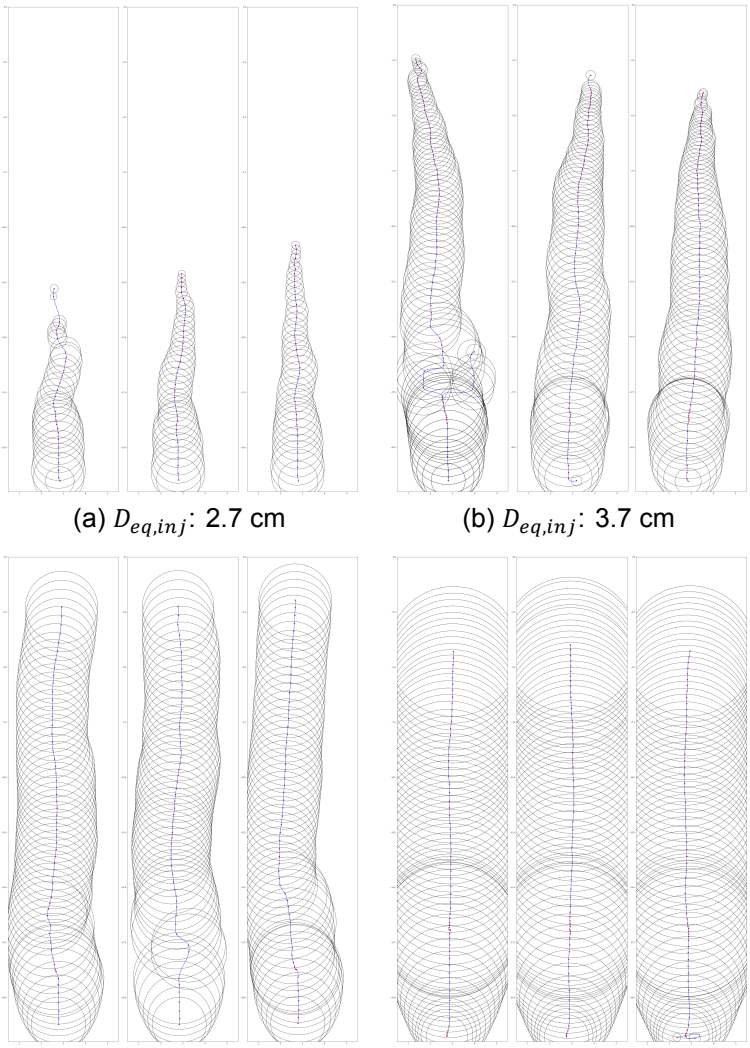

(a) $D_{eq,inj}$: 2.7 cm (b) $D_{eq,inj}$: 3.7 cm

(c) $D_{eq,inj}$: 4.7 cm (d) $D_{eq,inj}$: 5.9 cm

Figure B.10: Processed bubble projection
System 4, U: 4 cm/s, f: 75 Hz

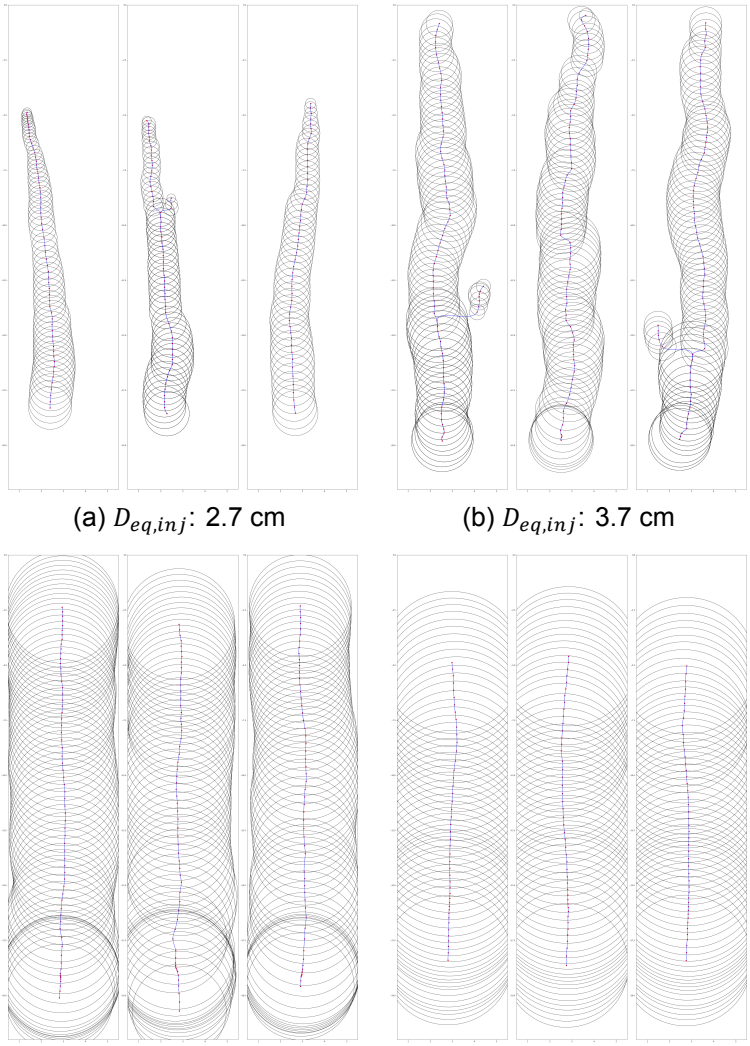

(a) $D_{eq,inj}$: 2.7 cm (b) $D_{eq,inj}$: 3.7 cm

(c) $D_{eq,inj}$: 4.7 cm (d) $D_{eq,inj}$: 5.9 cm

Figure B.11: Processed bubble projection
System 4, U: 5 cm/s, f: 75 Hz

B.2. Statistical Overview including secondary bubble

Within the formation stage analysis within the results section, there is a discussion of the observation that a secondary bubble forms at longer injection durations. This behavior was observed in Boyce et al. as well [14]. Within the results section, the statistical overview filtered the effects of the secondary bubble out for clarity. This appendix provides the statistical overview including the secondary bubble.

B.2.1. D_{bed} : 15 cm, d_p: 0.2 mm, Q: 35 m/s [System 1]

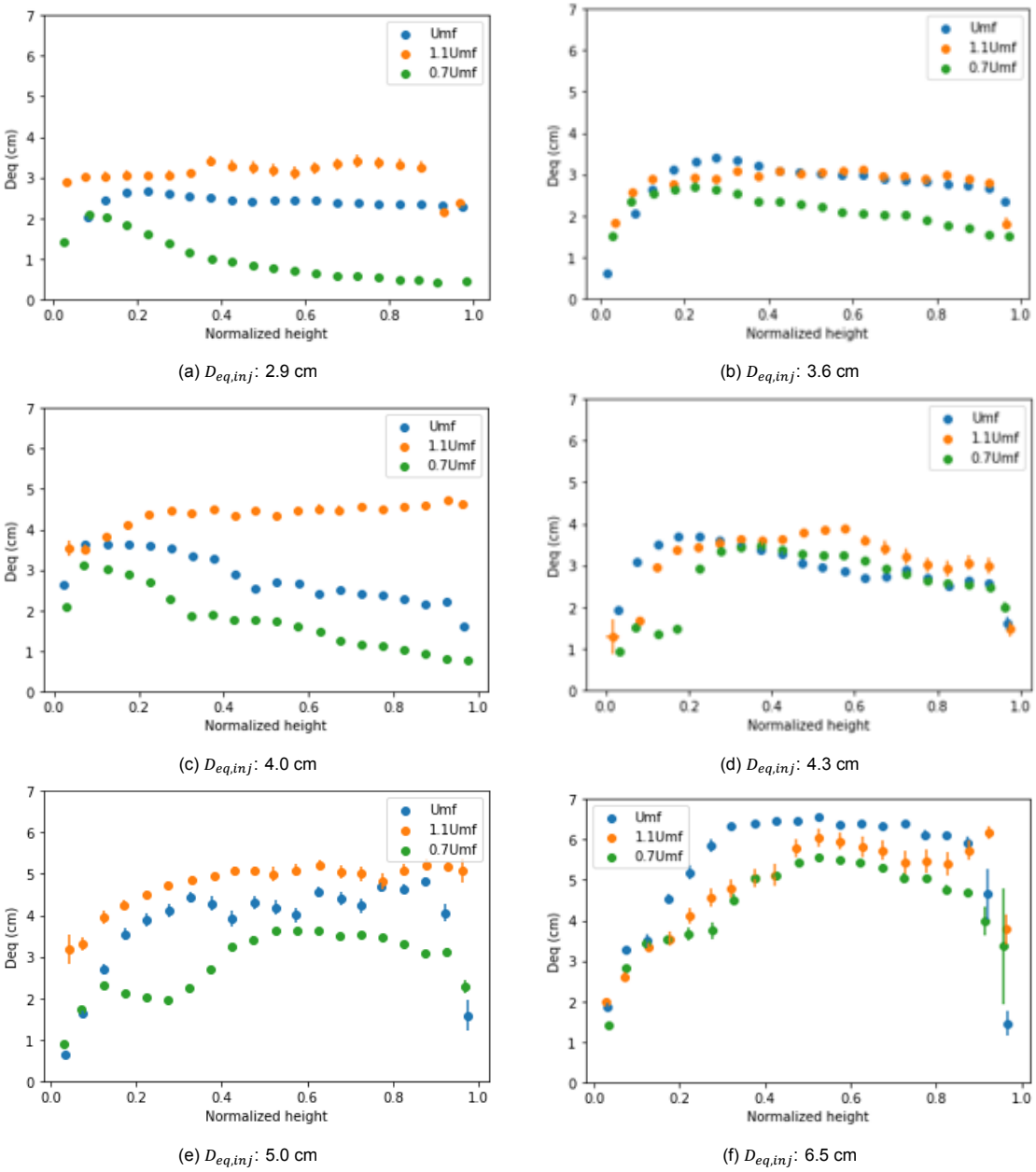

(a) $D_{eq,inj}$: 2.9 cm

(b) $D_{eq,inj}$: 3.6 cm

(c) $D_{eq,inj}$: 4.0 cm

(d) $D_{eq,inj}$: 4.3 cm

(e) $D_{eq,inj}$: 5.0 cm

(f) $D_{eq,inj}$: 6.5 cm

Figure B.12: d_{eq} over the normalized height of the projection frame for system 1
Secondary bubble present

B.2.2. D_{bed} : 15 cm, d_p: 0.5 mm, Q: 35 m/s [System 3]

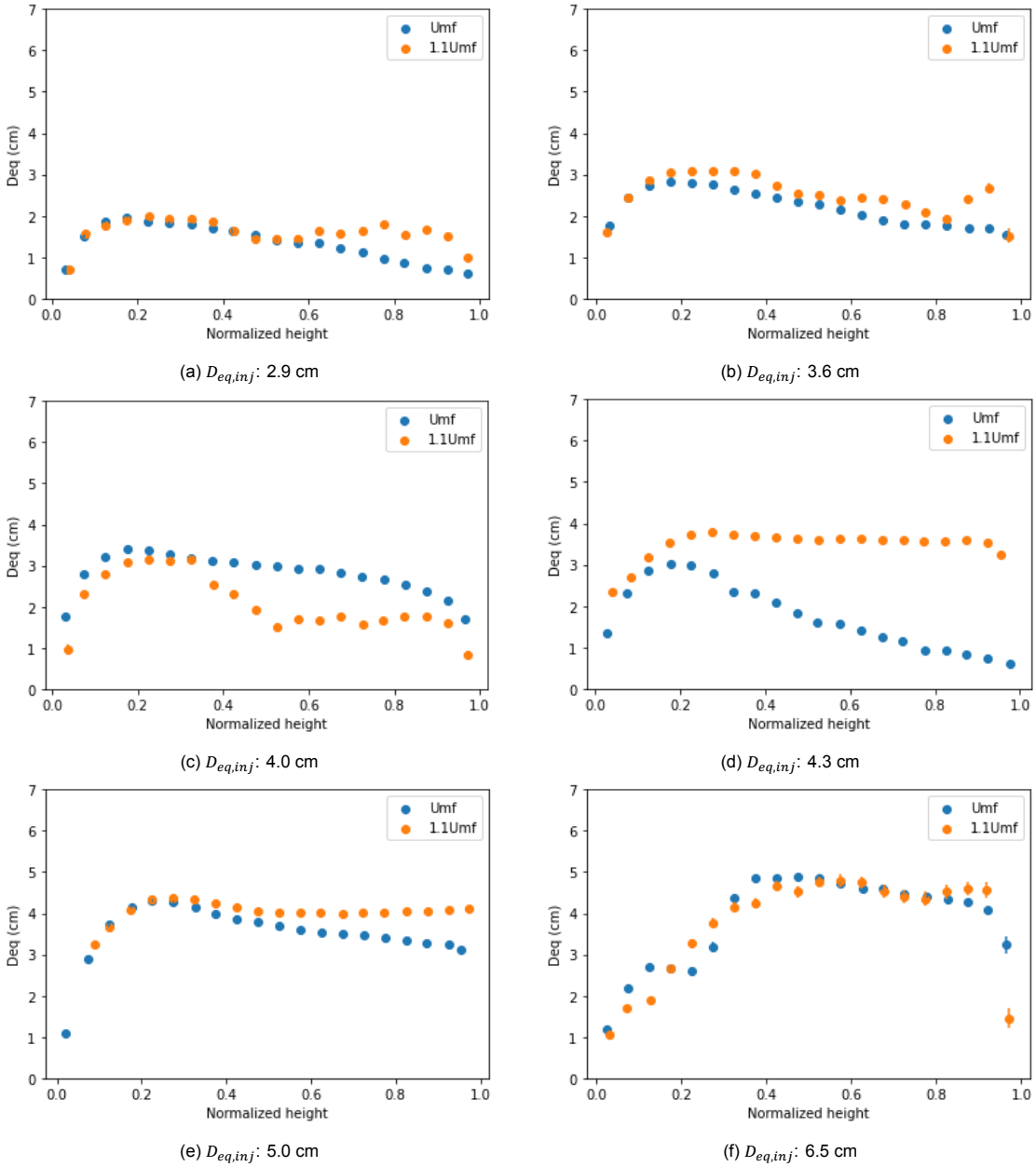

(a) $D_{eq,inj}$: 2.9 cm

(b) $D_{eq,inj}$: 3.6 cm

(c) $D_{eq,inj}$: 4.0 cm

(d) $D_{eq,inj}$: 4.3 cm

(e) $D_{eq,inj}$: 5.0 cm

(f) $D_{eq,inj}$: 6.5 cm

Figure B.13: d_{eq} over the normalized height of the projection frame for system 3
Secondary bubble present

B.3. 3D Reconstruction

B.3.1. Calibration

The calibration of the script must be done to obtain accurate 3D reconstructions. A calibration column is used to measure the distance of the x-ray source/detector pairs from the column used in experimentation. Further information about the 3D reconstruction can be found in Graas et al. [16]. The calibration column is a column with needles attached at specific intervals along the outer walls of the column. The calibration column rotates 360°, and x-ray projections of the calibration column are taken.

After the projections of the calibration column are taken, the calibration within the script must be done. The calibration within the script requires selection of the sharp ends of the needles at 3 evenly spaced angles from 3 frames. This is done for all of the x-ray sources/detector pairs. Two types of

needles were attached to the calibration column: ball point needle (B) and sewing needle (E). The orientation of the needles can be in two directions: pointed towards the top of the column (stake) or pointed towards the base of the column (drill). One completed frame of the calibration from the script can be seen in Figure B.14.

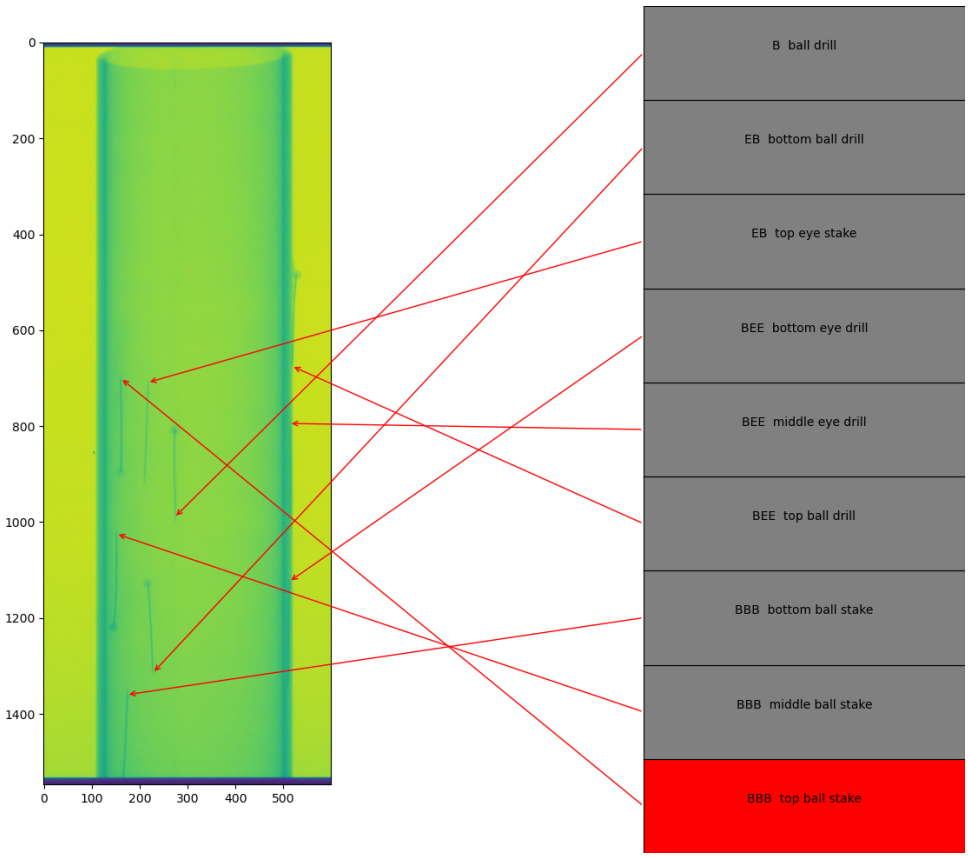

Figure B.14: Reconstruction Calibration

B.3.2. Column Turn Around

The 3D reconstruction provides an array, which are analyzed in MATLAB. Within MATLAB, the Volume Visualization tool is utilized to obtain images of the 3D reconstruction column rotating at intervals of 30°. A full 360° view of the 3D reconstructions are presented.

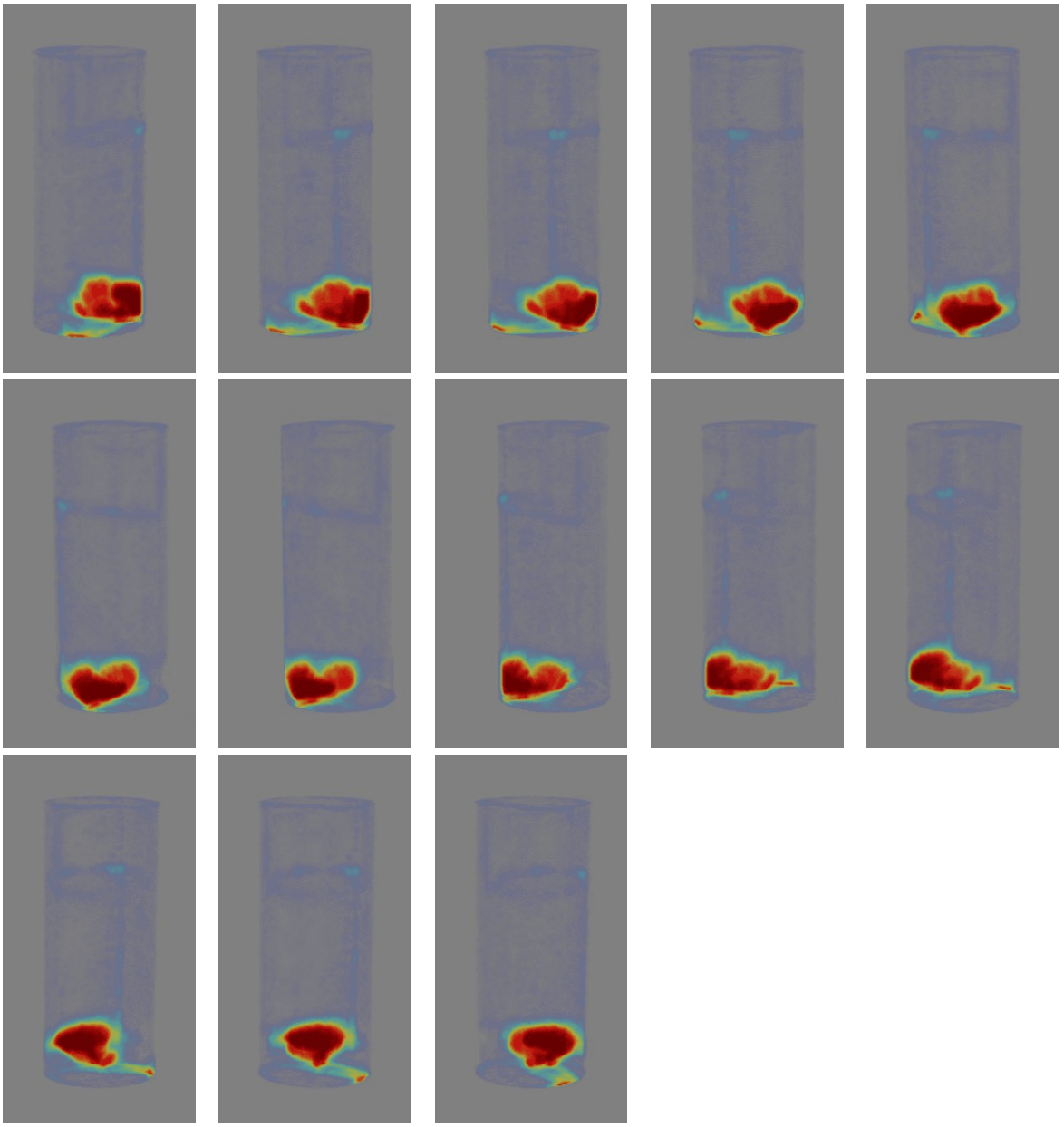

Table B.8: Single bubble motion in
System 4, U: 4 cm/s, $d_{eq,inj}$: 3.8 cm, f: 75 Hz

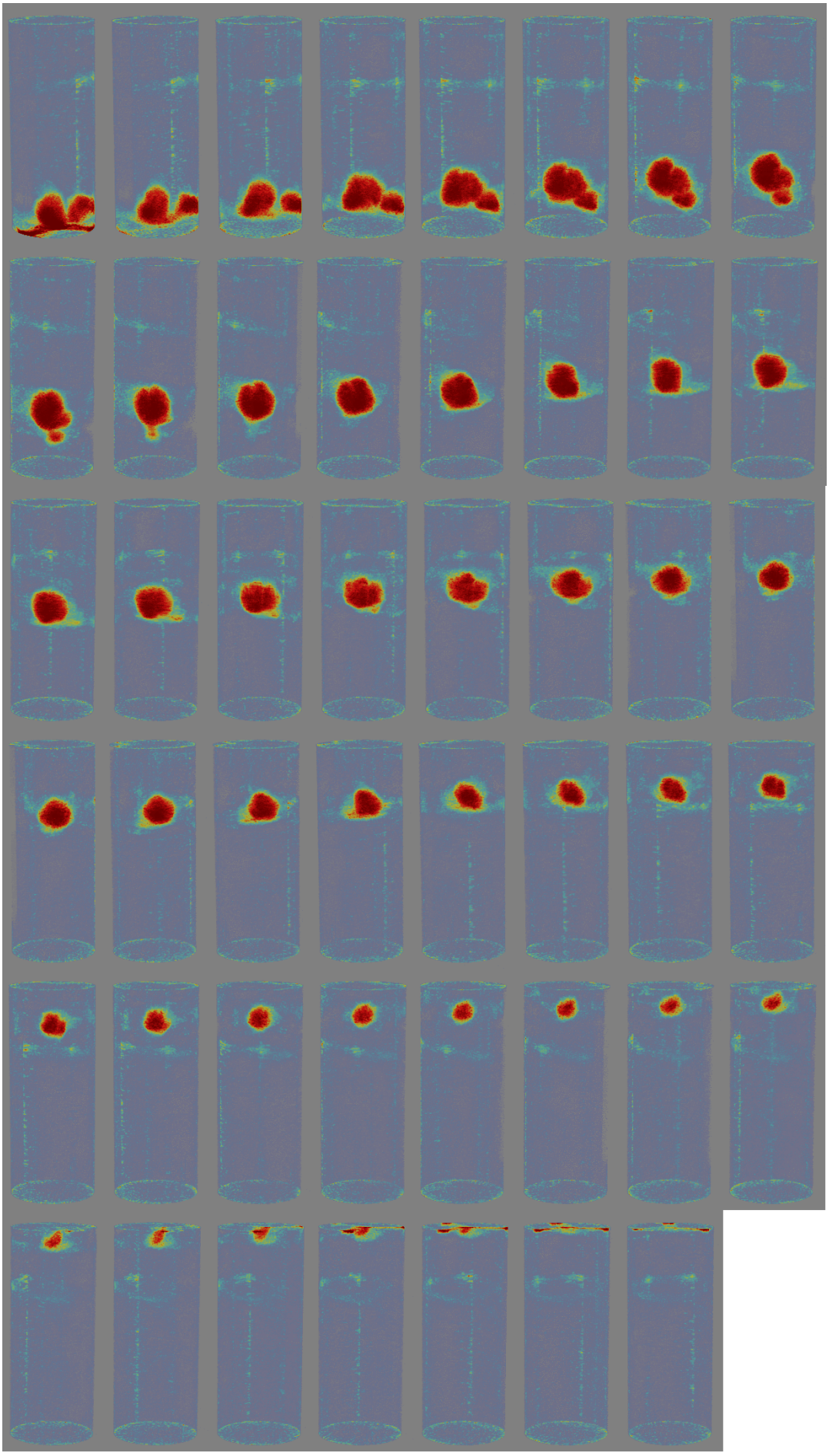

Figure B.15: bubble motion in for duration of reconstruction length
System 4, U: 4 cm/s, $d_{eq,inj}$: 3.8 cm, f: 75 Hz

C

Appendix C

C.1. Kato-Wen and Werther

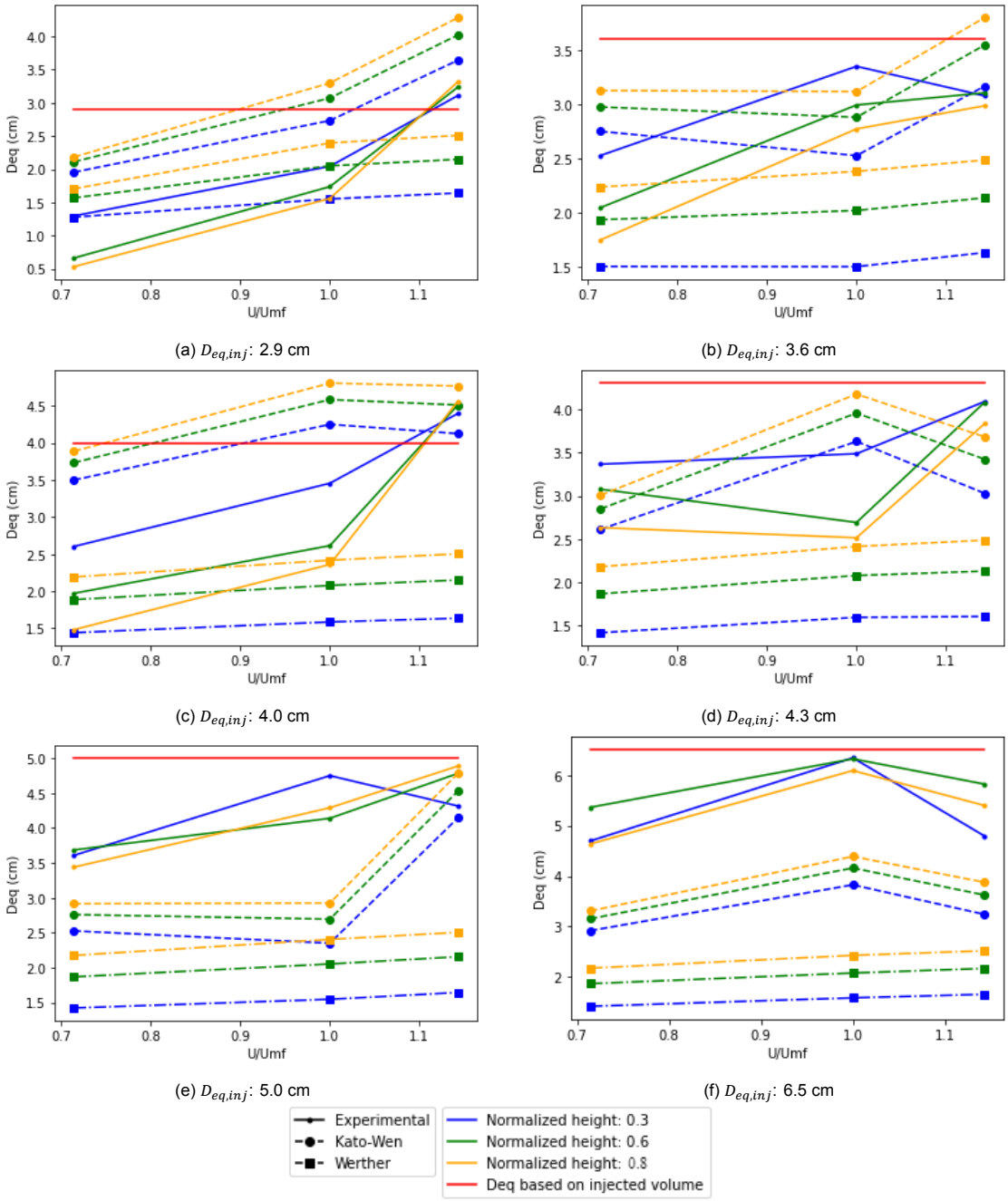

(a) $D_{eq,inj}$: 2.9 cm

(b) $D_{eq,inj}$: 3.6 cm

(c) $D_{eq,inj}$: 4.0 cm

(d) $D_{eq,inj}$: 4.3 cm

(e) $D_{eq,inj}$: 5.0 cm

(f) $D_{eq,inj}$: 6.5 cm

Figure C.1: Comparison of the experimental and Kato-Wen and Werther correlations at three normalized heights in the column D_{bed}: 15 cm, d_p:0.2mm, Q: 35 m/s [System 1]

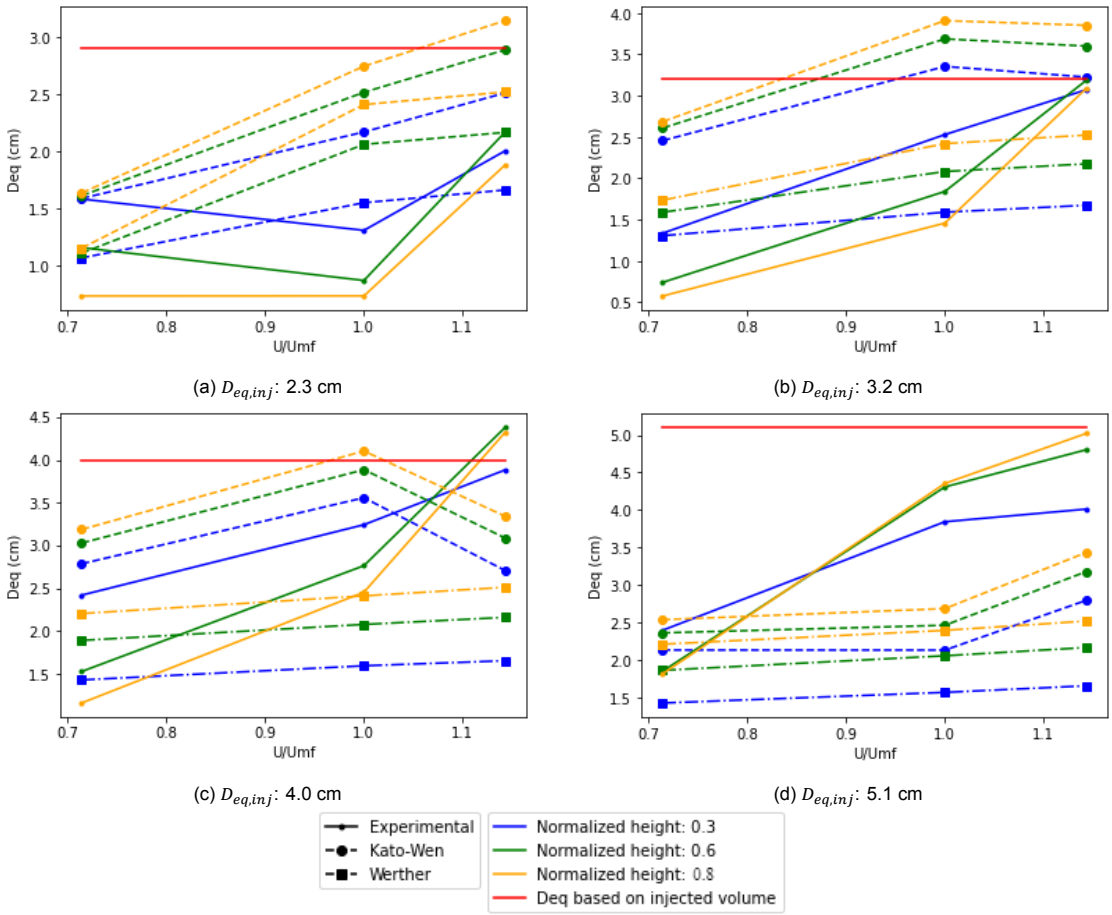

(a) $D_{eq,inj}$: 2.3 cm

(b) $D_{eq,inj}$: 3.2 cm

(c) $D_{eq,inj}$: 4.0 cm

(d) $D_{eq,inj}$: 5.1 cm

Figure C.2: Comparison of the experimental and Kato-Wen and Werther correlations at three normalized heights in the column D_{bed}: 15 cm, d_p:0.2mm, Q: 17 m/s [System 2]

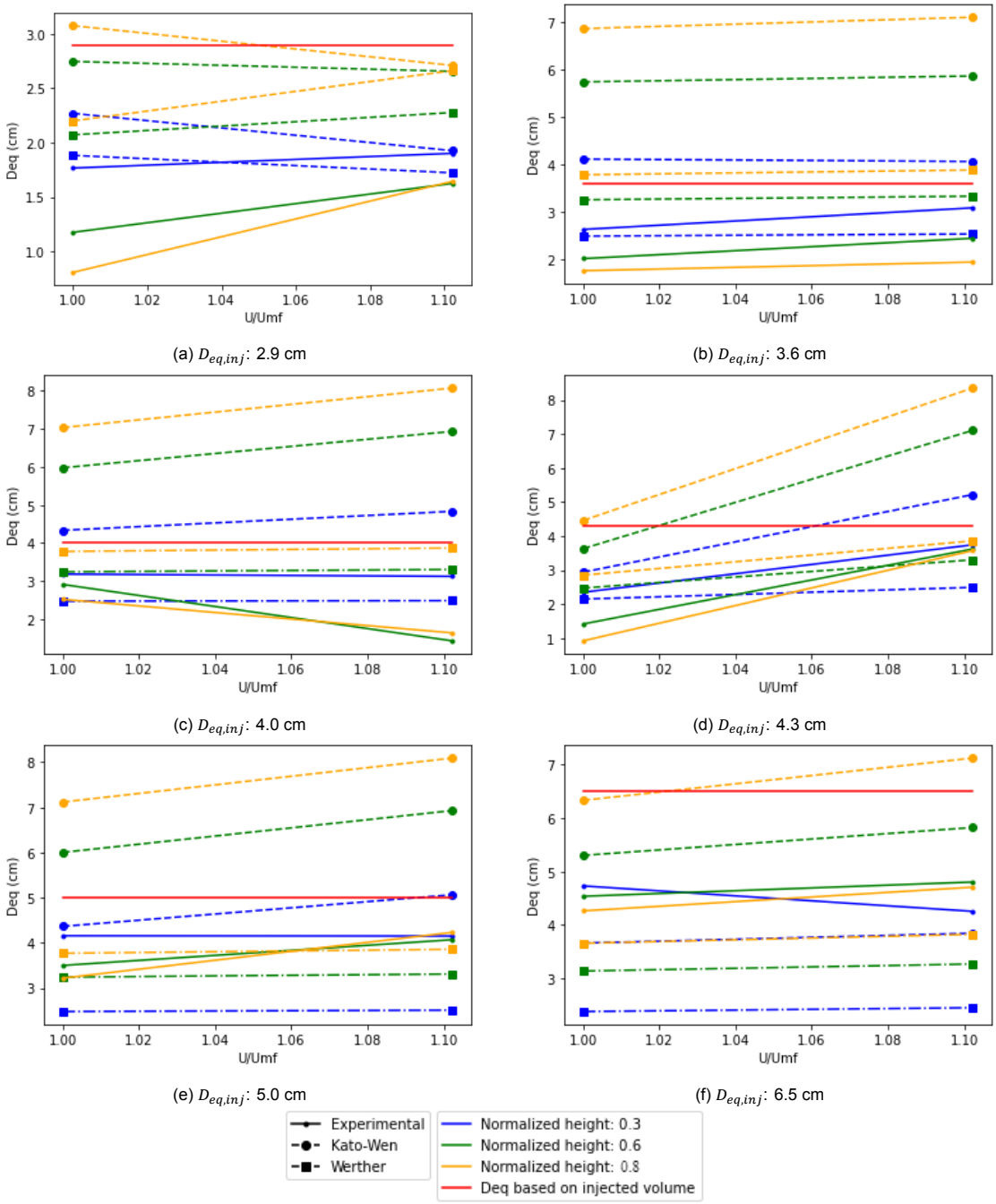

(a) $D_{eq,inj}$: 2.9 cm

(b) $D_{eq,inj}$: 3.6 cm

(c) $D_{eq,inj}$: 4.0 cm

(d) $D_{eq,inj}$: 4.3 cm

(e) $D_{eq,inj}$: 5.0 cm

(f) $D_{eq,inj}$: 6.5 cm

Figure C.3: Comparison of the experimental and Kato-Wen and Werther correlations at three normalized heights in the column D_{bed}: 15 cm, d_p:0.5mm, Q: 35 m/s [System 3]

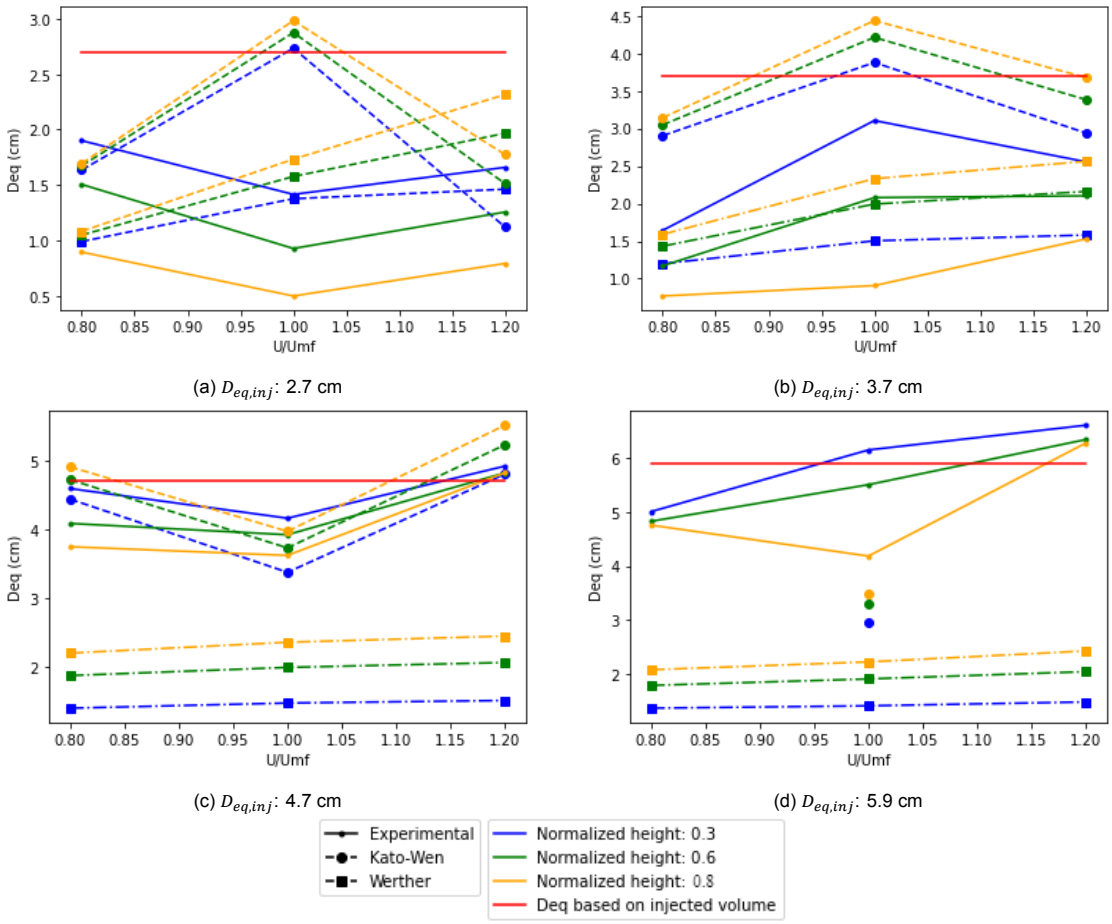

(a) $D_{eq,inj}$: 2.7 cm (b) $D_{eq,inj}$: 3.7 cm

(c) $D_{eq,inj}$: 4.7 cm (d) $D_{eq,inj}$: 5.9 cm

Figure C.4: Comparison of the experimental and Kato-Wen and Werther correlations at three normalized heights in the column D_{bed}: 5 cm, d_p:0.2mm, Q: 26 m/s [System 4]

C.2. Froude Number

.

C.2.1. Aspect Ratio

Figure C.5 takes the average aspect ratio of the 30 bubbles for every level of background fluidization and $d_{eq,inj}$, represented by the different colors. Overall, the width of the bubble is greater than the width of the bubble, suggesting an ellipsoidal bubble forms. Bubbles with lower injection durations and during the formation of the bubble have a tendency to be prolate ellipsoids; however, the majority tend to form oblate ellipsoids.

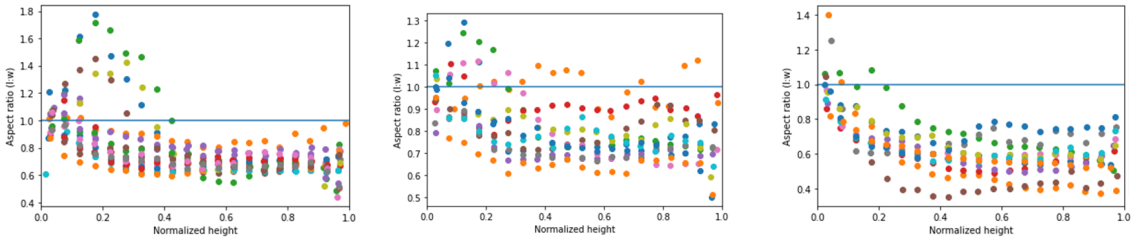

(a) System 1 (b) System 2 (c) System 3

Figure C.5: Average aspect ratio (L:W) over the normalized height based on the projection frame

Figure C.6 compares the aspect ratio of the bubble in terms of length/width over the bubble rise velocity. There are few bubbles that are spherical or prolate ellipsoids.

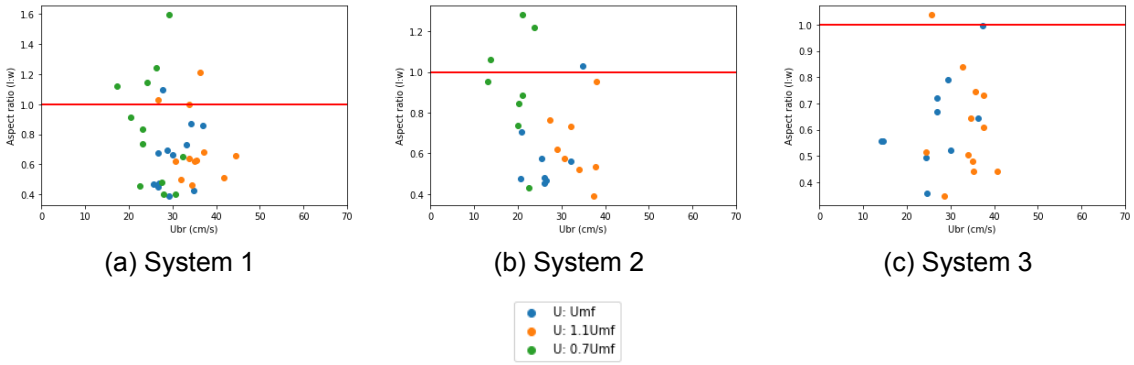

(a) System 1 (b) System 2 (c) System 3

Figure C.6: Aspect ratio (L:W) for the u_{br}

C.2.2. Froude number comparisons

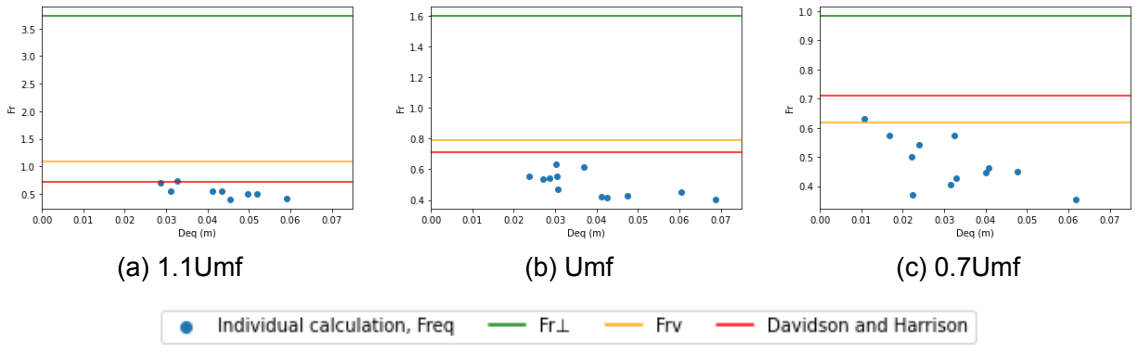

(a) 1.1Umf (b) Umf (c) 0.7Umf

Figure C.7: Different Froude number based on level of background fluidization for system 1

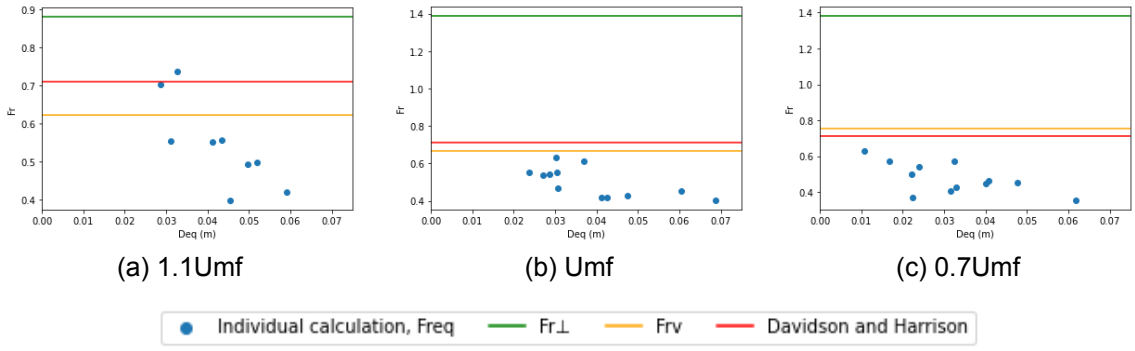

(a) 1.1Umf (b) Umf (c) 0.7Umf

Figure C.8: Different Froude number based on level of background fluidization for system 2

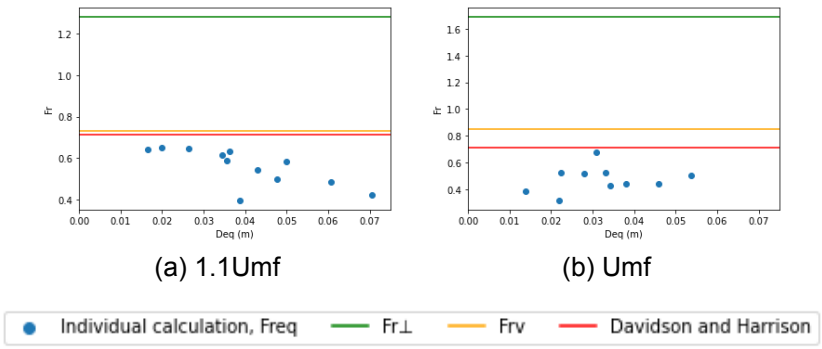

(a) 1.1Umf (b) Umf

Figure C.9: Different Froude number based on level of background fluidization for system 3

Appendix D

D.1. Slice Stacking Script

The following script is utilized to determine the slice stacked volume of the bubble and calculate the subsequent d_{eq}, A_{sb}, and $D_{eq,asb}$.

```
deq_store =[] #storage of the deq
asb_store = [] #storage of the interfacial surface area
deqa_store =[] #storage of the deq based on asb
file_name = [] #storage of file name
frame_number = [] #storage of frame number

for root, dirs, files in os.walk(path):
    for file in files:
            if file.endswith('.zip'): #ROI must be saved as ZIP file
                print(root+file)
                roi_b = read_roi_zip(root + "\\" + file)
                for key in roi_b.keys():
                    deq=0
                    asb=0
                    deqa=0

                    if roi_b[key]['type']=='traced':
                        x = np.array(roi_b[key]['x'])
                        y = np.array(roi_b[key]['y'])
                        x = np.r_[x, x[0]]
                        y = np.r_[y, y[0]]
                        tck, u = scipy.interpolate.splprep([x, y], s=0, per=True)
                        #Making the outline of the bubble.
                        #Increase the interpolation splines by increasing the linspace
                        xi, yi = scipy.interpolate.splev(np.linspace(0, 1,60000), tck)
                        #sorting based on y values
                        yj = np.sort(list(map(int,yi)))
                        #sorting xs based on y values
                        xj = [xi for _, xi in sorted(zip(yi,xi))]
                        #putting the sorted x and ys together
                        p =list(zip(xj,yj))
                        #collecting together the xs based on the same y values
                        ga = [[i for i, j in g]
                              for k,g in groupby(p,key=itemgetter(1))]
                        for i in ga: #taking the max/min of the x value
                                k = np.max(i)
                                l = np.min(i)
```

```
                                temp = k - l
                                #Calculating Deq for each slice
                                deq = deq + ((np.pi/4)*temp**2)
                                #Calculating D eq,asb for each slice
                                asb = asb + (np.pi*temp)
                        deq_tot = (6/np.pi)**(1/3) * deq**(1/3) #Combining all of the slices
                        deqa = (asb/np.pi)**(1/2) #Combining all of the D eq, asb
                        deq_store.append(deq_tot)
                        asb_store.append(asb)
                        deqa_store.append(deqa)
                        file_name.append(roi_b[key]['name'])
                    else: #Tell where error could be
                        print(roi_b[key]['name'])
                df = DataFrame({'File':file_name, 'Deq':deq_store, 'Asb':asb_store,
                    'Deqa':deqa_store})
                df.to_excel(root + file + ".xlsx")
            #Reseting
            deq_store = []
            asb_store = []
            deqa_store = []
            file_name = []

```